Modelling of a passive Reactor Cavity Cooling System (RCCS) for a nuclear reactor core subject to environmental changes and the optimisation of the RCCS radiation heat shield

by

Aldo Verwey

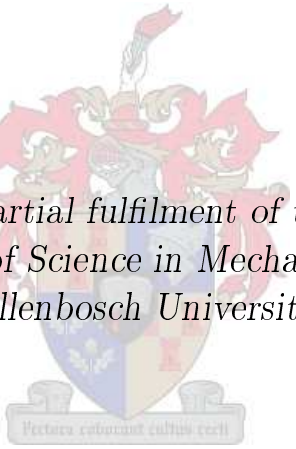

Thesis presented in partial fulfilment of the requirements for the degree of Master of Science in Mechanical Engineering at Stellenbosch University

Department of Mechanical and Mechatronics Engineering,
University of Stellenbosch,
Private Bag X1, Matieland 7602, South Africa.

Supervisor: Mr. R.T. Dobson

March 2010

Declaration

By submitting this thesis electronically, I declare that the entirety of the work contained therein is my own, original work, that I am the owner of the copyright thereof (unless to the extent explicitly otherwise stated) and that I have not previously in its entirety or in part submitted it for obtaining any qualification.

Signature:  .....

A. Verwey

Date: 15/02/2010 .....

Abstract

Modelling of a passive Reactor Cavity Cooling System (RCCS) for a nuclear reactor core subject to environmental changes and the optimisation of the RCCS radiation heat shield

A. Verwey

Department of Mechanical and Mechatronics Engineering,
University of Stellenbosch,
Private Bag X1, Matieland 7602, South Africa.

Thesis: MScEng (Mech)

March 2010

A reactor cavity cooling system (RCCS) is used in the PBMR to protect the concrete citadel surrounding the reactor from direct nuclear radiation impingement and heat. The specified maximum operating temperature of the concrete structure is 65 °C for normal operating conditions and 125 °C for emergency shut-down conditions. A conceptual design of an entirely passive RCCS suitable for the PBMR was done by using closed loop thermosyphon heat pipes (CLTHPs) to remove heat from a radiation heat shield over a horizontal distance to an annular cooling dam placed around the PBMR. The radiation shield is placed in the air space between the Reactor Pressure Vessel (RPV) and the concrete citadel, 180 mm from the concrete citadel.

A theoretical heat transfer model of the RCCS was created. The theoretical model was used to develop a computer program to simulate the transient RCCS response during normal reactor operation, when the RCCS must remove the excess generated heat from the reactor cavity and during emergency shut-down conditions, when the RCCS must remove the decay heat from the reactor cavity. The main purpose of the theoretical model is to predict the surface temperature of the concrete citadel for different heat generation modes in the reactor core and ambient conditions.

The theoretical model assumes a 1D geometry of the RCCS. Heat transfer by both radiation and convection from the RPV to the radiation heat shield (HS) is calculated. The heat shield is modelled as a fin. The fin efficiency was determined with the experimental work. Conduction through the fin is considered in the horizontal direction only. The concrete structure surface is heated by radiation from the outer surface of the heat shield as well as by convection heat transfer from the air between the heat shield and the concrete structure surface. The modelling of the natural convection closed loop thermosyphon heat pipes in the RCCS is done by using the Boussinesq approximation and the homogeneous flow model.

An experiment was built to verify the theoretical model. The experiment is a full scale model of the PBMR in the horizontal, or main heat transfer, direction, but is only a 2 m high section. The experiments showed that the convection heat transfer between the RPV and the HS cannot be modelled with simple natural convection theory. A Nusselt number correlation developed especially for natural convection in enclosed rectangles found in literature was used to model the convection heat transfer. The Nusselt number was approximately 3 times higher than that which classic convection theory suggested.

An optimisation procedure was developed where 121 different combinations of fin sizes and heat pipe sizes could be used to construct a RCCS once a cooling dam size was chosen. The purpose of the optimisation was to find the RCCS with the lowest total mass. A cooling dam with a diameter of 50 m was chosen. The optimal RCCS radiation heat shield that operates with the working fluid only in single phase has 243 closed loop thermosyphon heat pipes constructed from 62.72 mm ID pipes and 25 mm wide flatbar fins. The total mass of the single phase RCCS is 225 tons. The maximum concrete structure temperature is 62.5 °C under normal operating conditions, 65.8 °C during a PLOFC emergency shut-down condition and 80.9 °C during a DLOFC emergency shut-down condition. In the case where one CLTHP fails and the adjacent two must compensate for the loss of cooling capacity, the maximum concrete structure temperature for a DLOFC emergency shut-down will be 87.4 °C. This is 37.6 °C below the specified maximum temperature of 125 °C. The RCCS design is further improved when boiling of the working fluid is induced in the CLTHP. The optimal RCCS radiation heat shield that operates with the working fluid in a liquid-vapour mixture, or two phase flow, has 338 closed loop thermosyphon heat pipes constructed from 38.1 mm ID pipes and 20 mm wide flatbar fins. The total mass of the two phase RCCS is 198 tons, 27 tons less than the single phase RCCS. The maximum concrete structure temperature is 60 °C under normal operating conditions, 2.5 °C below that of the single phase RCCS. During a PLOFC emergency shut-down condition, the maximum concrete structure temperature is 62.3 °C, 3.5 °C below that of the single phase RCCS and still below the normal operating temperature of the single phase RCCS.

By inducing two phase flow in the CLTHP, the maximum temperature of the working fluid is fixed equal to the saturation temperature of the working fluid at the vacuum pressure. This property of water is used to limit the concrete structure temperature. This effect is seen in the transient response of the RCCS where the concrete structure temperature increases until boiling of the working fluid starts and then the concrete structure temperature becomes constant irrespective of the heat load on the RCCS. An increased heat load increases the quality of the working fluid liquid-vapour mixture. Working fluid qualities approaching unity causes numerical instabilities in the theoretical model. The theoretical model cannot capture the heat transfer to a control volume with a density lower than approximately 20 kg/m^3. This limits the extent to which the two phase RCCS can be optimised.

Recommendations are made relating to future work on how to improve the theoretical model in particular the convection modelling in the reactor cavities as well as the two phase flow of the working fluid. Further recommendations are made on how to improve the basic design of the heat shield as well as the cooling section of the CLTHPs.

Uittreksel

Modellering van 'n passiewe verkoelingstelsel vir 'n kernreaktor onderworpe aan veranderinge in omgewingstoestande en die optimering van die stralingskerm

("Modelling of a passive Reactor Cavity Cooling System (RCCS) for a nuclear reactor core subject to environmental changes and the optimisation of the RCCS radiation heat shield")

A. Verwey

Departement Meganiese en Megatroniese Ingenieurswese,
Universiteit van Stellenbosch,
Privaatsak X1, Matieland 7602, Suid Afrika.

Tesis: MScIng (Meg)

Maart 2010

'n Reaktor lug spasie verkoelingstelsel (RLSVS) word in die PBMR gebruik om die beton wat die reaktor omring te beskerm teen direkte stralingskade en hitte. Die gespesifiseerde maksimum temperatuur van die beton is 65 °C onder normale bedryfstoestande en 125 °C gedurende die noodtoestand afskakeling van die reaktor. 'n Konseptuele ontwerp van 'n geheel en al passiewe RLSVS geskik vir die PBMR is gedoen deur gebruik te maak van geslote lus termo-sifon (GLTSe) om hitte van die stralingskerm te verwyder oor a horisontale afstand na 'n ringvormige verkoelingsdam wat rondom die reaktor geposisioneer is. Die stralingskerm word in die lug spasie tussen die reaktor drukvat (RDV) en die beton geplaas, 180 mm vanaf die beton.

'n Teoretiese hitteoordrag model van die RLSVS was geskep. Die teoretiese model was gebruik vir die ontwikkeling van 'n rekenaar program wat die transiënte gedrag van die RLSVS sal simuleer gedurende normale bedryfstoestande, waar die oorskot gegenereerde hitte verwyder moet word vanuit die reaktor lug spasie, asook gedurende noodtoestand afskakeling van die reaktor, waar die afnemingshitte verwyder moet word. Die primêre doel van die teoretiese model is om the oppervlak temperatuur van die beton te voorspel onder verskillende bedryfstoestande asook verskillende omgewingstoestande.

Die teoretiese model aanvaar 'n 1D geometrie van die RLSVS. Hitte oordrag d.m.v. straling asook konveksie vanaf die RDV na die stralingskerm word bereken. The stralingskerm word gemodelleer as 'n vin. Die vin doeltreffendheid was bepaal met die eksperimente wat gedoen was. Hitte geleiding in die vin was slegs bereken in die horisontale rigting. Die beton word verhit deur straling vanaf die agterkant van die stralingskerm asook deur konveksie vanaf die lug tussen die stralingskerm en die beton. The modellering van die natuurlike konveksie GLTS hitte pype word gedoen deur om gebruik te maak van

die Boussinesq benadering en die homogene vloei model.

'n Eksperiment was vervaardig om the teoretiese model te verifieer. Die eksperiment is 'n volskaal model van die PBMR in die horisontale, of hoof hitteoordrag, rigting, maar is net 'n 2 m hoë snit. Die eksperimente het gewys dat die konveksie hitte oordrag tussen die RDV en die stralingskerm nie met gewone konveksie teorie gemodelleer kan word nie. 'n Nusselt getal uitdrukking wat spesifiek ontwikkel is vir natuurlike konveksie in geslote, reghoekige luggapings wat in die literatuur gevind was, was gebruik om die konveksie hitteoordrag te modelleer. Die Nusselt getal was ongeveer 3 maal groter as wat klassieke konveksie teorie voorspel het.

'n Optimeringsprosedure was ontwikkel waar 121 verskillende kombinasies van vin breedtes en pyp groottes wat gebruik kan word om 'n RLSVS te vervaardig nadat 'n toepaslike verkoelingsdam diameter gekies is. Die doel van die optimering was om die RLSVS te ontwerp wat die laagste totale massa het. 'n Verkoelingsdam diameter van 50 m was gekies. Die optimale RLSVS stralingskerm, waarvan die vloeier slegs in die vloeistof fase bly, bestaan uit 243 GLTSe wat van 62.72 mm binne diameter pype vervaardig is met 25 mm breë vinne. The totale massa van die enkel fase RLSVS is 225 ton. Die maksimum beton temperatuur is 62.5 °C vir normale bedryfstoestande, 65.8 °C vir 'n PLOFC noodtoestand afskakeling en is 80.9 °C vir 'n DLOFC noodtoestand afskakeling. In die geval waar een GLTS faal gedurende 'n DLOFC noodtoestand afskakeling en die twee naasgeleë GLTSe moet kompenseer vir die vermindering in verkoelings kapasiteit, is die maksimum beton temperatuur 87.4 °C. Dit is 37.6 °C laer as die gespesifiseerde maksimum temperatuur van 125 °C. Die RLSVS ontwerp kan verder verbeter word wanneer die vloeier in die GLTSe kook. Die optimale RLSVS stralingskerm met die vloeier wat kook, of in twee fase vloei is, bestaan uit 338 GLTSe wat van 38.1 mm binne diameter pype vervaardig is met 20 mm breë vinne. The totale massa van die twee fase vloei RLSVS is 198 ton, 27 ton ligter as die enkel fase RLSVS. Die maksimum beton temperatuur is 60 °C vir normale bedryfstoestande, 2.5 °C laer as die enkel fase RLSVS. Gedurende 'n PLOFC noodtoestand afskakeling is die maksimum beton temperatuur 62.3 °C, 3.5 °C laer as die enkel fase RLSVS en nogtans onder die maksimum beton temperatuur van die enkel fase RLSVS vir normale bedryfstoestande.

Deur om koking te veroorsaak in die GLTS word die maksimum temperatuur van die vloeier vasgepen gelyk aan die versadigings temperatuur van die vloeier by die vakuüm druk. Hierdie einskap van water word gebruik om 'n limiet te sit op die maksimum temperatuur van die beton. Hierdie effek kan gesien word in die transiënte gedrag van die RLSVS waar die beton temperatuur styg tot en met koking plaasvind en dan konstant raak ongeag van die hitte belasting op die RLSVS. 'n Toename in die hitte belasting veroorsaak net 'n toename in die kwaliteit van die vloeistof-gas mengsel. Mengsel kwaliteite van 1 nader veroorsaak numeriese onstabiliteite in die teoretiese model. The teoretiese model kan nie die hitteoordrag beskryf na 'n kontrole volume wat 'n digtheid het laer as ongeveer 20 kg/m^3. Hierdie plaas 'n limiet op die optimering van die twee fase RLSVS.

Aanbevelings was gemaak met betrekking tot toekomstige werk aangaande die verbetering van die teoretiese model met spesifieke klem op die modellering van konveksie in die reaktor asook die modellering van twee fase vloei. Verdere aanbevelings was gemaak aangaande die verbetering van die stralingskerm ontwerp asook die ontwerp van die verkoeling van die GLTSe.

Acknowledgements

To Mr Dobson, thank you for your enthusiastic support and guidance throughout this thesis. Your knowledge has helped me with every aspect of this thesis and encourages me to never stop studying the engineering world as well as life's philosophical questions.

To my parents, Danie and Amanda, thank you for all your love, support and encouragement.

To Marizel, thank you for your loving support and understanding through the tough times.

To my friends, thank you for all the great memories.

To Mr F. Zietsman, Greame Hamerse and the rest of the team who helped with the construction of the experimental apparatus, thank you.

PBMR (Pty) Ltd. is thanked for the financial support.

Thank you God, for giving me the ability to work and study. Thank you for providing for my every need and guiding me through my life.

Philippians 4:13 *I can do everything through Him who gives me strength.*

Dedications

To my family and friends

Contents

List of Figures

List of Tables

Nomenclature

Constants

$\pi =$	3.141 592 654	
$\mathrm{e} =$	2.718 281 828	
$g =$	9.81 Gravitational acceleration	$[\mathrm{m/s^2}]$
$\sigma =$	$5.67\mathrm{x}10^{-8}$ Stefan-Boltzmann constant	$[\mathrm{W/m^2K^4}]$

Variables

A	Area	$[\mathrm{m^2}]$
A_x	Cross sectional area of a control volume	$[\mathrm{m^2}]$
A_z	Longitudinal area of a control volume	$[\mathrm{m^2}]$
a	Speed of sound	$[\mathrm{m/s}]$
B	Any property in Reynolds transport theorem	$[\ ]$
B	Buoyancy summation term	$[\mathrm{kg/m\,s^2}]$
C	Pulse velocity	$[\mathrm{m/s}]$
c_p	Constant pressure specific heat	$[\mathrm{J/kg\,K}]$
c_v	Constant volume specific heat	$[\mathrm{J/kg\,K}]$
D	Diameter	$[\mathrm{m}]$
d_i	Inside diameter	$[\mathrm{m}]$
d_o	Outside diameter	$[\mathrm{m}]$
dr	Reactor core diameter	$[\mathrm{m}]$
E	Total energy	$[\mathrm{J}]$
e	Energy per unit volume	$[\mathrm{J/m^3}]$
F	Force	$[\mathrm{N}]$
F	Force summation term	$[\mathrm{N/m^2}]$
$\mathcal{F}_{fc}$	View factor from the fin to the concrete	$[\ ]$
$\mathcal{F}_{rf}$	View factor from the RPV to the fin	$[\ ]$
g'	Reduced gravitational acceleration	$[\mathrm{m/s^2}]$
h	Convection heat transfer coefficient	$[\mathrm{W/m^2\,^\circ C}]$
h	Enthalpy	$[\mathrm{J/kg}]$
h_{fg}	Enthalpy of evaporation	$[\mathrm{J/kg}]$
k	Thermal conductivity	$[\mathrm{W/m^\circ C}]$
L	Length	$[\mathrm{m}]$
M	Mass summation term	$[\mathrm{kg/m^2}]$

m	Mass	[kg]
$\dot{m}$	Mass flow rate	[kg/s]
$\dot{m}_{evap}$	Rate of evaporation	[kg/s]
Ma	Mach number	[ ]
Nhp	Number of heat pipes	[ ]
p	Pressure	[Pa]
Pr	Prandtl number	[ ]
Q	Total heat transferred	[J]
$\dot{Q}$	Heat transfer rate	[W]
R	Thermal resistance	[°C/W]
Ra	Rayleigh number	[ ]
Re	Reynolds number	[ ]
rcs	Radius of concrete structure	[m]
T	Temperature	[°C or K]
t	Time	[s]
Δt	Time step	[s]
U	Internal energy	[J]
U	Overall heat transfer coefficient	[W/m^2 °C]
u	Internal energy per unit volume	[J/m^3]
u_f	Internal energy per unit mass of a saturated liquid	[J/kg]
u_{fg}	Internal energy of evaporation per unit mass	[J/kg]
V	Velocity	[m/s]
V	Volume	[m^3]
v	Velocity	[m/s]
v	Kinematic Viscosity	[m^2/s]
W	Work done	[J]
x	Mass fraction of the liquid	[ ]
z	Height relative to a reference point	[m]

Greek letters

β	Value per unit mass of a property in Reynolds transport theorem	[ ]
β	Volume expansivity	[K^{-1}]
ϵ	Emissivity	[ ]
η	Fin efficiency	[%]
μ	Dynamic viscosity	[kg/m s]
ρ	Density	[kg/m^3]
θ	Vertical angle of control volume	[rad]
τ	Shear stress	[Pa]

Vectors and Tensors

$\overrightarrow{a}$	Acceleration	[m/s^2]

$\overrightarrow{F}$	Force	[N]
$\overrightarrow{v}$	Velocity	[m/s]

Subscripts

atm	Atmosphere
conv	Convection
cs	Concrete structure
env	Environment
i	Inside, inlet
i	Control volume number counter
j	Radial control volume number counter through the concrete structure
L	Left hand side
lam	Laminar
R	Right hand side
rad	Radiation
ref	Reference
sys	System
turb	Turbulent

Superscripts

$\dot{}$	(over dot) Quantity per unit time

Abbreviations

CV	Control Volume
CLTHP	Closed Loop Thermosyphon Heat Pipe
DLOFC	Depressurized Loss Of Forced Coolant
CV	Control Volume
DLOFC	Depressurized Loss Of Forced Coolant
DWS	Demineralized Water System
EPCC	Equipment Protection Cooling Circuit
FPS	Fire Protection System
HTR	High Temperature Reactor
HS	Heat Shield
ID	Inside Diameter
PBMR	Pebble Bed Modular Reactor
PLOFC	Pressurized Loss Of Forced Coolant
RCCS	Reactor Cavity Cooling System
RPV	Reactor Pressure Vessel

Chapter 1

Introduction

This chapter serves as an introduction to how the thesis topic has originated. The chapter gives the background information to the origins of the research, followed by a detailed problem definition explaining the technical difficulties of the study. The research objectives are given in which the role that this thesis plays in reactor cavity cooling research is outlined. The chapter concludes with an outline of the work done.

1.1 Background for conducting the research

Innovative nuclear power plants are being designed by the U.S.A, France, Finland, China, India and South Africa by incorporating passive systems to enhance the safety of these reactors by the elimination of active components. These are all Generation IV reactors and adhere to high safety standards. Passive systems are extensively developed for the use of reactor cavity cooling. The passive cooling systems must facilitate the fulfilment of safety functions of the nuclear reactors during normal operation and core cooling during emergency shut-downs.

This research project relates to the Pebble Bed Modular Reactor New Technology Development Program and in particular to the cooling of the reactor core cavity and concrete citadel with a passive cooling system. The concrete structure surrounding the reactor core pressure vessel of the PBMR reactor needs to be kept below a specified temperature for various operating conditions. Some research has been done to investigate the viability of using passive cooling systems for nuclear reactor cavity cooling, but most of the current work in the literature is very case specific. Current work mostly focuses on an existing cooling system and simulates the performance of the system using CFD. For design purposes, a tool is needed to aid the designer in developing a passive cooling system. In order to create such a tool, it is necessary to develop a computer program that can be easily used, do calculations quickly, and provide results that are accurate enough to be used as a design guide and to find an optimal reactor cavity cooling system for any nuclear reactor.

1.2 Problem definition

The goal of any Reactor Cavity Cooling System (RCCS) design is to create the ultimate heat sink. The RCCS must ensure the thermal integrity of the nuclear fuel, the core, the Reactor Pressure Vessel (RPV) and all equipment in the reactor cavity. Furthermore, the

RCCS must ensure that the concrete structure surrounding the RPV is kept below 65 °C for normal operating conditions and below 125 °C for the case of total loss of the primary helium coolant flow in the case of the PBMR. The current PBMR RCCS is not an entirely passive system. The RCCS presented in this thesis must be an entirely passive cooling system. The PBMR RCCS must be able to remove heat from the reactor cavity for three operating conditions as listed below:

- The normal operating condition, when only the residual heat must be removed.
- In the case when there is a coolant leak in a closed loop thermosyphon heat pipe (CLTHP) and the adjacent two CLTHPs must compensate for this loss in cooling capacity of the RCCS.
- In the case of an emergency shut-down, when the decay heat must be removed.

The research done in this thesis attempts to develop a RCCS design tool that will eliminate the need for creating a CFD model of the RCCS in its early design stages. A CFD analysis takes a lot of time to create meshes that accurately represent the geometries and heat transfer properties of a heat transfer system like an RCCS. It has been shown in literature that natural convection thermosyphon and convection in cavities can be modelled accurately by using 1D models. (Ambrosini, 2008) By using a 1D code, with a small number of nodes, or control volumes, in comparison with a CFD model, a temperature profile of the RCCS can be obtained in a short amount of time. The RCCS design tool must also be a optimisation tool. It must thus be able to change all the design variables of the RCCS. This is something that is very time consuming in a CFD model, whereas it is simple to change the value of any variable in a computer code.

The RCCS design tool must be verified in some way. This can be done either with an experiment or with a CFD simulation. After the verification and possible improvement of the theoretical model, it can be used as a design and optimisation tool for a RCCS design. The final design should then be verified with a detailed CFD simulation.

1.3 Research objectives

The objectives of this research are as follows:

1. Create a theoretical model of the heat transfer from the reactor core to the concrete citadel and to the environment with the use of a RCCS. The following need to be considered:
   a) The simplifying assumptions for the modelling of CLTHPs must be established using a literature study.
   b) A suitable solution method for 1D algorithms must be found using a literature study.
   c) Investigate the decay heat of the PBMR and express the decay heat as a function of time that can be used in the theoretical model.
   d) Investigate the grid independence of the theoretical model.

e) Do a sensitivity analysis of the theoretical model to establish what material properties has the biggest influence on the theoretical results.

2. Design and construct experimental apparatus that will be able to verify the theoretical model.

   a) The appropriate size of the experiment must be decided. The experiment must be able to capture the modes of heat transfer as will exist in the PBMR.

   b) Modify the theoretical model to simulate the experiments.

   c) Use the experimental data and the sensitivity analysis to determine the fin efficiencies of the different heat pipes and the material properties of the heat shields and the concrete structure.

3. Use the theoretical model as an optimisation tool to optimise the RCCS for a minimum total weight while satisfying the design constraints for each operating condition listed in Section 1.2.

   a) Create tables that list the temperatures of the concrete citadel as calculated by the theoretical model for differently sized CLTHPs and heat shields.

   b) Using the tables, select the RCCS with the lowest total mass and test the selected RCCS under all operating conditions as listed in Section 1.2.

4. Finally, the optimisation results must be interpreted and conclusions drawn. Recommendation must also be given for future work on the RCCS of the PBMR.

1.4 Outline of work

In order to achieve the above-mentioned goals, a literature study was done to give insight to the design process of a RCCS. The use of passive systems and the design of them with emphasis on safety design is given in Chapter 2. The design considerations for a RCCS are given as well as the basic requirements for an effective RCCS. The current RCCS of the PBMR was investigated to form a sound basis for the optimisation of the RCCS. A conceptual design of a new RCCS is given in Chapter 2 as well. A literature study regarding the effective thermal conductivity of the PBMR was needed and is shown in Chapter 2. The different operating conditions are discussed as well. The radiation and convection heat transfer in the reactor cavity are discussed in Chapter 2. The chapter concludes with the simplifying assumptions used in the modelling of the CLTHPs.

Chapter 3 discusses the mathematical theory that was used to create the theoretical model that simulates the heat transfer from the reactor core to the RCCS and ultimately to the environment. The equations are either derived from the conservation equations or are used as found in literature.

Chapter 4 shows how the mathematical theory was used to develop an algorithm that was programmed in PowerBASIC™ (2008). The chapter discusses the grid independence of the computer program and gives a sample calculation.

The goals of the experiments, the design of the experimental apparatus and the experimental results are given in Chapter 5. The experimental procedure and the data handling

are also discussed.

Chapter 6 shows a sensitivity analysis that was done for the theoretical model. The effect of the material properties of the RPV, the heat shield (HS) and the concrete citadel on the surface temperature of the concrete citadel is investigated.

Chapter 7 discusses the optimisation of the RCCS. The optimisation goals and the design variables of the RCCS are given as well as the design constraints.

Chapter 8 gives the results of the optimisation of the RCCS. The results of the optimisation and the modelling of the RCCS is discussed in Chapter 9 and conclusions are drawn on the findings of the study. Chapter 10 concludes this thesis and gives recommendations regarding future work.

Chapter 2

Literature Study

2.1 Design for safety and the use of passive cooling systems

The PBMR design team set out to create an inherently safe nuclear reactor, meaning that the reactor does not need any active safety intervention in the event of a depressurisation loss of forced coolant and automatically reverts back to a normal state after the shut-down transient. PBMR started their search for this level of safety by setting certain safety goals. These goals are summarised by Koster *et al.* (2003) as follows:

- There shall be no design based event, either from within the reactor or from external sources, which would deem it necessary for anyone living near the site boundary to take shelter or be evacuated.
- There shall be no need for moving mechanical components to ensure that the set safety targets are achieved.
- Exposure of plant personnel shall be significantly lower than the best international values presently being achieved.

The first goal is achieved with the advanced fuel design for the PBMR. The danger to the public for any nuclear reactor lies in the fission products contained within the fuel and its casing. As already stated, the requirement is that the evacuation of residents near the reactor must never be needed. This means the vast majority of the fission products must remain within the fuel for all possible events as well as events with a very low expectancy of occurrence. For the HTR fuel PBMR intends to use, this can be virtually guaranteed as long as the maximum fuel temperature remains below 1600 °C.

The second goal is achieved by using a passive cooling system as a RCCS. Passive cooling systems have many advantages over normal cooling systems. By using a passive system, the design, installation, operation and maintenance of the cooling system is greatly simplified compared to a normal cooling water pumping system. The number of components of a passive cooling system is considerably less than that of a normal cooling system. Mayson (2005) claims that an 80 % reduction in pipe usage is possible if a passive cooling system is used. This makes a passive cooling system both very economically competitive as well as functionally competitive. The fact that a passive cooling system uses no mechanical components makes the system very reliable. The reactor can thus be

regarded as inherently safe, because if the system has a very high reliability, the chance of a breakdown is very small. Thus, there is a very small possibility that the reactor will not be kept within the specified allowed temperatures.

The third goal will be achieved partly by the fuel design and partly by the radiation shield that forms part of the RCCS. The radiation shield will be constructed from steel that will act as a γ-ray absorber and will be placed between the RPV and the concrete citadel. The concrete citadel surrounding the reactor will also act as a moderator and provide insulation.

2.2 Reactor cavity cooling system design considerations

Reactor cavity cooling systems for gas cooled reactors are typically safety grade systems, either with passive or with highly-reliable, redundant forced-convection cooling systems, designed to remove all of the core after heat in the unlikely case of failure or unavailability of the main and all other shut-down cooling systems. The objective of most RCCS designs is to serve as an ultimate heat sink, ensuring the thermal integrity of the fuel, core, vessel, and critical equipment within the reactor cavity for the entire spectrum of postulated accident sequences. (Oh and Davis, 2007)

While much of the focus of RCCS design is on performance during accident conditions, it must be kept in mind that these extreme conditions are not likely to exist during the life of a modular gas cooled reactor plant. Since the heat removed by the RCCS from the reactor vessel during normal operation is a parasitic heat loss, it would be desirable for this to be minimized. In order to achieve this, the RCCS should ideally be shut down during normal reactor operation and be turned on in an emergency. However, from the definition of passive systems, a passive cooling system cannot be actively controlled, thus the RCCS heat removal capacity should be designed to remove the maximum amount of heat generated in an emergency condition without over cooling the reactor cavity during normal operation of the RCCS.

2.3 The current RCCS design of the PBMR

A simplified layout of the PBMR cavity cooling system is shown in figure 2.1 as given by Slabber (2006). In the current RCCS design, the RCCS is driven actively by the Equipment Protection Cooling Circuit (EPCC) under normal operating conditions. The detail design and workings of the EPCC will not be discussed. The EPCC can be seen as a *pump* for the purposes of this thesis.

During normal, or active, operation, 135 kg/s of cold water is circulated by the EPCC through the tank protection wall at a height above the storage tank. The fact that the inlet pipe is higher than the storage tank is significant, because the potential energy difference prevents water from flowing from the storage tank to the EPCC via the inlet pipe, thereby bypassing the RCCS standpipes, during passive cooling operating conditions. After the water passes through the tank protection wall, the cold water then flows to the base level of the reactor. The water is then pumped through the risers, or standpipes, to

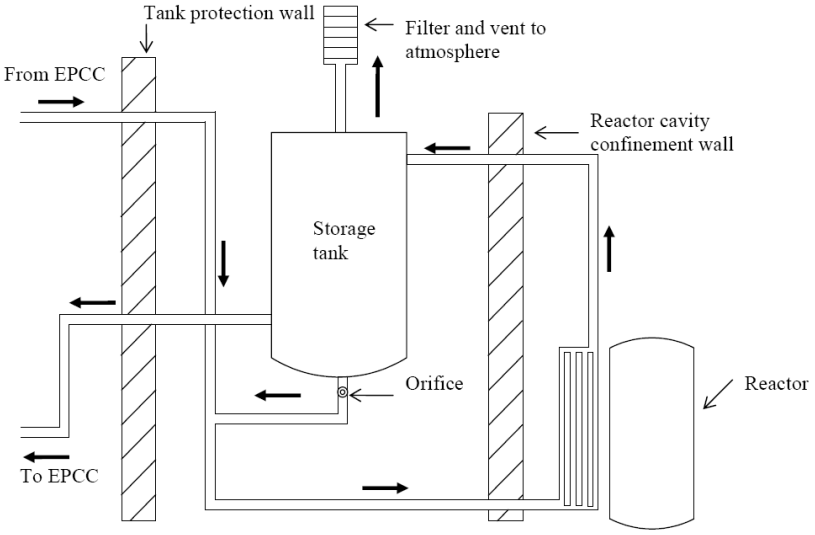

Figure 2.1: Conceptual layout of the current PBMR design

the top of the reactor and removes heat from the reactor cavity. There are 72 of these standpipes in the reactor. The heated water then flows into the storage tank at the top of the tank where it mixes with the cooler storage tank water. The storage tank water then flows out at the bottom of the tank through the tank protection wall and returns to the EPCC heat exchanger.

During passive operation the EPCC is off. Thus, there is no water being pumped through the standpipes. The mass flow rate of the water now relies on natural circulation induced by a density difference in the cooling system. During passive operation there will be no flow through the tank protection wall as shown in figure 2.1. The cooling water in the standpipes will be heated by the decay heat generated by the reactor. As the water warms up and the density drops, a density difference will be induced between the water in the standpipes and the water in the inlet pipe. The cooler, more dense, water will push the water in the standpipes up to the top of the standpipes. This causes water in the storage tank to be sucked out of the tank through the orifice plate and into the inlet pipe. In this manner, the water in the storage tank will be circulated passively through the standpipes and cool the reactor cavity. As the water in the storage tank starts to evaporate, the evaporated water will pass through the filter at the top of the storage tank into the atmosphere. During active operation, an insignificant amount of cold water will pass from the inlet pipe, via the orifice, into the storage tank, thereby bypassing the standpipes.

During active operation, the filter will prevent contaminants from outside the reactor building entering the tanks. These filters will allow clean air to pass through so that the pressure in the tanks is in balance with the ambient air pressure.

There will be 18 storage tanks each connected to 4 standpipes within the cooling system as shown in figure 2.1. Topping up of the water storage tanks to account for normal system losses, will be an automatic action by the Demineralised Water System (DWS). After larger water evaporation losses, e.g. due to passive operation, refilling will be a manually activated operation, drawing water from the DWS if time permits, or from the Fire Protection System (FPS) if fast replacement is required.

2.4 Functions and basic requirements of the RCCS

The functions and basic requirements of the RCCS are summarised as follows by Slabber (2006):

- The RCCS must provide investment protection by preventing thermal radiation from impinging directly onto the concrete walls of the reactor cavity.
- The RCCS must remove all waste, or residual, heat from the reactor cavity during normal operation, thereby maintaining the concrete surfaces of the cavity below the specified design temperature of 65 °C for normal operating conditions.
- The RCCS must remove all decay and residual heat transferred to the reactor cavity during a pressurized or depressurized loss of the forced helium coolant.
- In the event of the loss of active pumping capacity of the EPCC, the RCCS must remove heat passively from the reactor cavity and release this heat to the atmosphere. The RCCS must be able to operate passively for a minimum of 72 hours.
- Switching from active to passive operation mode must take place with no mechanical, electrical or human intervention.
- Together with the design of the heat transfer path from the fuel to the outer surface of the RPV, the RCCS must assist the other cooling systems in controlling the RPV temperature during normal operation as well as in a loss of forced gas coolant event. During normal operation, the RPV wall temperature must be limited to 350 °C. For a Pressurized Loss Of Forced Coolant (PLOFC), the RPV wall temperature must be limited to 474 °C and for a Depressurized Loss Of Forced Coolant (DLOFC), the RPV wall temperature must be limited to 527 °C.
- Under normal operating conditions, the RCCS must remove approximately 1890 kW of heat and approximately 3580 kW during a DLOFC event.

2.5 RCCS heat load during normal operating conditions

During the normal operation of the reactor, the RCCS must remove all the residual heat generated by the reactor and thereby protect the concrete citadel from overheating. The residual heat is the amount of heat that is being generated in the fuel pebbles that is not removed by the primary helium coolant flowing through the reactor core. The amount of residual heat that needs to be removed by the RCCS depends on the mass flow rate of the helium. The residual heat is calculated with reference to figure 2.2.

Figure 2.2 shows the heat generated in the fuel pebbles as $\dot{Q}_{thermal}$. Helium enters the reactor at T_{in} and leaves the reactor at T_{out}. Under normal operating conditions, these temperatures are 501.3 °C and 900 °C respectively. According to the design specification of the PBMR, the mass flow rate of the helium is 190 kg/s. The thermal heat generation is 395.2 MW (Slabber, 2006).

The residual, or parasitic, heat transferred to the RCCS can be calculated as follows:

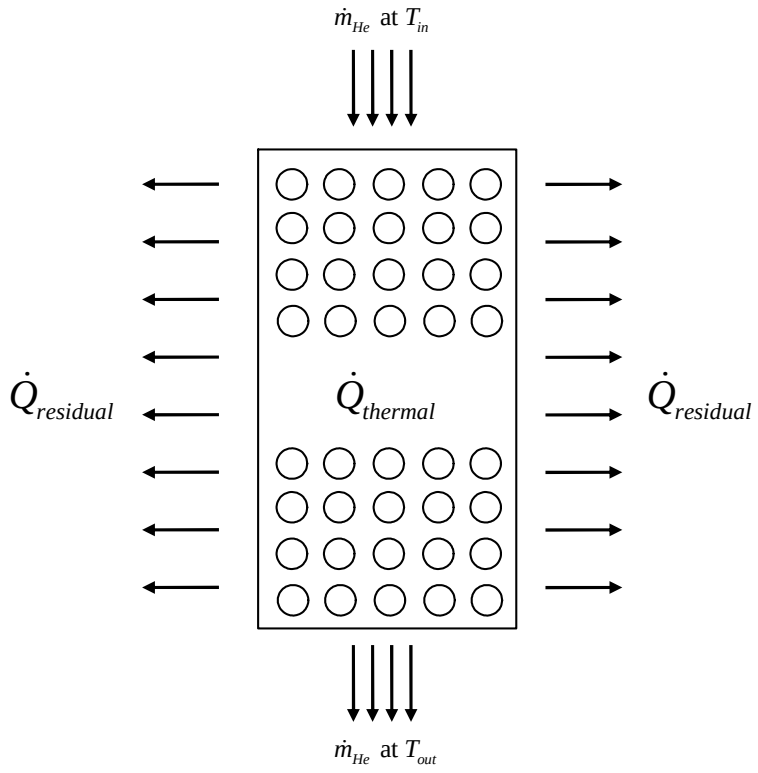

Figure 2.2: Heat flow in the reactor core

$$\dot{Q}_{residual} = \dot{Q}_{thermal} - \dot{m}_{He} c_{p_{He}} (T_{out} - T_{in}) \tag{2.5.1}$$

The constant pressure specific heat for helium stays constant over the temperature range at 5191 J/kgK. The helium pressure increases slightly while passing through the reactor core, but equation (2.5.1) still holds and gives a good estimate for the residual heat. Equation (2.5.1) shows a residual heat of 1966 kW. This corresponds very well with the 1890 kW in Section 2.4 suggested by Slabber (2006).

Van Staden (2004) found the mass flow rate of helium to be 185 kg/s using a CFD analysis of the flow in the reactor core. This mass flow rate resulted in a heat load on the RCCS during normal operation of 1750 kW. By using a different model, Van Staden (2004) then found the heat load to be 1890 kW. Equation (2.5.1) shows that the heat load for a mass flow rate of 185 kg/s will be 12.3 MW. This value is clearly incorrect. This can be attributed to the fact that Van Staden (2004) included the Core Barrel Conditioning System in his CFD model. The Core Barrel Conditioning System is a second cooling system that is also fitted into the reactor cavity. In order to be conservative, for this thesis, a heat load of 1966 kW will be used. This value corresponds to the design specification mass flow rate of 190 kg/s for the helium and a temperature difference of 398.7 °C.

2.6 Heat load on the RCCS during an emergency shut-down condition

There are two types of emergency situations that are of importance when designing the RCCS. The first is a Pressurized Loss of Forced Cooling (PLOFC) event and the second is

a Depressurized Loss of Forced Cooling (DLOFC) event. These two emergency conditions will now be discussed in more detail.

2.6.1 Pressurized Loss Of Forced Cooling

The PLOFC condition is characterized simply as a situation where "helium forced circulation stops". This implies that there is no helium leakage from the primary cooling circuit, but that the flow has stopped. If this situation occurs, the reactor will be shut down immediately and the decay heat will start heating the helium in the channels in the reactor core. The subsequent natural circulation of pressurized helium that takes place within the core tends to equalize core temperatures, thus reducing the tendency to form very hot regions, as would happen in DLOFC cases. In the PLOFC case, the main concern is the top of the core and vessel, which will become the hottest. During a PLOFC event, the pressure in the helium circuit will rapidly decrease to 6.8 MPa from the operating pressure of 9.0 MPa, and the RPV wall temperature will increase to approximately 474 °C from approximately 380 °C.(Slabber, 2006)

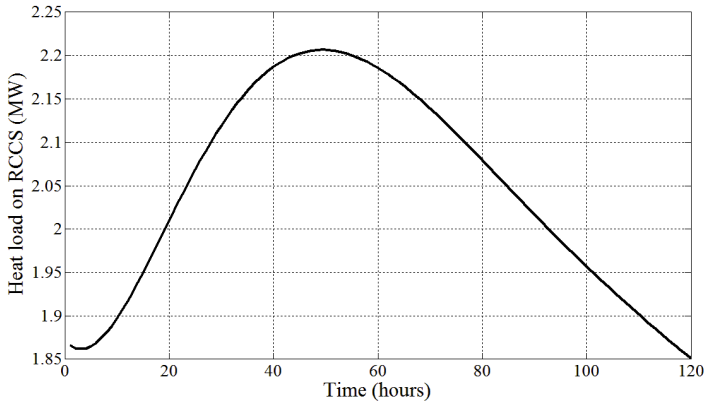

Figure 2.3: Transient heat load on the RCCS during a PLOFC (Van Staden, 2004)

Figure 2.3 shows the heat load on the RCCS as a function of time for a PLOFC event after the emergency shut-down of the reactor as was calculated by Van Staden (2004). As can be seen from the figure, the maximum heat load occurs approximately 50 hours after shut-down and is just above 2.2 MW.

2.6.2 Depressurized Loss Of Forced Cooling

During a DLOFC event it is assumed that no helium is circulated through the reactor and that the helium inventory has been vented to atmosphere because of helium leakage in the primary cooling circuit. The pressure in the reactor is therefore at atmospheric pressure equal to 101 kPa at sea level. This event simulates a loss of pressure in the helium circuit, which would also imply a reactor shut-down. For this case the reactor is sub-critical and the thermal power is the result of decay heat. The decay heat is transported to the RCCS primarily by conduction and thermal radiation only. It is assumed that there is no heat removed from the reactor core by convection to the little bit of helium that might still be in the narrow channels within the reactor core. This is regarded as a conservative approach. During a DLOFC, the RPV wall temperature will increase to approximately

527 °C.(Slabber, 2006)

The DLOFC event, unlike the PLOFC event, has many variations, including the size of the "break" and its location within the primary cooling circuit. A large break will cause a rapid blow-out of hot helium and could cause structural damage of critical items in the path of the discharge that may need to be factored into consequence estimates and postulated alleviation schemes. The leakage's location can cause air ingress. A very slow depressurization can put the reactor into a "limbo" state, between PLOFC and DLOFC for long periods, possibly making effective emergency response planning difficult. Following depressurisation, the effective core conductivity, along with the after heat (as a function of time), become the two major influences on peak fuel temperatures. The DLOFC accident is typically the design determinant for reactor maximum operating power level for a given vessel size. The reactor building of the PBMR will limit the ingress of air into the citadel.(Slabber, 2006)

The heat load on the RCCS as a function of time during a DLOFC event is not given by Van Staden (2004) and could not be found in other literature. It is assumed that the heat load has the same shape as figure 2.3 but will have a maximum value of 3580 kW as given in Section 2.4. This seems to be a plausible assumption because the neutronic behaviour of the reactor during shut-down will remain more or less the same, irrespective of the emergency condition causing the shut-down.

2.6.3 Theoretical simulation of decay heat

The heat load on the RCCS after an emergency shut-down will depend on the temperature difference between the RPV and the RCCS. It will thus be incorrect to assume the heat load on the RCCS as given in figure 2.3 for an unknown temperature difference between the RPV and the RCCS. By assuming the RCCS heat load would effectively mean that the theoretical model is inserting a heat source between the RPV and the RCCS. The decay heat generated by the reactor is the only heat source in the system and must be used to determine the heat load on the RCCS during an emergency shut-down. The decay heat is determined by the neutronic behaviour of the reactor. Therefore, for the purpose of this thesis, the neutronic behaviour will not be used to determine the decay heat. The decay heat will be simulated as given by Slabber (2007) and as shown in figure 2.4.

Figure 2.4 shows the decay heat of the reactor from 10 s after the emergency shut-down. During the first 10 s after shut-down, the generated heat drops from the normal output of 380 MW to around 16 MW. After this initial drop in reactor output, the generated heat decays as shown in the figure. The decay heat is given as a function of time by Slabber (2007) as:

$$Q_{decay} = 0.0622 Q_{normal} t^{-0.2} \tag{2.6.1}$$

where t is the time after the initial 10 second shut-down period.

By using this decay heat as the heat output of the reactor in the theoretical model and adjusting the effective thermal conductivity of the reactor, the heat load on the RCCS can be calculated. The heat load on the RCCS, as calculated with the theoretical model can

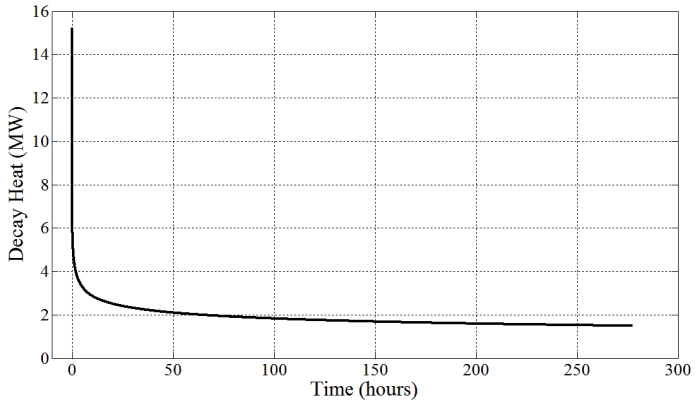

Figure 2.4: Decay Heat after emergency shut-down

be seen in figure 2.5. As can be seen from the figure, this calculated heat load compares with the heat load calculated by Van Staden (2004), and shown in figure 2.3.

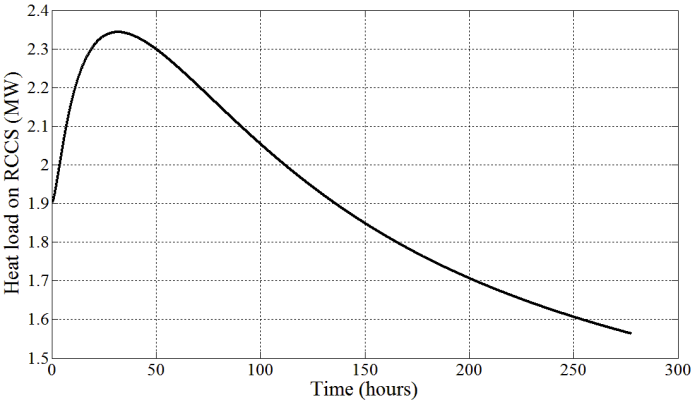

Figure 2.5: Transient heat load on the RCCS after an emergency shut-down

2.7 Geometrical description of the existing PBMR core cavity

The geometry and layout of the components in the reactor core cavity are very important design considerations for the RCCS. The core cavity components include the reactor core, the core barrel and the RPV. These components are all surrounded by the concrete citadel. Figure 2.6 shows the dimensions of each of the components according to Reitsma *et al.* (2006).

These dimensions differ somewhat from the dimensions given by Slabber (2006). Slabber (2006) suggests a slightly bigger core with a diameter of 3.7 m and a bigger core barrel outside diameter of 6.16 m. Slabber (2006) also uses a bigger RPV with an outside diameter of 6.56 m. The dimensions of the concrete citadel are given by Dams (1996). The only dimensions affecting the design of the RCCS are the RPV outside diameter and the concrete citadel inside diameter, because the RCCS must be fitted between the RPV and

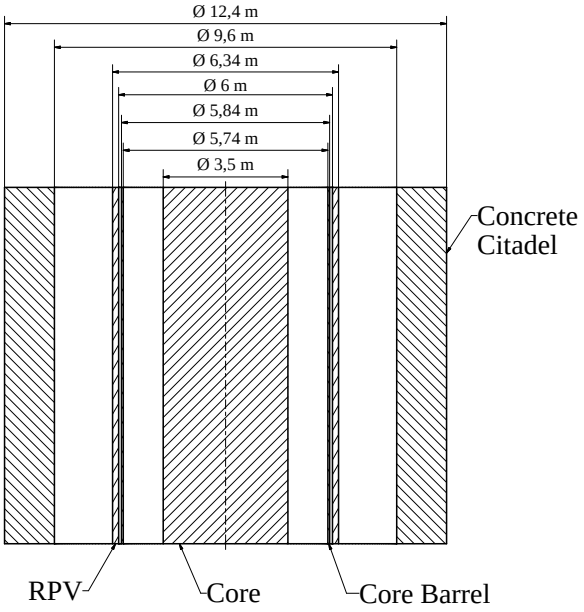

Figure 2.6: PBMR dimensions

the concrete structure. According to Slabber (2006), there is a 1.52 m gap where the RCCS can be installed and according to Reitsma *et al.* (2006) there is a 1.63 m gap. The conservative approach will be to use the smaller gap of 1.5 m.

2.8 Conceptual design of the RCCS for the PBMR

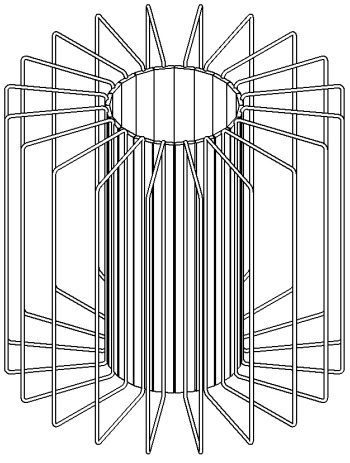

Figure 2.7: RCCS heat shield with CLTHPs concept

Figure 2.7 shows the conceptual design of the RCCS proposed in this thesis. The basic idea is to create a uniform shield consisting of a number of CLTHPs with two fins attached on either side of the risers. The fins will be placed next to each other to form a uniform heat shield. The heat shield will provide investment protection by preventing thermal radiation from impinging directly onto the concrete walls of the reactor cavity as discussed in Section 2.4. The fins can be welded together, as shown in figure 2.7, or be placed in a zig-zag formation where the adjacent fins overlap each other, should the stress,

caused by thermal expansion, in the weldments between two adjacent fins be too great. In the zig-zag formation, there will be no welding adjacent fins together. The analysis done on the performance of the RCCS in this thesis assumes that the horizontal pipes are 40 m long and that the vertical downcomers are placed in a cooling dam built around the reactor building as shown in figure 2.8. It will be possible to make use of manifolds to reduce the number of downcomers, but in order to simplify the one dimensional model of the RCCS it is assumed that each set of fins has its own complete CLTHP. By using a model as shown in figure 2.7 it is possible to analyse the performance of the RCCS by only analysing one CLTHP with its two flatbar fins. This approach simplifies the optimisation for the number of heat pipes required.

Figure 2.8: RCCS concept

Figure 2.8 shows how the risers of the RCCS will be placed between the RPV and the concrete citadel with the downcomers of each CLTHP entering an annular dam surrounding the concrete citadel. The core is represented by the red cylinder in the figure. The core barrel and the RPV are represented by the black and orange hollow cylinders respectively.

Each of the CLTHPs will also be fitted with an expansion tank as shown in figure 2.9. The function of the expansion tank is to keep the pressure in the CLTHP constant. As the working fluid heats up and expands, the working fluid is pushed into the expansion tank. The expansion tank can either be open in order to let the working fluid be at atmospheric pressure or a vacuum can be created over the expansion tank. By using an expansion tank under vacuum, the operating pressure of the working fluid can be controlled. The advantage of this is that two phase flow can be induced in the CLTHPs and thereby control the maximum temperature of the working fluid. The maximum working fluid temperature will be the saturation temperature of the working fluid at the vacuum pressure. By inducing a pressure of 25 kPa at the top of the CLTHP, the working fluid will be at its saturation temperature of 64.97 °C. The result of this is that the concrete structure temperature will be less than 65 °C. The use of two phase flow in the CLTHPs will be investigated in the optimisation of the RCCS.

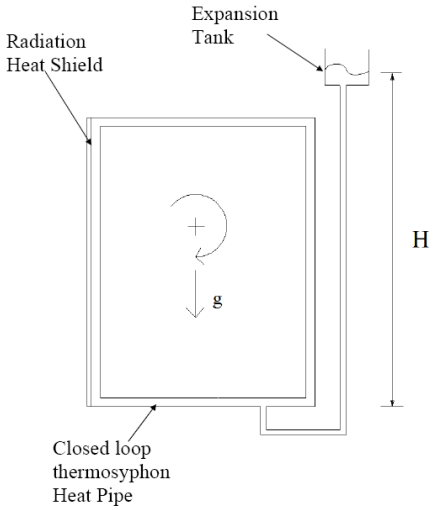

Figure 2.9: A closed loop thermosyphon heat pipe fitted with an expansion tank

2.9 Effective thermal conductivity of the pebble bed

The effective thermal conductivity of the pebble bed is defined as the combination of the pebble to pebble conduction, the conduction through the interstitial volumes and the radiation that occurs in the pebble bed. Convective heat transfer within the pebble bed can also be accounted for with the effective thermal conductivity by expressing the convection as an enhancement of the conductivity of the pebble bed.(Viljoen *et al.*, 2006)

The effective thermal conductivity of the reactor core is the dominant mechanism for the heat transfer from the fuel to the reactor pressure vessel. The effective thermal conductivity of the graphite in the core is a function of its irradiation history, temperature, orientation, and whether or not annealing is accounted for. The PBMR uses on-line refuelling, resulting in a mixing of fuel pebbles with various burn up- and irradiation histories, making these two factors difficult to model. The effective thermal conductivity of the core is usually considered to be primarily dependent on the radiant heat transfer between pebbles, and can thus be considered only a function of temperature.(Ball, 2004)

The most common method of determining the effective thermal conductivity of a pebble bed is the method presented by Zehner and Schlünder (1972). This model is used by Hossain *et al.* (2008) for analysis of high temperature gas rectors. Reimann *et al.* (2006) uses this method for helium cooled pebble beds. Ball (2004) and Viljoen *et al.* (2006) used this model for analysis of the PBMR.

In order to get a reliable approximation of the effective thermal conductivity of the PBMR to use in the theoretical model, the findings of Hoffmann and van Rensburg (2006) was used. Hoffmann and van Rensburg (2006) calculated the effective thermal conductivity by using the model developed by Zehner and Schlünder (1972), as well as the method used by Robold (1982), to calculate the effective thermal conductivity of pebble beds and then used a CFD model to verify the results. A comparison of the results of the three different methods can be seen in figure 2.10. The CFD model predicts the effective thermal conductivity higher than the other two models for higher core temperatures and is around the average of the other two models at moderate core temperatures. The effective

thermal conductivity calculated by the CFD model of Hoffmann and van Rensburg (2006) will be used in the theoretical model presented in this thesis.

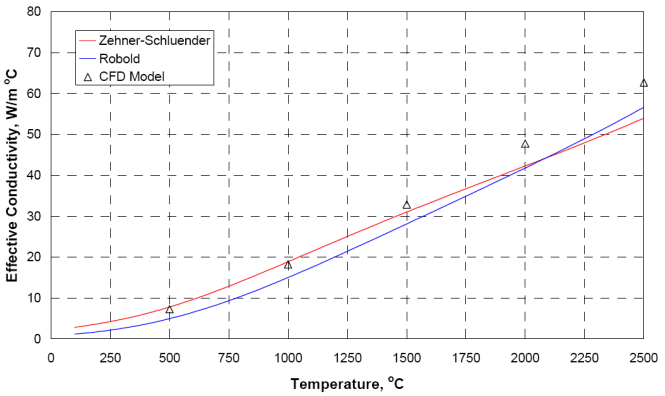

Figure 2.10: Effective thermal conductivity of the PBMR core.(Hoffmann and van Rensburg, 2006)

2.10 Radiation view factors in the reactor cavity

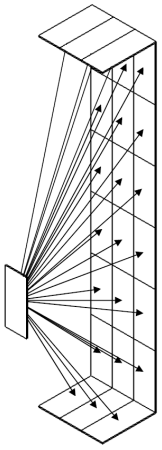

Figure 2.11: View factor from one node to the other nodes in the cavity

Figure 2.11 shows one set of radiation view factors that needs to be calculated in order to simulate the radiation heat transfer in the reactor cavity. This must be repeated for all the different elements of both the RPV and the back of the HS. The view factors will be used to calculate radiation heat transfer from the RPV to the RCCS and from the RCCS to the concrete citadel. Different view factors will be needed for different vertical positions as the temperature varies of each surface relative to a position on the surface from which the radiation is emitted. The radiation heat transfer from each element on a vertical surface, like the PRV and the HS, to the ceiling and the floor of the reactor cavity must also be calculated using the correct view factor.

2.10.1 Radiation view factor between two rectangular surfaces in parallel planes

The reactor core, RPV and radiation heat shield will be hotter at the top than at the base. This is due to the fact that hot air in the cavity will rise and the cooling water in the CLTHPs will enter the radiation shield from the bottom and will get hotter as its rises to the top of the reactor cavity. This implies that when the core, RPV and radiation heat shield are divided into nodes in the computer simulation, each node will have a different temperature and will radiate heat to all the other nodes. This makes it necessary to compute a radiation view factor for each node on surface 1 corresponding to surface 2 as shown in figure 2.12. Surfaces 1 and 2 represent any two opposing surfaces within the reactor cavity where radiation heat transfer occurs between them. The radiation heat transfer to each node will then be computed using the form factor to each of the nodes on the opposing surface and the temperature of the corresponding nodes.

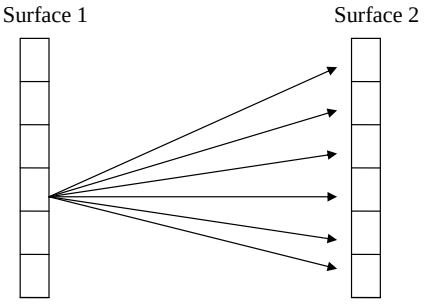

Figure 2.12: View factor from one node to other nodes

A major problem in evaluating the radiation heat transfer between two surfaces is to account for the geometric relations involved in how the surfaces view each other (Narayana, 1998). The calculation of the radiation view factor between two finite surfaces requires the solution of a double area integral, or fourth-order integration. The analytical procedure required to set up the double area integral is explained in Appendix A.

View factors for complex configurations may be calculated without any integration by using the rules of reciprocity and summation, and the known view factor for a more basic geometry. This is called view factor algebra and can be used in order to calculate the view factor for rectangle 1 to rectangle 3' as shown in figure 2.13, where two rectangles lie in parallel planes but do not directly oppose each other.

A more basic geometry to use for solving the view factor in figure 2.13 is shown in figure 2.14, where the two rectangles oppose each other directly. The radiation view factor for two identical, parallel, directly opposed rectangles, as shown in figure 2.14, is given by equation (2.10.1) as given by Modest (2003).

$$F_{1-2} = \frac{2}{\pi XY}\left\{ ln\left[\frac{(1+X^2)(1+Y^2)}{1+X^2+Y^2}\right]^{1/2} + X\sqrt{1+Y^2}tan^{-1}\frac{X}{\sqrt{1+Y^2}} + Y\sqrt{1+X^2}tan^{-1}\frac{Y}{\sqrt{1+X^2}} - Xtan^{-1}X - Ytan^{-1}Y\right\} \quad (2.10.1)$$

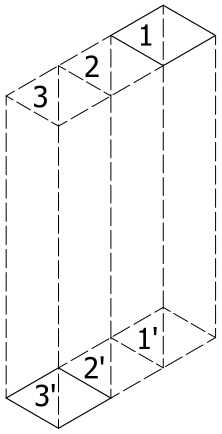

Figure 2.13: View factor for two parallel, non-opposing rectangular surfaces

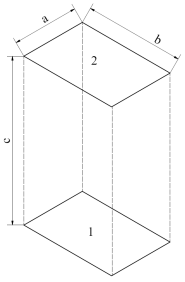

Figure 2.14: View factor for two identical, parallel, directly opposed rectangles

where $X = a/c$ and $Y = b/c$.

Narayana (1998) uses equation (2.10.1) and view factor algebra to give the view factor for the case in figure 2.13 as:

$$A_1 F_{1-3'} = \frac{1}{2}\left(K_{123} + K_2 - K_{12} - K_{23}\right) \tag{2.10.2}$$

The general solution is given by $K_m = A_m F_{mm'}$ e.g. $K_{123} = (A_1 + A_2 + A_3)\, F_{123-1'2'3'}$

2.10.2 Radiation view factor between two rectangular surfaces in perpendicular planes

The radiation heat transfer from each element on the RPV to the top (or ceiling) and floor of the reactor cavity can be calculated by using the view factor for two rectangular surfaces in perpendicular planes as shown in figure 2.15. The view factor is given by equation (2.10.3) as given by Modest (2003) and will be the building block for all the view factor calculations for the various perpendicular rectangles in this section.

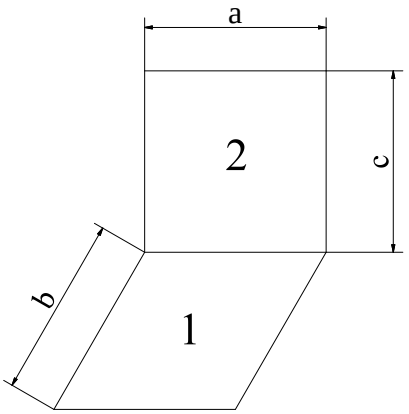

Figure 2.15: View factor for two perpendicular rectangular surfaces

$$F_{1-2} = \frac{1}{\pi W}\left(W tan^{-1}\frac{1}{W} + H tan^{-1}\frac{1}{H} - \sqrt{H^2+W^2}\,tan^{-1}\frac{1}{\sqrt{H^2+W^2}} + \frac{1}{4} ln\left\{\frac{(1+W^2)(1+H^2)}{1+W^2+H^2}\left[\frac{W^2(1+W^2+H^2)}{(1+W^2)(W^2+H^2)}\right]^{W^2}\left[\frac{H^2(1+H^2+W^2)}{(1+H^2)(H^2+W^2)}\right]^{H^2}\right\}\right) \quad (2.10.3)$$

where $W = b/a$ and $H = c/a$.

Figure 2.16 shows two rectangles in perpendicular planes that are separated by a space. The view factor is given by (2.10.4). The $F_{12,3}$ and $F_{2,3}$ view factors can be solved using (2.10.3).

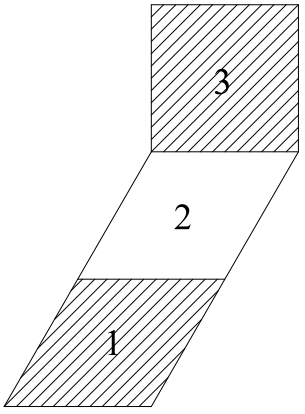

Figure 2.16: View factor for two perpendicular rectangles separated by a space

$$A_1 F_{1,3} = \frac{1}{2}\left[A_{12}F_{12,3} - A_2 F_{2,3}\right] \quad (2.10.4)$$

Figure 2.17 shows two perpendicular rectangles that have a common point as opposed to having a common side as in figure 2.15. This variation of the view factor was solved by Mills (1999) and is given by equation (2.10.5). This equation will be used as a property

to solve the more complex view factors in this section. Figure 2.17 is used to model the radiation from the very top (or bottom) element on the RPV to an element in the adjacent column of the ceiling, or floor, of the reactor cavity:

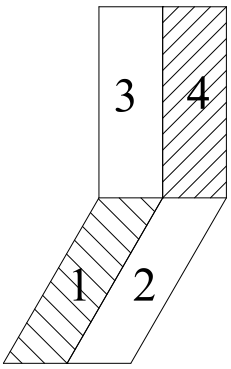

Figure 2.17: View factor for two adjacent perpendicular rectangles

$$A_1 F_{1,4} = \frac{1}{2}\left[A_{12}F_{12,34} - A_1 F_{1,3} - A_2 F_{2,4}\right] \tag{2.10.5}$$

Figure 2.18 shows two perpendicular rectangles that are completely separated. This configuration is used to model the radiation from the very top, or bottom, element on the RPV to an element in the second adjacent column of the ceiling, or floor.

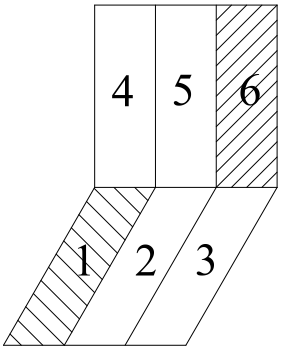

Figure 2.18: View factor for first element in the second adjacent column to reactor top

$$A_1 F_{1,6} = \frac{1}{2}\left[A_{123}F_{123,456} - A_{12}F_{12,45} + A_2 F_{2,5} - A_{23}F_{23,56}\right] \tag{2.10.6}$$

Equation(2.10.6) is used to solve the view factor in figure 2.18. The equation can also be used to solve the view factor for the top or bottom element on the RPV to elements in the i'th column on the floor (or ceiling) by simply increasing the width of the middle column representing the space between the elements in figure 2.18.

Figure 2.19 shows the configuration for the view factor from the second element of the RPV to the element on the floor (or ceiling) that is situated in the adjacent column. The view factor is solved by equation(2.10.7). Figure 2.20 shows the element moved up to the third column and is solved by equation(2.10.7).

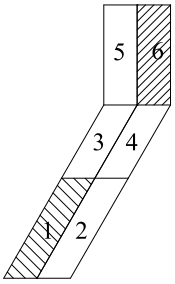

Figure 2.19: View factor for the second element in the first adjacent column to reactor top

$$A_1F_{1,6} = A_{1234}F_{1234,56} - \frac{1}{2}\left[A_{1234}F_{1234,56} - A_{24}F_{24,6} - A_{13}F_{13,5}\right] - A_{13}F_{13,5} - \frac{1}{2}\left[A_{34}F_{34,56} - A_3F_{3,5} - A_4F_{4,6}\right] - A_{24}F_{24,6} \quad (2.10.7)$$

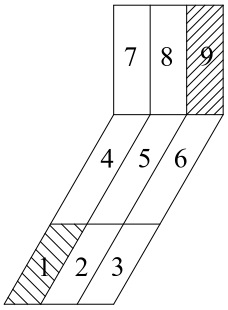

Figure 2.20: View factor for second element in the second adjacent column to reactor top

$$A_1F_{1,9} = \frac{1}{2}\left[A_{123456}F_{123456,789} - A_{1245}F_{1245,78} + A_{25}F_{25,8} - A_{456}F_{456,789} + A_{45}F_{45,78} - A_5F_{5,8} + A_{56}F_{56,89} - A_{2356}F_{2356,89}\right] \quad (2.10.8)$$

Using the figures and equations given in this section, it is possible to calculate the view factor from any element on the RPV to any element on the reactor floor or top by changing the widths and lengths of the element in the middle columns representing the space between the elements in the figures.

2.11 Convection in the reactor cavity

In most convection heat transfer problems encountered in literature, it was noticed that the objects on which heat transfer occur are assumed to be located in a fluid of infinite extent and uniform temperature. Many engineering applications however, present heat transfer situations in which free, or natural, convection occurs in closed spaces and the effect of neighbouring surfaces needs to be accounted for. One such application is in the small air space between the heat shield of the RCCS and the concrete citadel.

When the fluid is between vertical walls, or cylinders, the heat transfer from the hot surface to the cold surface can take place by conduction as well as convection depending on the Rayleigh number defined by Eckert and Drake (1972) as:

$$Ra = \frac{g\beta\left(T_{hot} - T_{cold}\right) L_c^3}{v^2} Pr \tag{2.11.1}$$

where L_c is the characteristic length and is the distance between the two surfaces. All properties are evaluated at the average temperature of the hot and cold surface.

For Rayleigh numbers below 1000, the temperature in the fluid decreases linearly along horizontal lines in the direction from the hot to the cold surface. This indicates that the heat transfer is by conduction only. For larger Rayleigh numbers, the temperature variation along horizontal lines is restricted to two boundary layers which develop along the hot and cold surface. The temperature variation is almost constant in the horizontal direction in the central region of the fluid. In cases with high Rayleigh numbers, the thermal resistance is two convection resistances in series, one on each surface. (Eckert and Drake, 1972)

There are many different correlations for Nusselt numbers for enclosures in the literature. Different ways of calculating the heat transfer from the RCCS fin to the concrete citadel will thus need to be considered in this section.

For engineering design calculations, interest is mainly concentrated on determining the total heat flow through the fluid from the hot surface to the cold surface. Eckert and Drake (1972) presents the simplest method of computing the total heat transfer by using an equivalent conductivity for the fluid as a function of Rayleigh number. The equivalent thermal conductivity for the fluid for different Ra numbers between the two surfaces can be determined using figure 2.21.

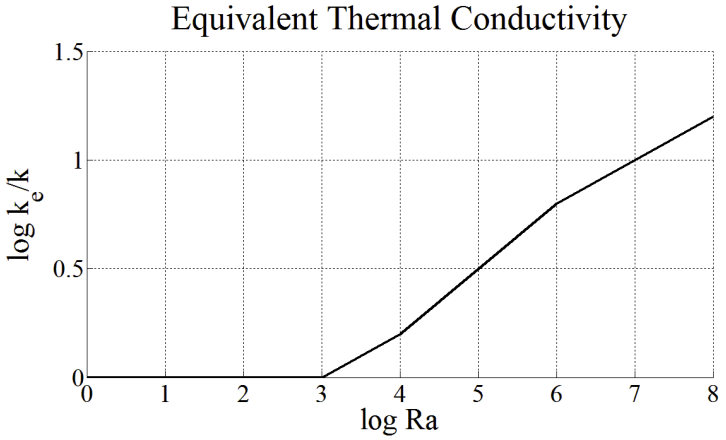

Figure 2.21: Equivalent thermal conductivity (Eckert and Drake, 1972)

Once the equivalent thermal conductivity for the fluid is found, the total heat transfer per unit time and area from the hot to the cold surface can be determined as follows:

$$q = \frac{k_e}{b}\left(T_h - T_c\right) \tag{2.11.2}$$

where

b = thickness of fluid layer
T_h = temperature of hot surface
T_c = temperature of cold surface

For the range in which $k_e/k = 1$, heat transfer through the layers takes place by conduction only. The deviation from $k_e/k = 1$ indicates the contribution of convection to the total heat flow.

Eckert and Carlson (1961) uses the following correlations for the Nusselt number:

$$Nu = 1 + 0.00166\frac{L}{H}Gr^{0.9} \tag{2.11.3}$$

for the conduction regime where

L = thickness of fluid layer
H = height of fluid layer

and

$$Nu = 1 + 0.119\left(\frac{L}{H}\right)^{0.1} Gr^{0.3} \tag{2.11.4}$$

for the convection regime.

Mills (1999) uses $Nu = 1$ for $Ra < 1000$ and calculates three different Nu numbers for $Ra > 1000$ and then uses the maximum of the three Nu numbers to calculate the convection heat transfer. The three correlations for Nu are given below.

$$Nu_1 = 0.0605Ra^{\frac{1}{3}} \tag{2.11.5}$$

$$Nu_2 = \left\{1 + \left(\frac{0.104Ra^{0.293}}{1 + \left(\frac{6310}{Ra}\right)^{1.36}}\right)^3\right\}^{\frac{1}{3}} \tag{2.11.6}$$

$$Nu_3 = 0.242\left(\frac{Ra}{H/L}\right)^{0.272} \tag{2.11.7}$$

Dobson and Ruppersberg (2006) uses the following:

$$Nu = 1.07\left(\frac{T_h - T_c}{H}\right)^{\frac{1}{4}}\frac{H}{k} \tag{2.11.8}$$

for $10^4 < Gr <= 10^9$ and

$$Nu = 1.3\left(T_h - T_c\right)^{\frac{1}{3}}\frac{H}{k} \tag{2.11.9}$$

for $10^9 < Gr <= 10^{12}$.

Figure 2.22 shows Nusselt numbers for the different correlations for the same computer simulation of the reactor. The radiation shield and the concrete structure are 180 mm apart. The heat input was kept at 1900 kW for all the simulations. As can be seen from the figure, Eckert and Carlson (1961) predicts a very high Nusselt number, almost 4 times greater than what Mills (1999) suggests. It is important to notice that Dobson and Ruppersberg (2006) calculates Nusselt numbers for each surface, while Eckert and Carlson (1961) and Mills (1999) uses only one Nusselt number to describe the convection between the two surfaces. Dobson and Ruppersberg (2006) gives more or less the same result for the Nusselt numbers on both the hot and cold surfaces. The values are slightly higher than the value Mills (1999) found. Although Eckert and Drake (1972) do not calculate a Nusselt number, an *equivalent* Nusselt number has been calculated and is also shown in figure 2.22. This *equivalent* Nusselt number is more of less the average of what Eckert and Carlson (1961) and Dobson and Ruppersberg (2006) found.

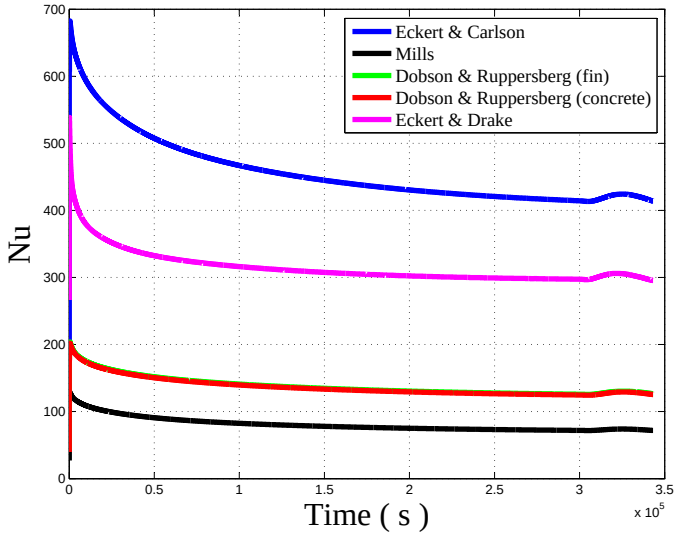

Figure 2.22: *Nu* numbers using different correlations

All these Nusselt numbers will be evaluated against the experimental results. The correlation that fits the experimental results best will be used in the further analysis and optimisation of the RCCS. A loss factor will also be used to approximate the losses through the narrow openings between the different components of the experimental apparatus. This loss factor will be multiplied with the Nusselt numbers to get more accurate results. The loss factor will also account for the fact that the enclosed cavity in the experiment has a finite width and all the Nusselt number correlations given in this section assume an infinitely wide enclosure.

2.12 Simplifying assumptions for modelling a closed loop thermosyphon heat pipe

CLTHPs have been used for numerous applications such as water heating and cooling of electronic equipment. Many experimental and theoretical studies have been done on CLTHPs. A major problem with CLTHPs is the theoretical modelling, because of numerical instabilities. Numerical instabilities in the theoretical model will be eliminated by

simplifying the model. In order to simplify the numerical model, Welander (1967) suggest that the following assumptions are made:

- The Boussinesq approximation.
- The tangential force on the working fluid is proportional to the instantaneous flow rate.
- The temperature of the working fluid is uniform over its cross section.

These approximations allow the formulation of a one dimensional model of a CLTHP. The instantaneous flow rate is the average 1D velocity of the fluid. Molz *et al.* (2004) also assumes quasi-static conditions for the CLTHP. Ambrosini and Ferreri (2000) uses the same approximations as Welander (1967) but also assumes that the horizontal pipes are adiabatic. Khodabandeh (2005) and McKee (1970) assumes that the flow inside the CLTHP is homogeneous. This implies that the gas and liquid velocities are the same.

This literature study resulted in a better understanding of the layout and design of the current PBMR RCCS, the functional requirements of an RCCS and in particular, the heat load on the RCCS during emergency shut-down conditions of the PBMR. Problem areas in the modelling of the RCCS such as the equivalent thermal conductivity of the reactor core, the different radiation view factors and the modelling of natural convection in enclosed rectangles has been investigated. This research can now be implemented and a theoretical model of the RCCS can be created.

Chapter 3

Theory

This chapter shows how the theoretical model of the heat flow from the reactor core via the radiation heat shield and the closed loop thermosyphon heat pipes (CLTHPs) to the environment and from the reactor core via the radiation heat shield through the concrete structure to the environment was obtained. The chapter starts with the background theory allowing a better understanding of the simplifying assumptions that were made in modelling the thermosyphon loop. The governing equations for the heat and mass flow in the thermosyphon are then derived from the basic laws of mechanics.

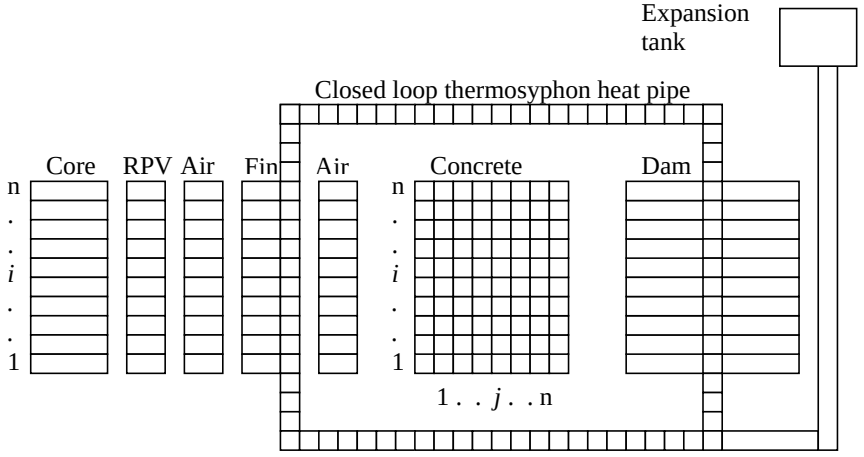

Figure 3.1: Nodalization for the theoretical model

The nodalization for the theoretical model can be seen in figure 3.1. The figure shows the reactor core with the RPV next to it. There is an air gap between the RPV and the fins which are attached to the risers of the closed loop thermosyphon heat pipe. The closed loop thermosyphon heat pipes are placed around the concrete structure. The downcomers are placed inside the cooling dam. Each thermosyphon is also fitted with an expansion tank. The temperatures of the reactor core, the RPV, the fins and the air gaps are assumed to be constant in the horizontal direction. The concrete structure has a 2D temperature distribution. In the figures in the rest of this chapter, the ith elements are two elements on the same horizontal level as shown in figure 3.1.

3.1 Mathematical modelling of the heat transfer from the reactor core to the fins and into the working fluid

3.1.1 Heat generation in the reactor core and the heat transfer from the reactor core to the RPV

The heat load on the RCCS for normal operating conditions is $Q_{load} = 1966$ kW as given in Section 2.5 and

$$Q_{decay} = 0.0622 Q_{normal} t^{-0.2}$$

as given in Section 2.6.3 for the emergency shut-down condition. Note that Q_{load} and Q_{decay} is the same variable in the theoretical model called Q_{in}.

The heat transferred from the core to the RPV is calculated as follows:

$$Q_{core-RPV} = UA(T_{core} - T_{RPV}) \tag{3.1.1}$$

where the overall heat transfer coefficient is $U = k_{eff}/dr$.

A is the surface area of the RPV and dr is the distance from the centre of the reactor core to the inside surface of the RPV.

The effective thermal conductivity is used as shown in figure 2.10 and is described by the following relation to core temperature:

$$k_{eff} = 0.000002857142857 T_{core}^2 + 0.019428571428571 T_{core} - 3.0$$

3.1.2 Heat transfer from the RPV to the fins

Consider the heat transfer between the ith elements of the RPV and the radiation heat shield as shown in figure 3.2. There is a convection thermal resistance between the RPV surface and the air as well as a convection thermal resistance between the air and the radiation heat shield surface. There is also a radiation thermal resistance.

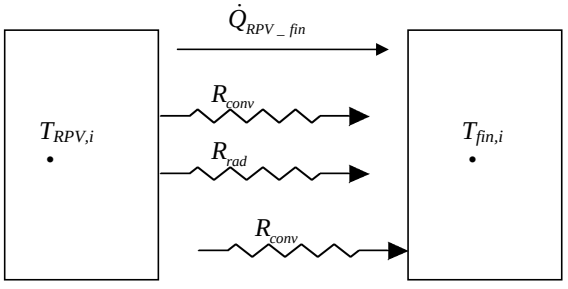

Figure 3.2: Heat transfer between the RPV and the fins

The radiation thermal resistance is given, as found in Çengel (2003), by:

$$R_{rad} = \frac{1}{\sigma}\left\{\frac{1-\varepsilon_{RPV}}{\varepsilon_{RPV} A_{z,RPV}} + \frac{1}{\mathcal{F}_{rf} A_{z,RPV}} + \frac{1-\varepsilon_{fin}}{\varepsilon_{fin} A_{z,RPV}}\right\}$$

The convection resistance on the RPV is given by:

$$R_{conv,1} = \frac{1}{h_1 A_{z,RPV}}$$

where

$$h_1 = 0.001 + \left(1.07\left(T_{RPV} - T_{air}\right)\frac{1}{L}\right)^{1/4}$$

for laminar flow and

$$h_1 = 0.001 + \left(1.3\left(T_{RPV} - T_{air}\right)\frac{1}{L}\right)^{1/3}$$

for turbulent flow as given by Dobson and Ruppersberg (2006). L is the vertical length of the element.

The convection resistance on the fins is given by:

$$R_{conv,2} = \frac{1}{h_2 A_{z,RPV}}$$

where h_2 is calculated exactly like h_1.

The total thermal resistance is then given by:

$$R_{thermal} = \left(\frac{1}{R_{conv,1} + R_{conv,2}} + \frac{1}{R_{rad}}\right)^{-1}$$

The heat transfer from the RPV to the fins is given by:

$$Q_{RPV-fins} = \frac{T_{RPV} - T_{fins}}{R_{thermal}} \tag{3.1.2}$$

3.1.3 Heat transfer from the fins to the working fluid in the closed loop thermosyphon heat pipe

The flow of heat from the fin to the water in the thermosyphon can be indicated as shown in figure 3.3. The temperatures of the fin and the water are known as well as the mass flow rate. The objective is to calculate the $Q_{fin-water}$ term. This will be the quantity used as the Q_{in} in equation (3.2.20).

The Reynolds number is given by

$$Re = \frac{4\dot{m}}{\pi\mu D}$$

For laminar flow, the inside heat transfer coefficient h_i is given by Çengel (2003) as

$$h_{lam} = 4.36\frac{k}{D}$$

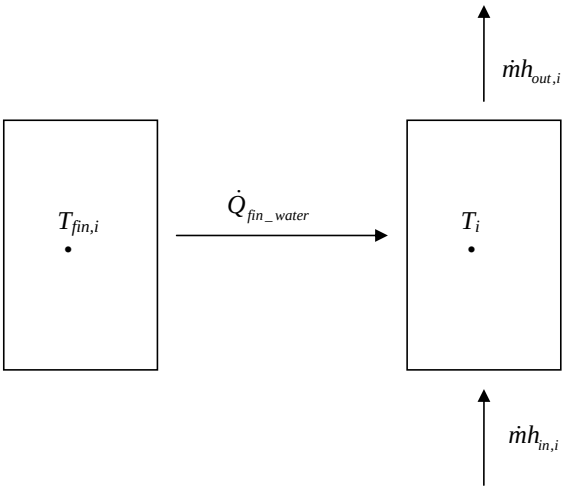

Figure 3.3: Heat transfer between the fins and the thermosyphon

For turbulent flow, the inside heat transfer coefficient h_i is given by Çengel (2003) as

$$h_{turb} = 0.023\frac{k}{D}Re^{0.8}Pr^{0.35}$$

The thermal resistance is then given by:

$$R_{thermal} = \frac{1}{h_i A_z}$$

The heat transfer from the fin to the thermosyphon is then given by:

$$Q_{fin-water} = \frac{\eta_{fin}\left(T_{fin} - T_{water}\right)}{R} \tag{3.1.3}$$

where η_{fin} is the fin efficiency.

3.2 Mathematical modelling of the heat- and mass transfer in the closed loop thermosyphon heat pipe

The flow in the thermosyphon is assumed to be quasi-static. A quasi-static, or quasi-equilibrium, process is when a process proceeds in such a manner that the system remains infinitesimally close to an equilibrium state at all times (Çengel and Boles, 2002).

In gas flows, one must be aware of compressibility effects. Compressibility effects refer to significant density changes of the fluid caused by the flow. These compressibility effects become important in the flow analysis when the flow velocity reaches a significant fraction of the speed of sound of the fluid. White (2003) shows that if the Mach number, $Ma = V/a$, of a fluid reaches 0.3, compressibility effects should be accounted for. The average velocity of the working fluid is orders less than the speed of sound in the working fluid in the closed loop thermosyphon, thus it is acceptable to assume incompressible flow for the mathematical analysis of the flow in the CLTHPs (White, 2003).

The quasi equilibrium process assumption is applicable to the modelling of the CLTHP because the average velocity of the working fluid is orders less than the speed of sound in the working fluid around the loop. This means that the rate at which pressure waves propagate around the loop is much faster than the rate of heat and mass transfer around the loop. This implies that the transient behaviour of the flow in the thermosyphon can be approximated with a steady state analysis at each time step. The quasi equilibrium process assumption was used by Molz *et al.* (2004), Reimann *et al.* (2006) and Dobson and Ruppersberg (2006).

These simplifying assumptions and those given in Section 2.12 were used to derive the governing differential equations to form a mathematical model of the CLTHP with its expansion tank.

There are three governing equations that need to be solved to form the mathematical model. These are listed and defined below as done by White (2003).

Conservation of mass:

$$\frac{dm}{dt} = 0 \tag{3.2.1}$$

Newton's second law:

$$\overrightarrow{F} = m\overrightarrow{a} = \frac{d}{dt}\left(m\overrightarrow{v}\right) \tag{3.2.2}$$

The first law of thermodynamics:

$$\frac{dQ}{dt} - \frac{dW}{dt} = \frac{dE}{dt} \tag{3.2.3}$$

These equations are known as the laws of mechanics. Newton's second law is also known as the momentum equation and the first law of thermodynamics is also known as the energy equation.

All the laws of mechanics are written for a system, which is defined as an arbitrary quantity of mass of fixed identity. The mathematical model of the CLTHP cannot be built using system analysis because it is necessary to derive explicit formulations suitable for computer programming. This requires the use of fixed control volumes for the formulation of the equations. To convert a system analysis to a control volume analysis, it is necessary to convert the mathematics to apply to a specific region rather than to an individual fixed mass. This conversion is called the Reynolds transport theorem and it can be applied to all the basic laws of mechanics. The Reynolds transport theorem for a one dimensional fixed control volume is

$$\frac{d}{dt}\left(B_{sys}\right) = \frac{d}{dt}\left(\int_{CV} \beta\rho \,\mathrm{d}V\right) + \left(\beta\rho A\nu\right)_{out} - \left(\beta\rho A\nu\right)_{in} \tag{3.2.4}$$

where B is any property and β is the intensive value, or amount per unit mass, of that property (White, 2003).

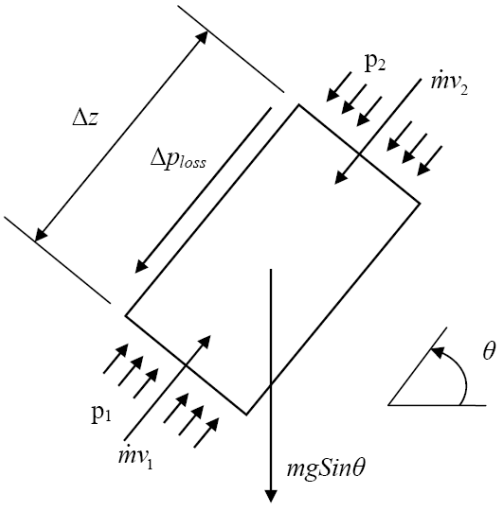

Figure 3.4: Conservation of momentum in the working fluid

Equations (3.2.1) to (3.2.3) can be converted to apply to control volumes, by using the Reynolds transport theorem (Equation (3.2.4)), into the following forms:

Conservation of mass:

$$\int_{CV} \frac{\delta \rho}{\delta t} dV + \Sigma \left(\rho A v\right)_{out} - \Sigma \left(\rho A v\right)_{in} = 0 \tag{3.2.5}$$

Newton's second law:

$$\frac{d}{dt}\left(mv\right)_{sys} = \Sigma F = \frac{d}{dt}\left(\int_{CV} \nu \rho dV\right) + \left(\dot{m}v\right)_{out} - \left(\dot{m}v\right)_{in} \tag{3.2.6}$$

The first law of thermodynamics:

$$\frac{dQ}{dt} - \frac{dW}{dt} = \frac{dE}{dt} = \frac{d}{dt}\left(\int_{CV} e\rho dV\right) + \left(e\rho A v\right)_{out} - \left(e\rho A v\right)_{in} \tag{3.2.7}$$

where $e = u + \frac{v^2}{2} + gz$

The governing equations can now be used to set up the difference equations for the control volumes that will be used in the computer program. Figure 3.4 shows all the forces acting on the working fluid inside the CLTHP. The conservation of momentum equation can now be applied to the working fluid in order to calculate the mass flow rate of the water in the CLTHP and the interface pressures between the control volumes.

The conservation of momentum equation makes it possible to derive a difference equation for the mass flow rate of the working fluid in each control volume. The derivation is

shown below with the use of figure 3.4.

$$\Sigma F_z = \frac{\delta mv}{\delta t} + \dot{m}v_2 - \dot{m}v_1 \tag{3.2.8}$$

$$\frac{\delta mv}{\delta t} = \Sigma F_z - \dot{m}v_2 + \dot{m}v_1 \tag{3.2.9}$$

$$\frac{\delta mv}{\delta t} = p_1 A_x - p_2 A_x - mgSin\theta - \Delta p_{loss} A_x - \dot{m}v_2 + \dot{m}v_1 \tag{3.2.10}$$

The pressure loss term accounts for pressure losses in the pipe due to friction as well as minor losses in the elbows and is given by the following:

$$\Delta p_{loss} = \frac{f\Delta z\rho v^2}{2d} + \frac{K\rho v^2}{2}$$

where f is the friction factor and K is the loss coefficient for the elbows.

Using the chain rule for the derivative and $v = \dot{m}/(\rho A_x)$, the momentum equation can now be written as follows:

$$m\frac{\delta v}{\delta t} = (p_1 - p_2) A_x - \Delta p_{loss} A_x + \dot{m}\left(\frac{\dot{m}}{\rho_1 A_x} - \frac{\dot{m}}{\rho_2 A_x}\right) - \rho A_x \Delta z g Sin\theta - \frac{\dot{m}}{\rho A_x}\frac{\delta m}{\delta t} \tag{3.2.11}$$

Equation (3.2.11) is written in units of force. The mass flow rate in the thermosyphon is dependent on the pressure differences across each of the elements. It is therefore necessary to convert the equation to have units of pressure, thus dividing it by the cross sectional area, A_x, to give:

$$\frac{m}{A_x}\frac{\delta v}{\delta t} = p_1 - p_2 - \Delta p_{loss} + \left(\frac{\dot{m}}{A_x}\right)^2\left(\frac{1}{\rho_1} - \frac{1}{\rho_2}\right) - \rho\Delta z g Sin\theta - \frac{\dot{m}}{\rho A_x^2}\frac{\delta m}{\delta t} \tag{3.2.12}$$

Equation (3.2.12) can be used to calculate the interface pressures between elements as shown in equation (3.2.13). For each element the subscripts 1 and 2 in the pressure and density terms denotes the inlet and outlet conditions. The outlet pressure of the first element is the inlet pressure of the second element. The outlet pressure of the second element is the inlet pressure of the third element and so fourth.

$$p_2 = p_1 - \frac{m}{A_x}\frac{\delta v}{\delta t} - \Delta p_{loss} + \left(\frac{\dot{m}}{A_x}\right)^2\left(\frac{1}{\rho_1} - \frac{1}{\rho_2}\right) - \rho\Delta z g Sin\theta - \frac{\dot{m}}{\rho A_x^2}\frac{\delta m}{\delta t} \tag{3.2.13}$$

An explicit equation for the fluid velocity is found by integrating (3.2.13) around the thermosyphon loop. The result of this is given by equation (3.2.14).

$$v^{t+\Delta t} = v^t + \frac{\Delta t}{\Sigma\frac{m_i}{A_x}}\left[\Sigma\left(p_{i-1} - p_{i+1}\right) - \Sigma\Delta p_{loss,i} + \Sigma\left(\frac{\dot{m}}{A_x}\right)^2\left(\frac{1}{\rho_{i-1}} - \frac{1}{\rho_{i+1}}\right) - \Sigma\rho_i\Delta z_i g Sin\theta_i - \Sigma\frac{\dot{m}}{\rho_i A_x^2}\frac{\delta m_i}{\delta t}\right] \tag{3.2.14}$$

The last equation can be simplified by noting that the integral of the pressure difference term will always be zero. By using the Boussinesq approximation (see Appendix B) for single phase flow, the density difference term is zero.

The explicit formulation for mass flow rate can now be given as:

$$\dot{m}^{t+\Delta t} = \rho A_x v^{t+\Delta t} \tag{3.2.15}$$

Figure 3.5 shows the energy flowing in and out of the working fluid inside the CLTHP. The energy equation can now be applied to the working fluid in order to calculate the temperature of working fluid in the CLTHP.

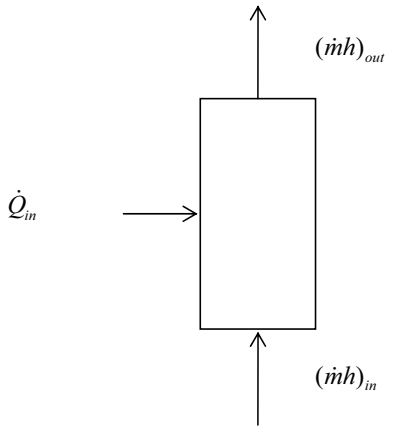

Figure 3.5: Conservation of energy in the working fluid

The conservation of energy equation makes it possible to derive a difference equation for the temperature of the working fluid in each control volume. The derivation is shown below with the use of figure 3.5. The first law of thermodynamics as given in equation (3.2.7) can be rewritten in the following form as given by Çengel and Boles (2002).

$$\dot{Q}_{in} - \dot{Q}_{out} + \dot{W}_{in} - \dot{W}_{out} + \Sigma\dot{m}\left(h_{in} - h_{out} + \frac{V_{in}^2 - V_{out}^2}{2} + g\left(z_{in} - z_{out}\right)\right) = \frac{\delta U}{\delta t} \tag{3.2.16}$$

Cancellation of the irrelevant terms in equation (3.2.16) shows that the first law of thermodynamics for the control volume reduces to:

$$\dot{Q}_{in} + (\dot{m}h)_{in} - (\dot{m}h)_{out} = \frac{\delta U}{\delta t} \tag{3.2.17}$$

where $\delta U = U_2 - U_1$

Using the chain rule for the derivative and the relation $U = mu$ in equation (3.2.17), it is possible to derive an explicit relation for the internal energy of the working fluid at the next time step and then determine the new time step temperature of the working fluid. This derivation is shown below.

$$m\frac{\delta u}{\delta t} + u\frac{\delta m}{\delta t} = \dot{Q}_{in} + \dot{m}\left(h_{in} - h_{out}\right) \tag{3.2.18}$$

$$\frac{\delta u}{\delta t} = \frac{1}{m}\left[\dot{Q}_{in} + \dot{m}\left(h_{in} - h_{out}\right) - u\frac{\delta m}{\delta t}\right] \tag{3.2.19}$$

$$u_i^{t+\Delta t} = u_i^t + \frac{\Delta t}{m_i}\left[\dot{Q}_{in} + \dot{m}\left(h_{in} - h_{out}\right) - u_i^t\frac{\delta m_i}{\delta t}\right] \tag{3.2.20}$$

The temperature of the working fluid at the next time step can be determined using:

$$T_i^{t+\Delta t} = \frac{u_i^{t+\Delta t}}{c_v} \tag{3.2.21}$$

This derivation was done assuming that there would be a heat flow into the control volume. For the elements in the mathematical model of the CLTHP where there is a net heat outflow, the equations would stay exactly the same. The only difference is that the $\dot{Q}_{in}$ term would be a negative quantity indicating the outflow of heat from the element. Also, the derivation assumes that the working fluid is in single phase. The following logic expressions are built into the model to calculate the temperature and mass fraction if the working fluid is a liquid-vapour mixture:

If $u_i^{t+\Delta t} \leq u_f$, then

$T_i^{t+\Delta t} = \frac{u_i^{t+\Delta t}}{c_v}$ and $x_i^{t+\Delta t} = 0$
If $u_i^{t+\Delta t} > u_f$, then

$T_i^{t+\Delta t} = T_{Sat@P_i}$ and $x_i^{t+\Delta t} = \frac{u_i^{t+\Delta t} - u_{f,i}^{t+\Delta t}}{u_{fg,i}^{t+\Delta t}}$

where $u_{f,i}^{t+\Delta t} = c_v T_{Sat,i}^{t+\Delta t}$

3.3 Mathematical modelling of the heat transfer from the RCCS to the environment

3.3.1 Heat transfer from the fins to the concrete structure

Not all the heat transferred from the RPV to the HS will be removed from the HS by the CLTHP. The reason for this is that the fins will not have a 100 % fin-efficiency, and there will be some heat transferred from the back of the fins to the surrounding concrete structure. The heat transfer from the back of the fins to the concrete structure can be illustrated as in figure 3.6. There is a convection thermal resistance on the fins as well as on the concrete structure. There is also a radiation thermal resistance.

The radiation thermal resistance is given, as found in Çengel (2003), by:

$$R_{rad} = \frac{1}{\sigma}\left\{\frac{1-\varepsilon_{fin}}{\varepsilon_{fin}A_{z,fin}} + \frac{1}{\mathcal{F}_{fc}A_{z,fin}} + \frac{1-\varepsilon_{concrete}}{\varepsilon_{fin}A_{z,RPV}}\right\}$$

The convection resistance on the fins is given by:

$$R_{conv,1} = \frac{1}{h_1 A_{z,fin}}$$

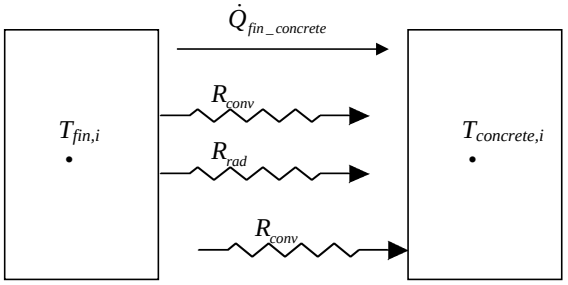

Figure 3.6: Heat transfer between the fins and the concrete structure

where

$$h_1 = 0.001 + \left(1.07\left(T_{fin} - T_{air}\right)\frac{1}{L}\right)^{1/4}$$

for laminar flow and

$$h_1 = 0.001 + \left(1.3\left(T_{fin} - T_{air}\right)\frac{1}{L}\right)^{1/3}$$

for turbulent flow.

The convection resistance on the concrete structure is given by:

$$R_{conv,2} = \frac{1}{h_2 A_{z,concrete}}$$

where h_2 is calculated exactly like h_1.

The total thermal resistance is then given by:

$$R_{thermal} = \left(\frac{1}{R_{conv,1} + R_{conv,2}} + \frac{1}{R_{rad}}\right)^{-1}$$

The heat transfer from the back of the fins to the concrete structure is given by:

$$Q_{fins-concrete} = \frac{T_{fin} - T_{concrete}}{R_{thermal}} \tag{3.3.1}$$

3.3.2 Temperature distribution in the concrete structure

The concrete structure is divided into control volumes in both the horizontal and vertical directions. Since the modelling of the heat transfer is only one dimensional, the heat transfer from the control volumes above and below the control volume in question are ignored as $\frac{\delta T}{\delta z} = 0$. The control volumes of the concrete structure can be seen in figure 3.7.

The temperature distribution in the concrete structure is modelled by using 3 different control volumes. One for the inside surface, one for all the interior control volumes and one for the exterior surface. The number of interior nodes can be hard coded into the

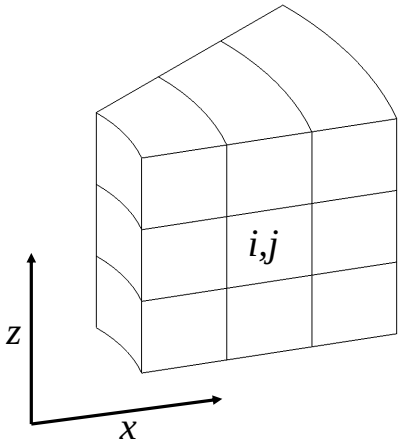

Figure 3.7: Control volumes in the concrete structure

computer model. The width of each control volume is determined by the number of CLTHPs used in the computer model as shown by figure 3.8. The width of the control volumes is proportional to the number of CLTHPs used as can be seen from equation (3.3.2). The curved surfaces on the inside and outside radii of the control volumes are assumed to be flat. This assumption is made to simplify the calculation of the radiation view factors.

$$W_{CV} = \frac{D_{CS}}{n_{CLT}} \tag{3.3.2}$$

where W_{CS} is the width of the concrete structure control volume, D_{CS} is the diameter of the concrete structure and n_{CLT} is the number of closed loop thermosyphons used in the model.

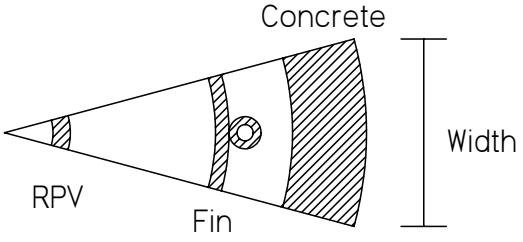

Figure 3.8: Top view of a concrete structure control volume

The temperature of the inside surface of the concrete structure is obtained with the use of figure 3.9. The $\dot{Q}_{fins-concrete}$ term is obtained in Section 3.3.1. The conduction term models the heat flow into or out of the interior control volume next to the surface control volume.

By using an explicit method to calculate the temperatures in the model for each time step, it is possible to calculate the temperature of the concrete structure surface in the following manner:

The conduction term is given by

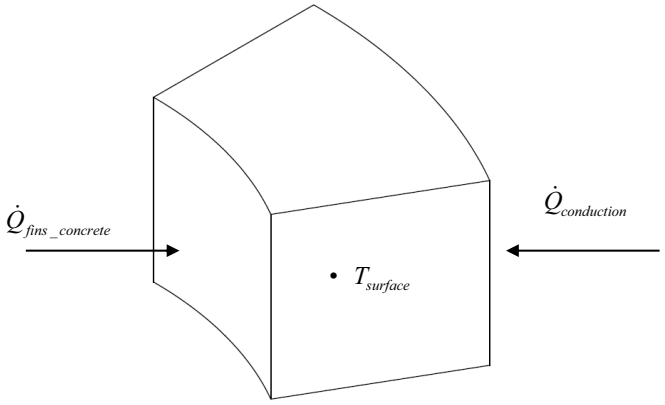

Figure 3.9: Temperature on the inside surface of the concrete structure

$$\dot{Q}_{cond} = \frac{T_1^t - T_2^t}{R}$$

where T_1^t denotes the temperature of the first control volume in the horizontal, or radial, direction, i.e. the surface control volume, at a given time step and T_2^t denotes the temperature of the second control volume in the horizontal direction, i.e. the first interior control volume, at a given time step.

The thermal resistance is calculated by using the inside and outside radii of each control volume (denoted by $rcs(j-1)$ and $rcs(j)$) and is given by

$$R = \frac{\frac{rcs(1)-rcs(0)}{2} + \frac{rcs(2)-rcs(1)}{2}}{k_{cs}A_{cs}}$$

where

$$A_{cs} = \frac{2\pi L rcs(1)}{Nhp}$$

The temperature of the control volume for the inside surface at the new time step is then given by

$$T_i^{t+\triangle t} = T_i^t + \frac{\triangle t}{m_{cs}c_{p,cs}}\left(\dot{Q}_{fins-concrete} - \dot{Q}_{cond}\right) \tag{3.3.3}$$

The temperatures of the interior control volumes of the concrete structure are obtained with the use of figure 3.10. There is a conduction heat transfer term from the left and right. The computer program loops through all the nodes by using j as a counter. The $j+1$ temperature will be the j temperature for the next control volume. In this manner, all the temperatures of the interior control volumes are calculated one at a time for each time step. The $rcs(j)$ terms in the following equations denotes the radius of the concrete structure at the interface between adjacent control volumes.

The conduction from the left hand control volume can be modelled as follows:

$$\dot{Q}_L = \frac{T_{j-1}^t - T_j^t}{R_L}$$

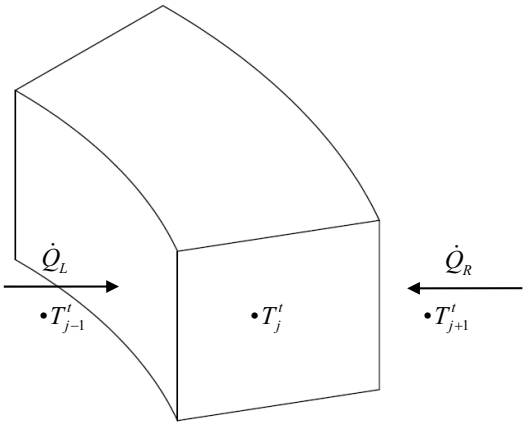

Figure 3.10: Heat transfer of the interior control volumes of the concrete structure

where R_L is given by

$$R_L = \left(\frac{rcs(j-1) - rcs(j-2)}{2} + \frac{rcs(j) - rcs(j-1)}{2} \right) \frac{1}{k_{cs} A_{cs,j-1}}$$

and

$$A_{cs,j-1} = \frac{2\pi rcs(j-1)L}{Nhp}$$

The conduction from the right hand control volume can be modelled as follows:

$$\dot{Q}_R = \frac{T^t_j - T^t_{j+1}}{R_R}$$

where R_R is given by

$$R_R = \left(\frac{rcs(j) - rcs(j-1)}{2} + \frac{rcs(j+1) - rcs(j)}{2} \right) \frac{1}{k_{cs} A_{cs,j}}$$

and

$$A_{cs,j} = \frac{2\pi rcs(j)L}{Nhp}$$

Figure 3.11 shows five adjacent control volumes in the concrete structure. This figure will explain how the resistance terms in the previous equations were determined.

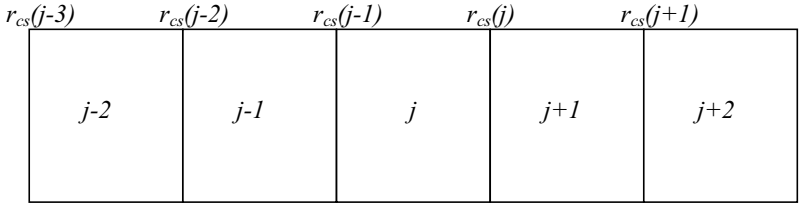

Figure 3.11: Five interior control volumes of the concrete structure

The temperatures of the interior control volumes at the new time step are then given by

$$T_j^{t+\triangle t} = T_j^t + \frac{\triangle t}{m_{cs} c_{p,cs}} \left(\dot{Q}_L - \dot{Q}_R \right) \tag{3.3.4}$$

The heat transfer into and out of the control volume of the outer surface of the concrete structure can be seen in figure 3.12. There is conduction from the interior node and a heat transfer term on the outside surface to the environment. This heat transfer is convection heat transfer only. The last control volume is denoted by n.

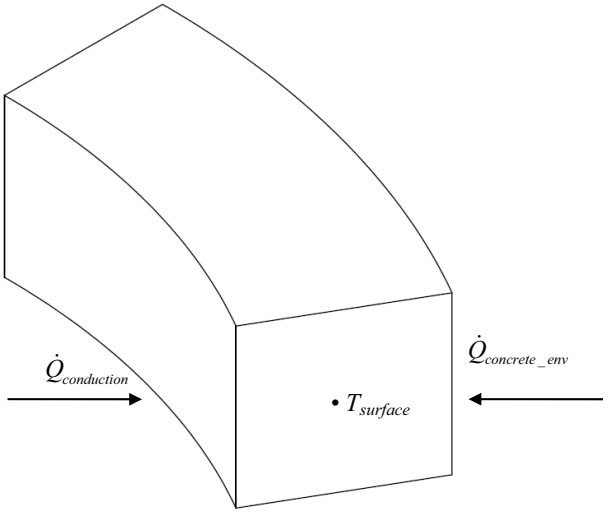

Figure 3.12: Temperature on the outside surface of the concrete structure

The conduction from the left hand control volume can be modelled as follows:

$$\dot{Q}_L = \frac{T_{n-1}^t - T_n^t}{R_L}$$

where R_L is given by

$$R_L = \left(\frac{rcs(n-1) - rcs(n-2)}{2} + \frac{rcs(n) - rcs(n-1)}{2} \right) \frac{1}{k_{cs} A_{cs,n-1}}$$

and

$$A_{cs,n-1} = \frac{2\pi rcs(n-1)L}{Nhp}$$

The convection heat transfer on the outside surface is given by

$$\dot{Q}_{conv} = \frac{T_n^t - T_{env}^t}{R_{conv}}$$

where R_{conv} is given by

$$R_{conv} = \frac{1}{h_{conv} A_{cs,n}}$$

The heat transfer coefficient is calculated in the same manner as in Section 3.3.1. The new temperature of the outside surface of the concrete structure is then given by:

$$T_n^{t+\triangle t} = T_n^t + \frac{\triangle t}{m_{cs} c_{p,cs}} \left(\dot{Q}_L - \dot{Q}_{conv} \right) \tag{3.3.5}$$

3.3.3 Heat transfer from the downcomers of the CLTHPs to the cooling dam

The flow of heat from the water in the CLTHPs to the water in the cooling dam can be seen in figure 3.13. The temperatures of the water in the CLTHP and the cooling dam are known as well as the mass flow rate. The objective is to calculate the $Q_{water-dam}$ term.

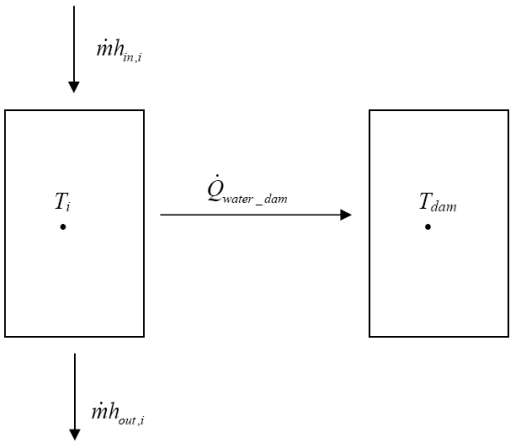

Figure 3.13: Heat transfer between the thermosyphon and the cooling dam

The Reynolds number and the heat transfer coefficient on the inside surface of the CLTHP is calculated in the same manner as discussed in Section 3.1.3. The heat transfer coefficient on the outside of the thermosyphon is calculated, as given by Çengel (2003) as:

$$h_{out} = \frac{k}{L} \left\{ 0.825 + \frac{0.387 Ra^{1/6}}{\left[1 + (0.492/Pr)^{9/16} \right]^{8/27}} \right\}^2 \tag{3.3.6}$$

The thermal resistance between the water in the CLTHP and the water in the cooling dam is compiled of two convection resistances and one conduction resistance through the wall thickness of the CLTHP. The total thermal resistance is given by:

$$R_{thermal} = \frac{1}{h_{in} A_z} + \frac{ln \frac{d_o}{d_i}}{2\pi L k} + \frac{1}{h_{out} A_z}$$

The heat transfer from the CLTHP to the cooling dam is then given by:

$$\dot{Q}_{water-dam} = \frac{T_{water} - T_{dam}}{R_{thermal}} \tag{3.3.7}$$

3.3.4 Heat transfer from the cooling dam to the environment

It is assumed that the condenser section of the CLTHP is placed in the middle of a cooling dam, on the outside of the rector building. The water in the dam is open to the environment and transports the heat removed from the CLTHPs to the environment. A simplified model of the heat transfer in the cooling dam and to the environment can be seen in figure 3.14. The figure shows a cross section of the dam with the condenser side of a CLTHP standing in it. As can be seen in the figure, the temperature distribution in the water is assumed to be uniform in the horizontal direction. The heat transfer on the surface of the water consist of the solar radiation incident from the sun, a heat loss from evaporation and convection caused by ambient air flowing over the water surface. The final heat loss is a small radiation heat loss.

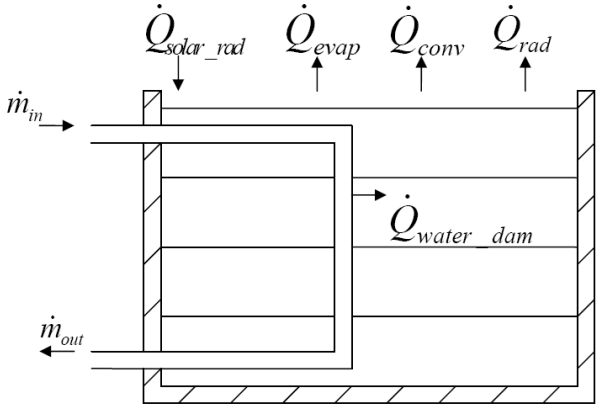

Figure 3.14: Heat transfer between the dam and the environment

The incident solar radiation is assumed to have a constant flux per unit area and is given by

$$\dot{Q}_{solarrad} = 333 A_{z_{dam}} \tag{3.3.8}$$

The rate of evaporation, as given by Chinnery (1973), is given by

$$\dot{m}_{evap} = 6.69e^{-11}(1.47 - 5.49e^{-6}P_{atm})(0.44 + 0.204V_{wind})(P_{sat@T_{dam}} - P_v)\rho_{dam}A_{z_{dam}}$$

The heat loss through evaporation is then given by

$$\dot{Q}_{evap} = \dot{m}_{evap}h_{fg} \tag{3.3.9}$$

The convection heat loss is given by

$$\dot{Q}_{conv} = (1 + V_{wind})h_{conv}A_{z_{dam}}(T_{env} - T_{dam}) \tag{3.3.10}$$

where the heat transfer coefficient, h_{conv}, is given by Chinnery (1973) as

$$h_{conv} = 2.5(T_{env} - T_{dam})^{\frac{1}{4}}$$

There is also a radiation heat loss from the surface of the water to the sky. This is because the effective sky temperature will always be slightly lower than the water temperature. The sky emissivity is given by Mills (1999) as

$\epsilon_{sky} = 0.727 + 0.0016 T_{dp}$ during the day and $\epsilon_{sky} = 0.741 + 0.00162 T_{dp}$ during the night.

T_{dp} is the dew point temperature of the environment. The effective sky temperature is then given by Mills (1999) as:

$$T_{sky} = \epsilon_{sky} \left[(T_{env} + 273.15)^4 \right]^{\frac{1}{4}} - 273.15$$

The radiation heat transfer from the surface can be given by

$$\dot{Q}_{rad} = \epsilon_{dam} A_{z_{dam}} \sigma \left[(T_{dam} + 273.15)^4 - (T_{sky} + 273.15)^4 \right] \tag{3.3.11}$$

The net heat transfer to the environment can be given by

$$\dot{Q}_{net_{dam_{env}}} = \dot{Q}_{evap} + \dot{Q}_{conv} + \dot{Q}_{rad} - \dot{Q}_{solarrad} \tag{3.3.12}$$

The net heat transfer into the water in the dam can be given by

$$\dot{Q}_{net_{dam}} = \dot{Q}_{water_dam} - \dot{Q}_{net_{dam_{env}}} \tag{3.3.13}$$

The new dam temperatures can then be given by

$$T_{dam}^{t+\triangle t} = T_{dam}^{t} + \triangle t \frac{\dot{Q}_{net_{dam}}}{m_{dam} c_{v_{dam}}} \tag{3.3.14}$$

3.4 Summary

A control volume approach has been used in order to create a theoretical model of the heat transfer from the reactor core to the RPV, from the RPV to the HS and from the HS to the working fluid in the closed loop thermosyphon heat pipes. The heat transfer from the back of the HS to the concrete structure has also been investigated and modelled. The closed loop thermosyphon heat pipe has been modelled using the simplifying assumptions given in Section 2.12. The heat transfer to and from the cooling dam has also been analysed. The mathematical equations derived in this chapter will now be used to create a computer program that will simulate the performance of a RCCS.

Chapter 4

Computer Program

The numerical model for the heat transfer simulation of the RCCS was written in PowerBASIC™ (2008). This chapter shows the calculation procedure and the grid size determination for the theoretical model. A sample calculation for the first time step is given at the end of the chapter. A sample input file to the computer program can be seen in Appendix E.

4.1 Program algorithm

The program algorithm consists of two sections. The first is the set-up section where time t equals zero. The second section is called the time loop where all values are replaced by newly calculated values for each time step. The set-up section includes the following:

a) Define all variables.

b) Read the input file and create and open all the output files.

c) Create all elements and give them all geometrical properties and initial thermodynamic properties.

d) Set the initial mass flow rate to zero and calculate the initial element interface pressures and corresponding saturation temperatures.

The time loop has the following steps:

1. Set environment temperature to day or night temperature depending on t.
2. Check flow regime and set laminar and turbulent flow switches accordingly.
3. Calculate the new core, RPV and fin temperatures.
4. Calculate the new temperature of the air between the RPV and the fin.
5. Calculate the new temperature of the concrete structure inside surface.
6. Calculate the new temperature of the air between the fin and the concrete structure.
7. Calculate the new temperature distribution in the concrete structure and the new outside surface temperature.
8. Calculate the net heat transfer into each element of the CLTHP.

9. Calculate the new cooling dam temperatures.
10. Calculate the new temperatures and mass fractions for the CLTHP.
11. Calculate the new densities, masses and void fractions for the CLTHP. Void fraction is calculated with
$$\alpha = \left(1 + \frac{1-x}{x}\frac{\rho_g}{\rho_l}\right)^{-1}$$
The density is then given by $\rho = \alpha\rho_g + (1-\alpha)\rho_l$
12. Calculate the new expansion tank temperature and water level.
13. Calculate the new mass flow rate.
14. Calculate the new element interface pressures and corresponding saturation temperatures.
15. Replace all old values with the new values.
16. Increase the time with the time step, $t = t + \Delta t$.
17. Go to the start of the time loop.

4.2 Grid independence

The computer program allows the user to select the number of elements that each of the four pipes in the CLTHP must be divided into and thereby selecting the grid, or element, size. The element size for each pipe is simply the length of the pipe divided by the chosen number of elements for the pipe. The size of the elements will influence the results of each simulation. It is therefore necessary to do a sensitivity analysis of the grid size. The grid size must be kept as small as possible in order to minimize simulation time, but large enough to give accurate, or conservative results.

The first step was to decide on an appropriate grid size for single phase flow in the CLTHPs. This was done by keeping the vertical pipes' number of elements constant and comparing the results for when the horizontal pipes' number of elements are increased. The results are shown in Table 4.1.

Table 4.1: Inlet and outlet temperatures (in °C) of the horizontal pipes with different numbers of elements

	Bottom Pipe		Top Pipe	
Elements	Inlet	Outlet	Inlet	Outlet
2	54.7884	54.7882	72.8963	72.8962
4	54.7883	54.7881	72.8967	72.8965
8	54.7881	54.7878	72.8972	72.8970
16	54.7878	54.7875	72.8978	72.8976

Table 4.1 shows the inlet and outlet temperatures of the water inside the top and bottom pipes of the CLTHP for different grid sizes. As can be seen from the results, the

temperatures are almost constant for any number of elements. The simulation was done for $2x10^6$ iterations, or a 23 day simulation. The water remained in single phase. From the results obtained, it was decided that the top and bottom pipes should each have two elements if the flow is in single phase. The mass flow rate remained the same for all the simulations.

With the number of elements in the horizontal pipes fixed, the appropriate number of elements for the vertical pipes could be found. The same simulation was used as for the horizontal pipes. The results are shown in the Table 4.2.

Table 4.2: Inlet and outlet temperatures of the vertical pipes with different numbers of elements as well as the mass flow rate

	Hot Pipe		Cold Pipe		$\dot{m}(kg/s)$
Elements	Inlet	Outlet	Inlet	Outlet	
8	60.4405	74.7853	72.1074	58.3886	0.1180
12	56.2995	72.8964	70.8449	54.7886	0.1069
14	54.7090	72.0962	70.2526	53.3696	0.1034
24	49.1865	68.7878	67.7488	48.3244	0.0938
32	46.3310	67.1728	66.1852	45.6578	0.0901

As can be seen from Table 4.2, the temperatures and the mass flow rate in the thermosyphon drops with an increased grid size. The outlet temperature of the hot pipe is the most important temperature in the RCCS simulation since it is the maximum temperature in the CLTHP and is the maximum temperature that the concrete citadel could reach. It was decided to use 12 elements in the vertical pipes for single phase flow. This means that each element is 1 m long. This approach is considered conservative, because using more elements will result in a lower concrete structure temperature prediction. Using a smaller number of elements also decreases the simulation time of the computer model.

4.3 Sample calculation

A sample calculation for the temperatures calculated by the computer program is shown in Table 4.3. The initial temperatures are shown in the top section of the table. For this condition, the total simulation time t and the mass flow rate in the CLTHP are zero. The model has 8 elements in the vertical direction, meaning the CLTHP has 8 elements for each vertical pipe and 2 for the horizontal pipes. The concrete structure has 8 elements in the vertical direction and 12 elements in the horizontal direction. The CLTHP is indicated by the bold loop and the concrete structure by the bold square. The sample calculation shows only the calculated temperatures, since the temperatures are the main design variables for the RCCS. The time step was set to 10 s for the purpose of this sample calculation. The time step will be 1 s for normal simulations. The reason for having a 10 s time step for the sample calculation is to ensure temperature changes in the second decimal place. The temperatures for the first time step can be seen in the lower portion of the table.

Table 4.3: Sample calculation for the first time step

Time = 0 s											T_water in the Closed Loop Thermosyhon Heat Pipe										
Mass flow rate = 0 kg/s																					
							20									20					
T_Core	T_RPV	T_air	T_fin		T_air					Temperature Distribution in Concrete								T_env			T_Dam
1100	470	20	20	20	20	20	20.00808	20.02694	20.06735	20.17511	20.52532	21.33351	23.21929	24.70097	24.88955	24.97037	25	25		20	20
1100	470	20	20	20	20	20	20.00808	20.02694	20.06735	20.17511	20.52532	21.33351	23.21929	24.70097	24.88955	24.97037	25	25		20	20
1100	470	20	20	20	20	20	20.00808	20.02694	20.06735	20.17511	20.52532	21.33351	23.21929	24.70097	24.88955	24.97037	25	25		20	20
1100	470	20	20	20	20	20	20.00808	20.02694	20.06735	20.17511	20.52532	21.33351	23.21929	24.70097	24.88955	24.97037	25	25		20	20
1100	470	20	20	20	20	20	20.00808	20.02694	20.06735	20.17511	20.52532	21.33351	23.21929	24.70097	24.88955	24.97037	25	25		20	20
1100	470	20	20	20	20	20	20.00808	20.02694	20.06735	20.17511	20.52532	21.33351	23.21929	24.70097	24.88955	24.97037	25	25		20	20
1100	470	20	20	20	20	20	20.00808	20.02694	20.06735	20.17511	20.52532	21.33351	23.21929	24.70097	24.88955	24.97037	25	25		20	20
1100	470	20	20	20	20	20	20.00808	20.02694	20.06735	20.17511	20.52532	21.33351	23.21929	24.70097	24.88955	24.97037	25	25		20	20
							20									20					
Time = 10 s											T_water in the Closed Loop Thermosyhon Heat Pipe										
Mass flow rate = 2.58E-14 kg/s																					
							20									20					
T_Core	T_RPV	T_air	T_fin		T_air					Temperature Distribution in Concrete								T_env			T_Dam
1099.999	469.9822	469.9346	20.33122	20	20	20.01109	20.00808	20.02694	20.06735	20.17511	20.52533	21.33352	23.21929	24.70097	24.88955	24.97037	24.98891	25		20	20.00003
1099.999	469.9822	469.9346	20.33122	20	20	20.01109	20.00808	20.02694	20.06735	20.17511	20.52533	21.33352	23.21929	24.70097	24.88955	24.97037	24.98891	25		20	20.00003
1099.999	469.9822	469.9346	20.33122	20	20	20.01109	20.00808	20.02694	20.06735	20.17511	20.52533	21.33352	23.21929	24.70097	24.88955	24.97037	24.98891	25		20	20.00003
1099.999	469.9822	469.9346	20.33122	20	20	20.01109	20.00808	20.02694	20.06735	20.17511	20.52533	21.33352	23.21929	24.70097	24.88955	24.97037	24.98891	25		20	20.00003
1099.999	469.9822	469.9346	20.33122	20	20	20.01109	20.00808	20.02694	20.06735	20.17511	20.52533	21.33352	23.21929	24.70097	24.88955	24.97037	24.98891	25		20	20.00003
1099.999	469.9822	469.9346	20.33122	20	20	20.01109	20.00808	20.02694	20.06735	20.17511	20.52533	21.33352	23.21929	24.70097	24.88955	24.97037	24.98891	25		20	20.00003
1099.999	469.9822	469.9346	20.33122	20	20	20.01109	20.00808	20.02694	20.06735	20.17511	20.52533	21.33352	23.21929	24.70097	24.88955	24.97037	24.98891	25		20	20.00003
1099.999	469.9822	469.9346	20.33122	20	20	20.01109	20.00808	20.02694	20.06735	20.17511	20.52533	21.33352	23.21929	24.70097	24.88955	24.97037	24.98891	25		20	20.00003
							20									20					

Chapter 5

Experimental Work

The design of the experimental apparatus and the goals that need to be achieved with the different experiments are discussed in this section. The experiments was used to verify the theoretical model of the RCCS.

5.1 Goals of the experimental work

The main objective of the experimental work is to verify the theoretical model of the heat transfer from the core to the concrete citadel. This means that the modelling of the convection heat transfer coefficients for all the surfaces in the reactor cavity need to be modelled correctly and verified with an experiment. The radiation heat transfer must also be modelled and verified with the experiment.

The first goal of the experimental work is to build an experiment that represents the heat transfer in the reactor cavity as closely as possible. The second goal is to have only two controlled parameters. These would be a RPV temperature that can be kept constant and a water mass flow rate through the heat pipes that can also be kept constant.

The temperatures of the RPV, the heat shields and concrete are measured at three different height levels in order to establish whether or not there is a temperature distribution in the vertical direction in these components. This also implies that the experiment must be large enough so that a measurable temperature distribution is created. The RPV in the PBMR reactor will operate at 350 °C under normal operating conditions. The experiment must control the RPV temperature and keep it at 300 °C or 350 °C if possible. The theoretical model will be used to predict the mass flow rate of the cooling water in the heat pipe for whatever constant RPV temperature. The theoretical mass flow rate is not constant but it always converges to some sort of constant when thermal equilibrium is reached. The mass flow rate in the experiment will then be set to a value as close as possible to the theoretical value. The mass flow rate of the experiment will then be used in the theoretical model as a constant and the temperatures will be predicted for the heat shield and the concrete. The heat shield and concrete temperatures as well as the water inlet and outlet temperatures will be measured in the experiment. If the heat shield and concrete as well as the water temperatures of the experiment are the same as in the theoretical model, it will be assumed that all the heat transfer coefficients are correct.

5.2 Design of the experimental apparatus

It was decided that the experiment should geometrically represent the RPV, the RCCS and the concrete structure of the PBMR. All materials that were to be used should be the same as those to be used in the PBMR reactor. The RPV would be represented by heating plates constructed of mild steel with electric heating elements fitted to the back of them, the fins and heat pipes by stainless steel to form the heat shield and the concrete would be Ready Mixed concrete. In order to optimise the heat shield configuration, differently sized fins must be considered, thus the experiment must be able to test differently sized fin-and-pipe configurations. The heat shields needed to work independently from each other so that the heat shields could be tested one at a time. It was decided to test three different sized heat shields constructed of three different sized pipes and flatbar. Table 5.1 shows the dimensions of the stainless steel pipes and flatbar that were used to construct the heat pipes and fins. The pipes and flatbar are 304 stainless steel.

Table 5.1: Heat pipe and fin dimensions used in the experiments

Heat Pipe Name	OD (mm)	ID (mm)	Fins (Flatbar) (mm)
Small	42.16	35.04	50 x 6
Medium	73.03	62.71	75 x 6
Large	114.3	102.26	100 x 10

Figure 5.1 shows how the experiment was assembled. The heat pipes are 2 m long and are all connected to the same water inlet and outlet. Cooling water is pumped from a storage tank into the heat pipes from the bottom. As can be seen in figure 5.1(b), there are three separately cast concrete slabs which represent the concrete citadel. These concrete slabs are secured to the frame with four flatbar steel straps. Figures 5.1(c) and 5.1(d) shows the insulation. The insulation is 20 mm sheet of calcium silicate ($k = 0.06$ W/mK) covered with a 0.5 mm stainless steel sheet on each side. The insulation forms an enclosed rectangle around the heating plates and the concrete. The heating elements for each of the three heat pipes can be switched on independently and the water can be channelled to each heat pipe with ball valves. The mass flow rate of the water is controlled on the outlet side with two gate valves.

The thermocouples were placed in such a way that they would measure the intended temperatures as closely as possible to the true temperatures of the RPV, the HS and the concrete. This implies good contact of the thermocouple junctions with the surfaces of the components. The heating plate temperatures are measured with iron-constantan J-type thermocouples that are bolted to the heating plates to ensure good contact. The surface temperature of the fins on the heat pipes needs to be measure on both sides. The copper-constantan T-type thermocouples used for this were placed against the fin and the tips of the thermocouples were glued to the fin. The thermocouples were then covered with white silicon. The silicon acts as insulation. This ensured that an accurate measurement of the fin surface is achieved. The concrete temperatures must be measured just beneath the surface. T-type thermocouples were made and cast into the concrete with their junctions about 2 mm beneath the surface.

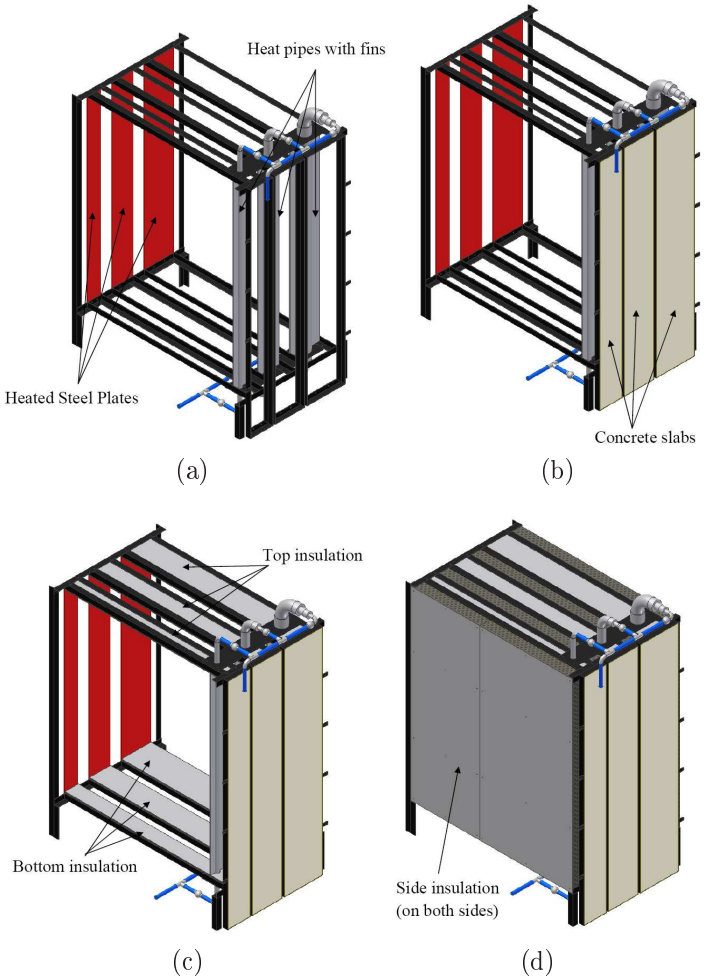

Figure 5.1: Experiment Assembly: (a) shows the heat pipes and heating plates; (b) shows the concrete; (c) shows the top and bottom insulation; and, (d) shows the side insulation walls.

5.3 Experimental procedure and data handling

Two experiments were done for each of the three heat pipes. The first was a 'wet' experiment where water is pumped through the heat pipe and the second is a 'dry' experiment where there is no water in the heat pipe and the heat pipe is used purely as a radiation shield. The reason for having the two experiments is to be able to get an idea of the effectiveness of the cooling. The 'dry' experiment will give the maximum concrete temperatures and the 'wet' experiment will then be used to see by how much the concrete temperature can be lowered, giving an idea of how effective the reactor cavity cooling is.

The experimental procedure starts off with by setting the cooling water mass flow rate to the predetermined value as explained in Section 5.1. This is done by adjusting the valves shown in figure 5.2. One valve is connected to the outlet of the heat pipe and the other is connected to a by-pass pipe. By closing the by-pass valve and opening the outlet valve, the mass flow rate is increased and visa-versa. The reason for having a by-pass pipe is to allow the mass flow rate through the pump to remain constant. The cooling water mass flow rate is measured at the outlet by filling a bucket of known volume within a measured time and weighing the water in the bucket using an electronic scale. After

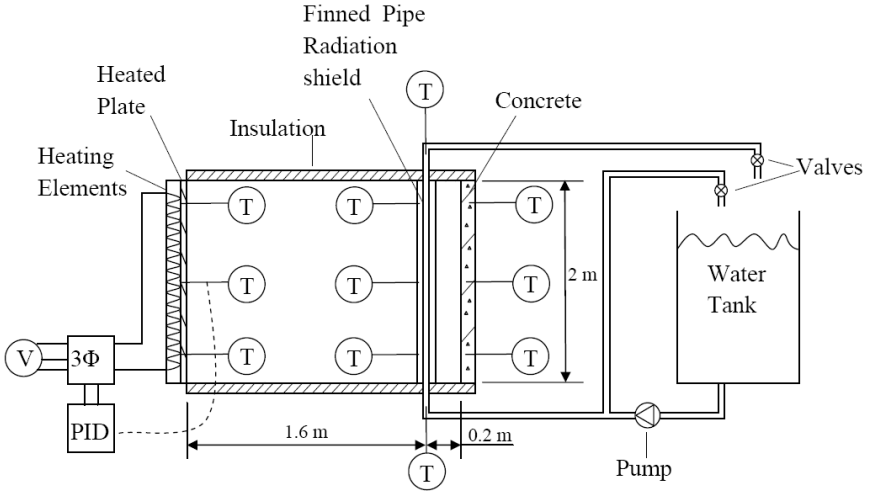

Figure 5.2: Cross section of the experimental set-up (heat pipe rotated 90° for illustrative purposes only)

the mass flow rate is set, the data logger is turned on and then the heating elements are turned on. The experiment is run for 7 hours and the temperatures are logged every 10 seconds by the data logger. It was decided to run the experiment for 7 hours because the concrete is by then very close to thermal equilibrium. Figure 5.2 shows where the temperatures are measured during the experiment as well as the general layout of the experimental set-up.

In order to compare the experimental data to the theoretical data, the theoretical model needed to be adjusted so that it simulated the experiment and not the reactor geometry. Firstly, the RPV temperature was fixed in the theoretical model. Secondly, the cooling water mass flow rate was given as a function of time as measured in the experiment. This was needed because the mass flow rate drops slightly during the 7 hour experiment. The fin efficiency and the heat transfer coefficients were adjusted to predict the experimental values more accurately. After this, the heat losses from the experiment were approximated by using the loss factors as explained in Section 2.11. The loss factor will have a value ranging from zero to one and is used to approximate the convection heat losses from the enclosed air cavity, through the insulation and the small openings in the experimental apparatus, to the surroundings. This adjusted theoretical model was then used for analysing the 'dry' experiment results.

The data handling of the small heat pipe experiment has been used as an example to show how the theoretical model was changed in order to predict the experimental data. The fin efficiency was determined first. This was done by comparing the inlet and outlet water temperatures for the experiment and the theoretical model. It was found that the theoretical model used a convective heat transfer coefficient on the inside of the heat pipe that was too large. The result of this was that the outlet water temperature was predicted too high as shown by figure 5.3 and that the heat shield temperature was predicted too low. The reason for the high heat transfer coefficient is that the onset of turbulent flow was specified as by Dobson and Ruppersberg (2006) at $Re_{turb} = 1181$. It was decided to use $Re_{turb} = 2300$ as specified by Çengel (2003). The result was a lower heat transfer coefficient and more accurate results as can be seen in figure 5.4.

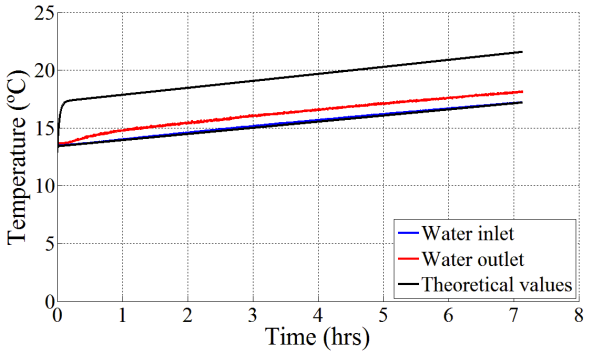

Figure 5.3: Inlet and outlet water temperatures if $Re_{turb} = 1181$

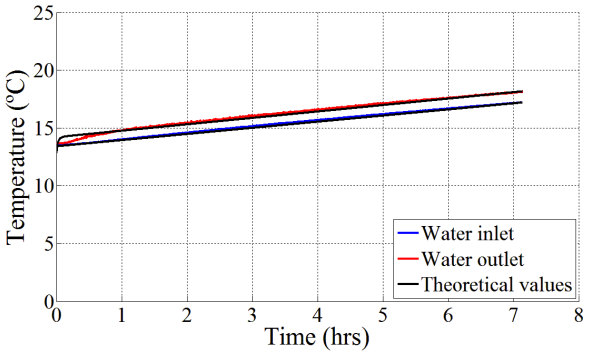

Figure 5.4: Inlet and outlet water temperatures if $Re_{turb} = 2300$

The heat transferred to the cooling water is affected by two factors, namely the inside heat transfer coefficient and the fin efficiency. Changes in the inside heat transfer coefficient had a significant effect on the water outlet temperature as seen in figures 5.3 and 5.4, where the outlet water temperature is reduced from 22 °C to 18 °C by using $Re_{turb} = 2300$. Changes in the fin efficiency, however, do not have such a big effect on the outlet water temperature but it has a significant effect on the heat shield temperature. Changes in the heat transfer coefficient do not have a significant effect on the heat shield temperature. These observations were used to approximate the fin efficiency based on the measured heat shield temperatures. The fin efficiency was adjusted until the theoretical heat shield temperatures were close to the experimental values. This was done for both the 'wet' and 'dry' experiments. The fin efficiency is not the only factor affecting the heat shield temperature. The convection heat transfer from the air to the heat shield has a major effect as well. It was found that the fin efficiency had to be dropped to 0.1 for the heat shield temperature to be as high as the experimental values. The effect of this was that the cooling water outlet temperature was predicted too low. The convection was clearly predicted too low. The correlations given in Section 3.1.2 assumes a geometry with infinite depth as well as an open top. It was decided that a correlation that was derived from a similar experiment needed to be used. Costa (2002) did a similar experiment and also used a 1D theoretical model as well as a CFD model. Costa (2002) used only one Nusselt number (or heat transfer coefficient) to describe the heat transfer in an enclosure of height H and length L from a vertical heated wall to a vertical cold wall opposing it instead of two convection heat transfer coefficients as used by Dobson and Ruppersberg (2006). This Nusselt number is given by

$$Nu = 0.18 \left(\frac{Pr}{0.2 + Pr} Ra \right)^{0.29} \left(\frac{L}{H} \right)^{-0.13} \tag{5.3.1}$$

This correlation is for laminar convection in an enclosure of infinite depth, but it was found that when using a Nu multiplication factor of 3 for turbulent convection in a finite enclosure, it produced heat transfer rates that corresponded with the experimental results. The heat shield temperatures for the 'wet' and 'dry' experiments can be seen in figures 5.5 and 5.6.

To account for the heat losses and the fact that appropriate heat transfer coefficients are not available for the specific geometry of the experiment it was necessary to multiply the heat transfer from the RPV to the radiation shield in the experiment with heat loss

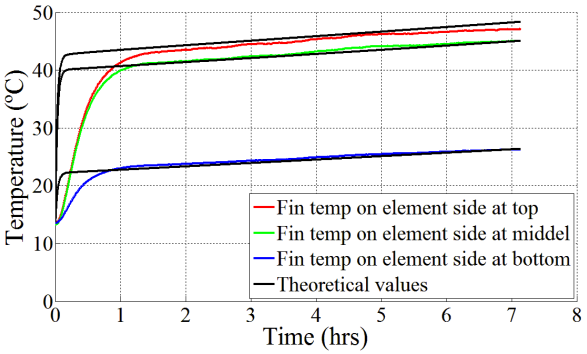

Figure 5.5: Heat shield temperatures for the small heat pipe under wet conditions at different height levels of the experiment

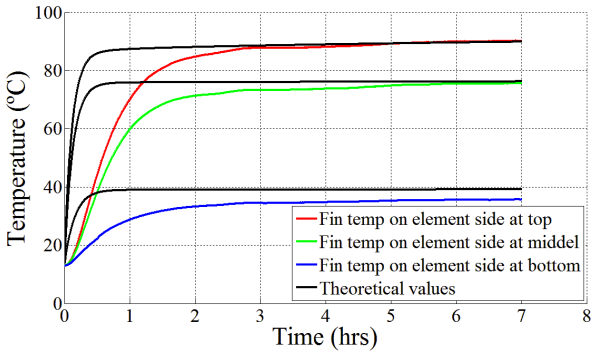

Figure 5.6: Heat shield temperatures for the small heat pipe under dry conditions at different height levels of the experiment

factors. The heat loss from the back of the elements to the environment was ignored because only the temperature of the RPV important. Other heat losses included the thermal capacity of the support structures and the environment. This is not an actual loss of heat, but the thermal capacity of the support structures and the environment has an influence on the temperature time response. The small openings between the insulation walls and the structure also led to some losses especially at the bottom of the structure. The heat transfer model was adjusted so that for the 'wet' condition, the loss factors would be zero except at the bottom where the heat losses were substantial. For the 'dry' experiments, all the temperatures are higher and the losses are more. This was physically observed during the experiments. The losses for the 'wet' experiment from the elements to the heat shield was estimated to be 22 % and for the 'dry' experiment around 47 %. This last value may seem high, but this is when the Nusselt number is multiplied by 3 to model turbulent convection. At higher temperatures the factor of 3 may be too big.

The convection between the heat shield and the concrete is modelled by using the correlations as used by Mills (1999) as discussed in Section 2.11. The Nusselt number was again multiplied by 3 for both the 'wet' and 'dry' experiments with all the loss factors from the heat shield to the concrete equal to zero for the 'wet' experiment and 40 % for the 'dry' experiment. The results are shown in figures 5.7 and 5.8.

This data handling and adjustment of the theoretical model was repeated for the medium and large heat pipe experiments. The results are shown in Section 5.4.

5.4 Experimental results

The theoretical values for the medium and large heat pipe experiments were obtained using the same theoretical model that was adjusted by, and used for the small heat pipe experiment. The only variables that were adjusted were the loss factors for the convection between the heating elements and the heat shield and between the heat shield and the concrete.

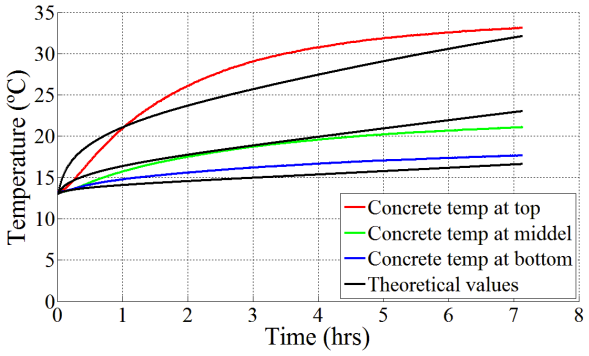

Figure 5.7: Concrete temperatures for the small heat pipe under wet conditions at different height levels of the experiment

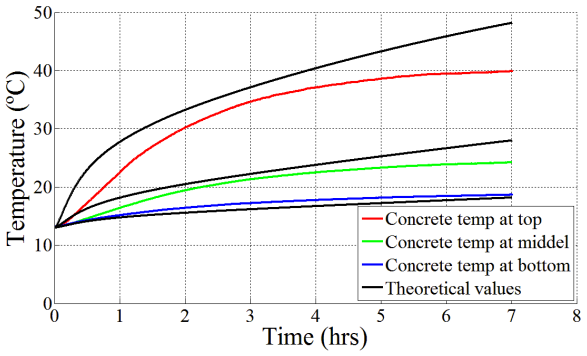

Figure 5.8: Concrete temperatures for the small heat pipe under dry conditions at different height levels of the experiment

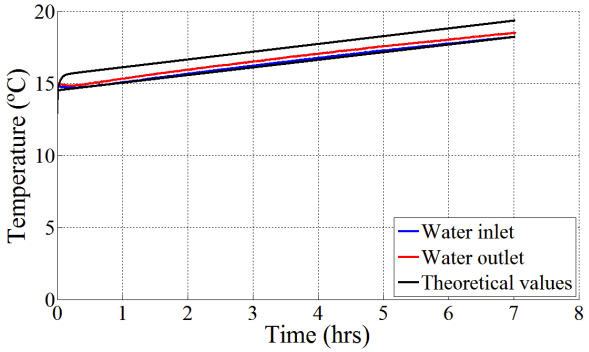

Figure 5.9: Inlet and outlet water temperatures for the medium heat pipe under wet conditions

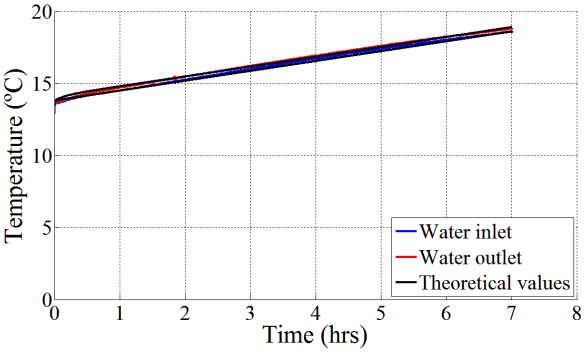

Figure 5.10: Inlet and outlet water temperatures for the large heat pipe under wet conditions

As can be seen in figures 5.9 and 5.10, the outlet temperature of the cooling water is predicted accurately by using the theoretical fin efficiencies shown in Table 5.2 and a turbulent Reynolds value $Re_{turb} = 2300$.

Figures 5.11 and 5.12 show the heat shield temperatures for the medium and large heat pipe experiments under 'wet' conditions. By using the fin efficiencies, loss factors and Nu multiplication factors given in Table 5.2, the heat shield temperatures can be well predicted and one can develop a good feel for the heat losses in the experiment. Figures 5.13 and 5.14 show the heat shield temperatures for the medium and large heat pipe experiments under 'wet' conditions. As can be seen from the figures, the temperatures for the concrete gets over predicted, for instance at 7 hours into the experiment the predicted value of the concrete is 31.75 °C, which is 4.7 % higher than the experimental value of 30.25 °C.

Table 5.2 shows the theoretical fin efficiencies used in the modelling of the experiments. The theoretical fin efficiency is defined as the ratio of the actual heat transfer rate from the fin to the ideal heat transfer rate from the fin if the entire fin were at the base temperature of the fin. It also gives the heat loss factors between the elements and the heat shield (or

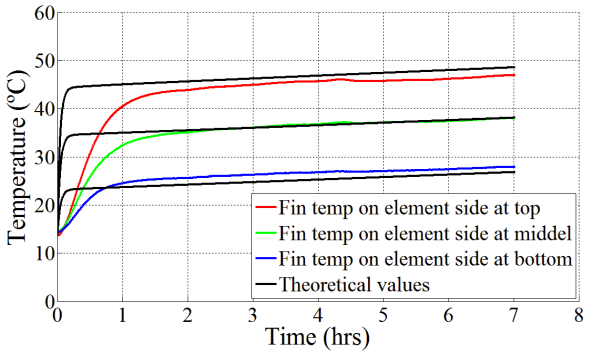

Figure 5.11: Heat shield temperatures for the medium heat pipe under wet conditions at different height levels of the experiment

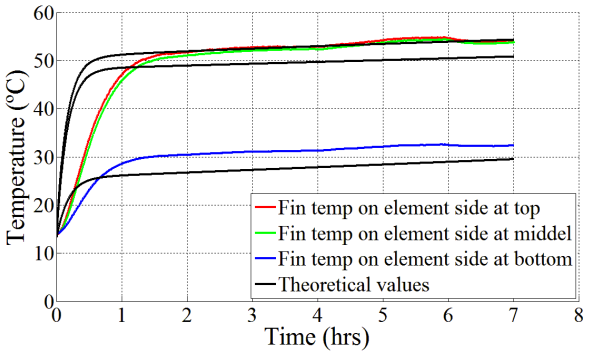

Figure 5.12: Heat shield temperatures for the large heat pipe under wet conditions at different height levels of the experiment

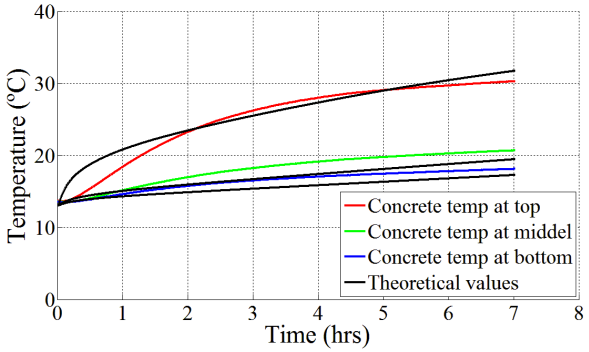

Figure 5.13: Concrete temperatures for the medium heat pipe under wet conditions at different height levels of the experiment

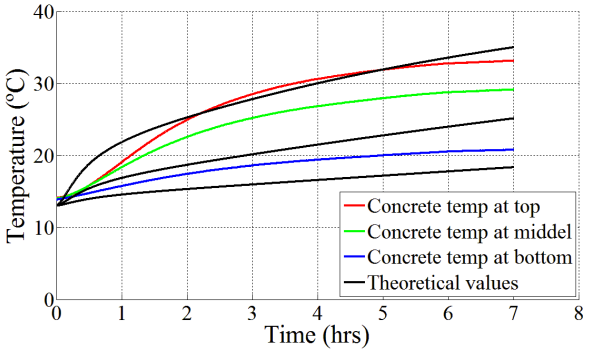

Figure 5.14: Concrete temperatures for the large heat pipe under wet conditions at different height levels of the experiment

Table 5.2: Theoretical fin efficiencies, loss factors (LF) and Nu multiplication factors

Heat Pipe	η	Loss factors		Nu multiplication factor	
		LF_{ef}	LF_{fc}	Nu_{ef}	Nu_{fc}
Small	0.7	0.22	0.0	3	3
Medium	0.4	0.27	0.175	2.8	3
Large	0.15	0.23	0.175	1	3

fin), LF_{ef}, the heat loss factors between the heat shield and the concrete, LF_{fc}, as well as the Nu multiplication factor used between the elements and the heat shield, Nu_{ef} and between the heat shield and the concrete, Nu_{fc}. The Nu multiplication factors are needed because both Costa (2002) and Mills (1999) assumes an infinite depth of the enclosure in which the convection takes place. As can be seen from Table 5.2, Nu_{ef} decreases as the depth of the enclosure increases. For this reason, Nu_{ef} will be set to one in the model of the reactor cavity. Nu_{fc} will be set to 3 in the model of the reactor cavity to increase the convection heat transfer between the radiation shield and the concrete. All loss factors will be zero because there will be no losses to the environment in the actual reactor cavity.

The cooling effect of the cooling water on the heat shield and concrete temperatures can be seen in Table 5.3. The cooling water in the small heat pipe has the biggest effect on the heat shield and concrete temperatures. The cooling water lowers the heat shield temperature by 43.1 °C and the concrete temperature by 6.9 °C.

Table 5.3: Effect of the cooling water in the 'wet' experiments

Heat Pipe	Wet		Dry		$\Delta T_{heatshield}$	ΔT_{cs}
	$T_{heatshield}$	T_{cs}	$T_{heatshield}$	T_{cs}		
Small	47.1	33.1	90.2	40.0	43.1	6.9
Medium	46.9	30.3	80.0	35.3	33.1	5.0
Large	54.8	33.1	94.4	38.9	39.6	5.8

Chapter 6

Sensitivity Analysis

In this chapter, the sensitivity of the theoretical model is investigated. It is necessary to investigate in what way changes in the material properties affect the results of the theoretical model. Each material property must be tested through a range of values. It is also necessary to investigate the effect of changing the Nusselt numbers as was done in Section 5.3. Changes in the ambient conditions are also tested with the theoretical model.

6.1 An investigation of the effect of changes in the material properties of the RPV, the heat shield and the concrete structure on the temperatures calculated by the theoretical model

Table 6.1: Material properties as used in the experiments

Component	C_p (J/kgK)	ε	ρ (kg/m^3)	k (W/m°C)
RPV	500*	0.85	7800*	∞
Heat Shield	477	0.8	7900	16
Concrete	1100	0.77	2400	0.8

The material properties for the RPV, the heat shield and the concrete structure as was used in the experiments can be seen in Table 6.1. The RPV properties marked with *s have no influence on the result of the model for the experiments. This is because in the RPV temperature is kept constant in the model for the experiment. The other properties were approximated by trial and error beginning with values found in literature. The properties given in Table 6.1 will be the starting point of the sensitivity analysis. The theoretical model will also have $Re_{turb} = 2300$ for the water in the heat pipes as discussed in Section 5.3. The thermal conductivity of the RPV was chosen $k = \infty$ to simplify the theoretical model. This implies that the RPV has no temperature drop over its thickness. This is a conservative approximation, because there will be a small temperature drop over the RPV in reality.

In the sensitivity analysis all the properties as given in Table 6.1 were kept constant except the one under investigation. After one property's sensitivity analysis is done, the value will be set to the value given in Table 6.1 and the sensitivity analysis of the next

property can begin. All the sensitivity analyses simulations were done for a simulation time of 10^6 s. For the sensitivity analysis, CLTHPs with 32.46 mm ID pipes with 45 mm wide fins were used with a 30 m diameter cooling dam. The temperatures that were calculated by the theoretical model and shown in Tables 6.3 to 6.5 are listed in Table 6.2.

Table 6.2: List of calculated temperatures in the sensitivity analysis

T_{core}	Temperature of the reactor core
T_{RPV}	Temperature of the RPV
$T_{A_{RPV-HS_i}}$	Temperature of the air between the RPV and the heat shield (HS)
T_{HS_i}	Temperature of the heat shield (HS) on the inside surface
T_{HS_o}	Temperature of the heat shield (HS) on the outside surface
T_w	Temperature of the water in the heat pipes
$T_{A_{HS_o-Con_i}}$	Temperature of the air between the heat shield (HS) and the concrete
T_{Con_i}	Temperature of the concrete structure on the inside surface
T_{Con_o}	Temperature of the concrete structure on the outside surface

Table 6.3 shows the temperatures calculated by the theoretical model for changes in the RPV material properties. As can be seen, changes in the thermal capacity and density have little to no affect on the calculated temperatures. Changes in the emissivity, however, have a greater effect on the RPV temperature. By changing the emissivity from 0.6 to 0.9, the RPV temperature drops by approximately 48 °C. Even though there is a drop in temperature of the RPV, the heat shield temperature increases slightly. This is due to the fact that more heat is transferred by radiation from the RPV to the heat shield when its emissivity is increased.

Table 6.4 shows the temperatures calculated by the theoretical model for changes in the heat shield material properties. Again, changes in the thermal capacity and density have little to no effect on the calculated temperatures. Changes in the thermal conductivity also do not effect the calculated temperatures by much. The emissivity is once again the property with the biggest influence on the results. By changing the emissivity from 0.3 to 0.9, the RPV temperature drops by approximately 111 °C. The heat shield temperature increases slightly (0.07 %) as was seen before in Table 6.3. The emissivity of the heat shield is the first change in material property that has a significant effect on the surface temperature of the concrete structure. By changing the emissivity of the heat shield from 0.3 to 0.9, the surface temperature of the concrete structure is increased by almost 7 °C. It is thus desirable to have a heat shield with a very low emissivity.

Table 6.5 shows the temperatures calculated by the theoretical model for changes in the concrete structure material properties. The sensitivity of the surface temperature of the concrete structure varies for all of the concrete structure material properties. When varying the thermal capacity from 700 J/kgK to 1300 J/kgK, the concrete structure temperature decreases by 1.67 °C. If the emissivity of the concrete structure is changed from 0.3 to 0.9, the concrete structure temperature increases by 6.4 °C. A density change from 1900 kg/m^3 to 2500 kg/m^3 makes the concrete structure temperature decrease by 0.8 °C. An increase in the thermal conductivity of the concrete structure from 0.6 W/m°C to 1.8 W/m°C results in a decrease in the concrete structure temperature of 5.3 °C. This is important as the specified maximum allowed temperature of the concrete structure is

Table 6.3: Sensitivity analysis for RPV material properties

	T_{core}	T_{RPV}	$T_{A_{RPV-HS_i}}$	T_{HS_i}	T_{HS_o}	T_w	$T_{A_{HS_o-Con_i}}$	T_{Con_i}	T_{Con_o}
C_p									
300	1035.485	369.433	204.925	80.310	80.123	70.667	76.157	72.118	28.188
350	1035.485	369.432	204.927	80.315	80.128	70.673	76.163	72.125	28.192
400	1035.484	369.43	204.929	80.320	80.133	70.678	76.169	72.132	28.196
450	1035.484	369.429	204.931	80.324	80.138	70.684	76.175	72.139	28.200
500	1035.483	369.428	204.934	80.329	80.143	70.690	76.181	72.146	28.204
550	1035.482	369.427	204.936	80.334	80.147	70.695	76.187	72.153	28.209
600	1035.482	369.426	204.938	80.339	80.152	70.701	76.192	72.160	28.213
ε									
0.6	1058.465	411.144	222.885	80.280	80.093	70.632	76.120	72.074	28.164
0.65	1052.925	401.176	218.596	80.291	80.104	70.645	76.134	72.091	28.173
0.7	1047.933	392.148	214.710	80.302	80.115	70.657	76.147	72.106	28.182
0.75	1043.405	383.918	211.168	80.311	80.124	70.668	76.158	72.119	28.189
0.8	1039.273	376.376	207.922	80.319	80.133	70.678	76.168	72.132	28.196
0.85	1035.483	369.429	204.932	80.327	80.140	70.687	76.178	72.143	28.203
0.9	1031.991	363.003	202.167	80.334	80.148	70.695	76.187	72.153	28.208
ρ									
7500	1035.483	369.429	204.932	80.325	80.139	70.685	76.176	72.140	28.201
7600	1035.483	369.429	204.932	80.326	80.139	70.686	76.176	72.141	28.202
7700	1035.483	369.429	204.932	80.326	80.140	70.686	76.177	72.142	28.202
7800	1035.483	369.429	204.932	80.327	80.140	70.687	76.178	72.143	28.203
7900	1035.483	369.429	204.933	80.328	80.141	70.688	76.179	72.144	28.203
8000	1035.483	369.429	204.933	80.328	80.142	70.689	76.179	72.145	28.204
8100	1035.483	369.428	204.933	80.329	80.142	70.689	76.180	72.145	28.204

only 65 °C.

In order to establish which material property of the concrete structure has the biggest effect on the surface temperature of the concrete structure, it is necessary to compare the percentage change in the concrete structure temperature corresponding to a percentage change in each material property. The result of this is shown in Table 6.6. As can be seen, the changes in the concrete structure emissivity has the biggest effect on the concrete structure temperature.

The heat transfer from the back of the heat shield to the concrete structure was modelled for the experiments using the equations given in Section 2.11 as given by Mills (1999), but the Nusselt number was multiplied by 3 to account for the specific geometry and heat loss situation as discussed in Section 5.3. The same calculations were then used for the theoretical model as well as the method of Dobson and Ruppersberg (2006) as given in Section 2.11. The results can be seen in Table 6.7.

As shown in Tables 6.5 and 6.4, the emissivities of the heat shield and the concrete structure has the greatest effect on the surface temperature of the concrete structure. The emissivity of stainless steel changes with time because of oxidation and the deposition of fission products. For new stainless steel surfaces an emissivity of 0.3 is normally assumed.

Table 6.4: Sensitivity analysis for heat shield material properties

	T_{core}	T_{RPV}	$T_{A_{RPV-HS_i}}$	T_{HS_i}	T_{HS_o}	T_w	$T_{A_{HS_o-Con_i}}$	T_{Con_i}	T_{Con_o}
C_p									
440	1035.484	369.430	204.934	80.330	80.143	70.690	76.181	72.147	28.204
460	1035.483	369.429	204.933	80.328	80.142	70.688	76.179	72.145	28.203
480	1035.483	369.429	204.932	80.327	80.140	70.687	76.178	72.143	28.202
500	1035.483	369.428	204.931	80.325	80.139	70.685	76.176	72.141	28.201
520	1035.483	369.428	204.930	80.324	80.137	70.684	76.174	72.139	28.201
540	1035.482	369.428	204.929	80.323	80.136	70.683	76.172	72.136	28.200
560	1035.482	369.427	204.929	80.321	80.134	70.681	76.171	72.134	28.199
ε									
0.3	1092.510	471.249	248.770	80.242	80.070	70.579	73.056	66.068	27.123
0.4	1073.130	437.271	234.142	80.272	80.094	70.617	74.058	68.015	27.459
0.5	1059.627	413.228	223.790	80.292	80.111	70.642	74.800	69.459	27.713
0.6	1049.579	395.129	215.998	80.307	80.123	70.661	75.369	70.566	27.912
0.7	1041.762	380.923	209.881	80.318	80.133	70.676	75.817	71.439	28.072
0.8	1035.483	369.429	204.932	80.327	80.140	70.687	76.178	72.143	28.203
0.9	1030.315	359.912	200.835	80.335	80.147	70.697	76.475	72.721	28.311
ρ									
7600	1035.483	369.429	204.933	80.328	80.142	70.688	76.179	72.145	28.203
7700	1035.483	369.429	204.933	80.328	80.141	70.688	76.179	72.144	28.203
7800	1035.483	369.429	204.933	80.327	80.141	70.688	76.178	72.143	28.203
7900	1035.483	369.429	204.932	80.327	80.140	70.687	76.178	72.143	28.203
8000	1035.483	369.429	204.932	80.327	80.140	70.687	76.177	72.142	28.202
8100	1035.483	369.429	204.932	80.326	80.140	70.686	76.177	72.142	28.202
8200	1035.483	369.428	204.932	80.326	80.139	70.686	76.176	72.141	28.202
k									
14	1035.483	369.429	204.933	80.327	80.114	70.687	76.165	72.117	28.198
15	1035.483	369.429	204.933	80.327	80.128	70.687	76.172	72.131	28.200
16	1035.483	369.429	204.932	80.327	80.140	70.687	76.178	72.143	28.203
17	1035.483	369.429	204.932	80.327	80.151	70.687	76.183	72.153	28.205
18	1035.483	369.429	204.932	80.327	80.161	70.687	76.188	72.163	28.206
19	1035.483	369.429	204.932	80.327	80.170	70.687	76.192	72.171	28.208
20	1035.483	369.429	204.932	80.327	80.178	70.687	76.196	72.179	28.209

This could not be used because the emissivity will change with time. Incropera and DeWitt (2002) suggests emissivities of 0.33 for lightly oxidized stainless steel, 0.67 for highly oxidized stainless steel and 0.88 for oxide surface treated stainless steel.

de Groot *et al.* (2008) suggests that inspection of previous high temperature experiments has indicated that stainless steel tube surfaces, as used in the heat shield, are severely coloured by oxidation and the deposition of fission products. This result in a reduced reflectivity and a more carbon-like surface state of the stainless steel surface and it would lead to an increased emissivity. An increased emissivity reduces the temperature difference between the RPV and the heat shield and between the heat shield and the concrete structure surface. Therefore, an emissivity of 0.8 was conservatively adopted for the stainless steel. (de Groot *et al.*, 2008)

Table 6.5: Sensitivity analysis for concrete structure material properties

	T_{core}	T_{RPV}	$T_{A_{RPV-HS_i}}$	T_{HS_i}	T_{HS_o}	T_w	$T_{A_{HS_o-Con_i}}$	T_{Con_i}	T_{Con_o}
C_p									
700	1035.490	369.441	204.965	80.374	80.213	70.727	76.782	73.288	29.997
800	1035.488	369.438	204.956	80.362	80.194	70.717	76.626	72.994	29.554
900	1035.487	369.435	204.948	80.350	80.175	70.706	76.473	72.702	29.097
1000	1035.485	369.432	204.940	80.338	80.158	70.697	76.323	72.418	28.643
1100	1035.483	369.429	204.932	80.327	80.140	70.687	76.178	72.143	28.203
1200	1035.482	369.426	204.925	80.316	80.124	70.678	76.038	71.878	27.781
1300	1035.480	369.423	204.918	80.306	80.108	70.669	75.904	71.623	27.380
ε									
0.3	1035.488	369.437	204.954	80.359	80.186	70.716	73.337	66.508	27.256
0.4	1035.487	369.434	204.947	80.348	80.171	70.706	74.280	68.380	27.561
0.5	1035.485	369.432	204.941	80.340	80.159	70.699	74.979	69.765	27.792
0.6	1035.484	369.431	204.937	80.334	80.151	70.694	75.513	70.824	27.973
0.7	1035.484	369.430	204.934	80.330	80.144	70.690	75.934	71.658	28.117
0.8	1035.483	369.429	204.932	80.326	80.139	70.686	76.272	72.330	28.236
0.9	1035.483	369.428	204.930	80.323	80.135	70.683	76.551	72.882	28.334
ρ									
1900	1035.487	369.436	204.950	80.353	80.181	70.709	76.517	72.787	29.231
2000	1035.486	369.434	204.947	80.348	80.172	70.705	76.447	72.654	29.021
2100	1035.486	369.433	204.943	80.343	80.164	70.700	76.378	72.523	28.812
2200	1035.485	369.431	204.939	80.337	80.156	70.696	76.310	72.394	28.606
2300	1035.484	369.430	204.936	80.332	80.148	70.691	76.244	72.268	28.402
2400	1035.483	369.429	204.932	80.327	80.140	70.687	76.178	72.143	28.203
2500	1035.482	369.428	204.929	80.322	80.133	70.683	76.113	72.020	28.007
k									
0.6	1035.490	369.441	204.964	80.373	80.212	70.725	76.810	73.344	26.063
0.8	1035.483	369.429	204.932	80.327	80.140	70.687	76.178	72.143	28.203
1	1035.478	369.419	204.906	80.288	80.079	70.655	75.638	71.116	30.006
1.2	1035.473	369.410	204.883	80.254	80.025	70.627	75.166	70.218	31.546
1.4	1035.468	369.402	204.862	80.224	79.978	70.603	74.747	69.421	32.874
1.6	1035.465	369.395	204.844	80.197	79.935	70.581	74.370	68.704	34.032
1.8	1035.461	369.389	204.827	80.173	79.897	70.561	74.028	68.053	35.050

The results of this sensitivity analysis are that the transition from laminar to turbulent flow in the heat pipes will be at $Re_{turb} = 2300$ and the convection heat transfer should be calculated as was done by Dobson and Ruppersberg (2006) because Dobson and Ruppersberg (2006) uses a simpler, yet sufficiently accurate correlation than Mills (1999). Furthermore, the emissivity of stainless steel will be 0.8 although it can be lower and the concrete structure emissivity will be 0.77 as used in the experiments as this is what is expected in the very long term.

Table 6.6: Comparison of the sensitivity of the concrete structure temperature for different Material Properties (MPs)

MP	Increase in MP (%)	ΔT_{Con_i} (%)	ΔT_{Con_i} per 100 % increase in MP
C_p	86	-2.3	-2.7
ε	200	9.6	4.8
ρ	32	-1	-3.1
k	200	-7.2	-3.6

Table 6.7: Comparison of the sensitivity of the concrete structure temperature for different Nu correlations

	T_{core}	T_{RPV}	$T_{A_{RPV-HS_i}}$	T_{HS_i}	T_{HS_o}	T_w	$T_{A_{HS_o-Con_i}}$	T_{Con_i}	T_{Con_o}
Nu_M	1035.48	369.42	204.93	80.33	80.14	70.69	71.3	71.3	28.02
Nu_{DR}	1035.48	369.42	204.93	80.32	80.14	70.68	76.17	72.14	28.2

6.2 The effect of changes in the ambient conditions on the temperatures calculated by the theoretical model

The ambient temperature, the relative humidity and the wind speed has an effect on the RCCS performance. In this sensitivity analysis, the ambient conditions are changed and a 6 day simulation was done with the theoretical model. The model used 32.46 mm ID closed loop thermosyphon heat pipes with 40 mm wide fins and a 30 m diameter cooling dam. The results of this sensitivity analysis are shown in Table 6.8.

Table 6.8: Sensitivity analysis for changes in the ambient conditions

	T_{Con_i}	T_{Con_o}	T_{dam} at top	T_{dam} at bottom	$\dot{m}_{evap}$
Relative Humidity					
0.3	68.02	23.71	52.79	36.43	0.00954
0.5	68.30	23.72	53.23	36.89	0.00938
0.7	68.57	23.73	53.67	37.34	0.00923
0.9	68.84	23.74	54.10	37.79	0.00908
T_{env}					
25	68.56	27.94	53.42	37.11	0.00876
30	69.31	31.83	53.81	37.54	0.00839
35	70.15	35.56	54.34	38.12	0.00795
40	71.10	39.24	55.04	38.86	0.00741
V_{wind}					
1	68.30	23.72	53.23	36.89	0.00938
20	64.42	23.63	45.83	31.82	0.02400
40	61.95	23.55	41.10	28.27	0.03245
60	60.21	23.49	37.76	25.66	0.03784

As can be seen from Table 6.8, the relative humidity of the ambient air does not have a

big effect on the temperature of the concrete structure. The concrete structure temperature increases with less than 1 °C as the RH is increased from 0.3 to 0.9. The cooling dam temperature increases with 1.3 °C and the rate of evaporation decreases slightly. Changes in the ambient temperature have a slightly bigger effect on the performance of the RCCS. The inside surface temperature of the concrete structure increases by approximately 2.5 °C as the ambient temperature changed from 25 °C to 40 °C. It must be noted that the day and night temperatures were set to 40 °C for the sensitivity analysis. The 2.5 °C increase is thus an over prediction of the concrete structure temperature on a 40 °C day. The wind speed has the biggest influence on the RCCS performance. The temperature of the concrete structure decreases with approximately 8 °C when the wind speed increases to 60 km/h. The wind enhances the cooling ability of the RCCS, but the rate of evaporation from the cooling dam increases by a factor of four. After this sensitivity analysis, it was decided to use a RH of 0.5 and an ambient air temperature of 25 °C in the day and 16 °C at night. Since the wind velocity has such a big effect on the performance of the RCCS, a 1 km/s wind will be used in the optimisation of the RCCS to keep with a conservative approach.

Chapter 7

Optimisation of the RCCS Radiation Heat Shield

The optimisation of the RCCS radiation heat shield is discussed in this chapter. The optimisation goal is discussed as well as the constraints on the RCCS design. The goal is to optimise the total mass of the RCCS. The optimisation is not done by minimizing a function that contains all the design variables as is the norm in numerical optimisation. The optimisation is done using the theoretical model as an optimisation tool and using different input values for the sizes of the heat pipes and fins to find a close-to-optimal design. The optimisation must satisfy the design specifications for 3 operating conditions, as listed in Section 1.2, making a single numerical optimisation even more complex.

7.1 Goals of the RCCS Radiation Heat Shield optimisation

The main goal of the RCCS radiation heat shield optimisation is to create a RCCS that will keep the inside surface temperature of the concrete citadel below 65 °C under normal operating conditions with the minimum amount of material required. The second goal of the optimisation is to find the combination of standard sized fins and pipes that will provide sufficient cooling under emergency conditions, but does not result in an excessive parasitic heat loss from the reactor cavity under normal operating conditions.

7.2 Design variables of the RCCS

There are a number of design variables that can be changed in order to improve the design of the RCCS. These include the diameter of the heat shield, the diameter of the pipes for the closed loop thermosyphon heat pipes and the fin widths and thicknesses of the radiation heat shield. The size of the cooling dam in which the downcomers stand will also have an effect on the performance of the RCCS.

7.3 General design constraints of the RCCS

As stated in Section 2.7, the RCCS must fit into the 1.52 m gap between the RPV and the concrete citadel. In the design of Barnert and Singh (1996), the radiation heat shield is very close to the RPV, but can then be moved in order for the RPV to be inspected.

The heat shield is closer to the concrete structure and will have a fixed position in the design for the purpose of this thesis. The reason for this is that inspection of the RPV would be possible without moving the RCCS. A fixed RCCS will also simplify the design. It was decided that the radiation heat shield must have a 9.5 m diameter. This leaves a 180 mm air space between the radiation heat shield and the concrete structure. This air space constrains the maximum pipe diameter of the closed loop thermosyphon heat pipes. It was decided that the maximum outside diameter of the heat pipes will be 180 mm so that the pipes will not decrease the air space between the radiation heat shield and the concrete citadel to less than 90 mm.

The surface temperature of the concrete citadel can also be kept within the specified limits by insulating the concrete structure or the heat shield. Bhat *et al.* (not dated) uses a 100 mm thick layer of mineral wool as insulation on the surface of the heat shield. When the surface temperature of the insulation reaches 278 °C, the heat shield temperature is only 54 °C in the design of Bhat *et al.* (not dated). The insulation creates a temperature drop of 224 °C from the air inside the reactor cavity to the heat shield. This allows Bhat *et al.* (not dated) to use a RCCS made from small diameter pipes with a temperature difference of only 6.6 °C between the risers and the downcomers. This small temperature difference shows that the RCCS of Bhat *et al.* (not dated) removes only a small amount of heat and that the insulation has the bigger influence on the concrete structure temperature. It was decided that there will be no insulation in the design of the RCCS in this thesis. The reason for this is that by using insulation, no actual cooling takes place. In an emergency situation, the decay heat must be removed by the RCCS, and partially by the concrete structure, from the reactor cavity to the environment. By insulating the heat shield as done by Bhat *et al.* (not dated), it will take more time to remove the decay heat from the reactor cavity and the thermal integrity of the fuel might be compromised.

A further constraint is that the RCCS must be constructed with standard sized flatbar for the fins and pipes for the closed loop thermosyphon heat pipes. The sizes of the flatbar and pipes that were considered are listed in Appendix D. The use of standard sized materials places a constraint on the number of different combinations of fins and pipes that can be used. Eleven pipes and eleven flatbars were selected from the catalogues in Appendix D. Table 7.1 shows the number of closed loop thermosyphon heat pipes that can be used for all the combinations of flatbar and pipe sizes. The number of thermosyphons to be used is fixed for each flatbar and pipe combination because the radiation heat shield diameter is fixed at 9.5 m as discussed previously. Table 7.2 shows the total mass of the RCCS for all the different combinations of fin and pipe sizes.

7.4 Optimisation procedure

The first step in the optimisation procedure is to calculate the maximum heat shield temperature and the maximum temperature of the concrete citadel for each combination of heat pipe inside diameter and fin width as well as different diameters for the cooling dam. The selected heat pipe diameters and fin widths have already been referred to and can be seen in Appendix D. The diameters of the cooling dam range from 20 m to 60 m with 10 m increments. There are thus 605 (11 heat pipes x 11 fins x 5 cooling dams) different RCCS designs that can be used. The 605 different input files for the theoretical model, as shown in Appendix E, needed to be created. The cooling dam diameter and the

Table 7.1: Number of thermosyphons for different pipe- and fin sizes and the Pressure loss coefficient of the pipes

ID (mm)	Wfin (mm)											PLk
	20	25	30	35	40	45	50	60	75	80	100	
18.85	448	389	344	309	280	256	236	203	169	160	132	0.4318
24.30	407	358	320	289	263	242	224	195	163	154	128	0.4052
32.46	363	324	292	266	244	226	210	184	155	148	123	0.3686
38.10	338	304	276	252	233	216	201	177	151	143	120	0.3456
49.25	297	271	248	229	213	199	186	166	142	135	115	0.3051
62.72	264	243	224	209	195	183	172	155	134	128	109	0.2645
73.66	232	215	200	188	177	167	158	143	125	120	103	0.2377
90.12	211	197	185	174	164	156	148	135	119	114	99	0.2063
102.26	193	182	171	162	154	146	139	127	113	109	95	0.1892
128.2	165	156	148	141	135	129	124	114	102	99	87	0.1664
146.33	143	137	131	125	120	116	111	104	94	91	81	0.1587

Table 7.2: Total mass of the RCCS for different pipe- and fin sizes (tons)

ID (mm)	Wfin (mm)										
	20	25	30	35	40	45	50	60	75	80	100
18.85	111	99	89	81	75	70	65	58	51	49	43
24.30	146	130	118	108	99	92	87	77	67	64	56
32.46	176	159	145	133	123	115	108	96	83	80	69
38.10	198	179	164	151	141	132	123	110	96	92	79
49.25	238	219	201	187	175	164	155	139	121	116	101
62.72	243	225	208	195	183	173	163	149	130	125	109
73.66	375	349	325	307	290	274	260	237	209	201	174
90.12	304	284	268	253	239	228	217	199	177	171	150
102.26	328	311	293	278	265	252	240	221	198	192	169
128.2	379	359	341	326	313	299	288	266	240	233	206
146.33	640	614	587	561	539	522	500	469	426	412	369

inside diameter of the heat pipes are given as inputs, but the input file does not define the width of the fin. The number of closed loop thermosyphon heat pipes must be taken from Table 7.1 and be specified in the input file. The number of closed loop thermosyphon heat pipes and the diameter of the radiation heat shield are used in the program to specify the width of the fins. The results of the 605 simulations can be seen in Appendix F. All the simulations were done for the ambient conditions given in Table 7.3. The simulation time was 10^6 s, or approximately 11.5 days.

The second step in the optimisation procedure is to use the data given in Appendix F to select the RCCS design with the smallest cooling dam and the lowest total mass as given in Table 7.2 that has a maximum concrete structure temperature of less than 65 °C. This selected RCCS will only satisfy the first condition given in Section 1.2. Next,

Table 7.3: Ambient conditions used for creating the temperature tables in Appendix F

T_{day}	25 °C
T_{night}	16 °C
Relative Humidity	0.5
Wind speed	1 m/s
Atmospheric pressure	101325 Pa

the RCCS must be tested for the second and third conditions. No studies have been done for the case where one thermosyphon heat pipe fails and the adjacent two thermosyphon heat pipes must compensate for the loss in cooling capacity of the RCCS. There is thus no specified maximum concrete structure temperature in the literature for this case. In order to be conservative, the maximum concrete structure temperature for this condition is taken as 65 °C. In the case of an emergency shut-down of the PBMR, the maximum concrete structure temperature is 125 °C.

The condition for when a thermosyphon heat pipe fails can be evaluated by adjusting the number of closed loop thermosyphon heat pipes. Under this condition, the number of active thermosyphon heat pipes is two thirds of the number of thermosyphon heat pipes given in Table 7.1. In order to satisfy the thermosyphon failure condition, a RCCS must be chosen from the tables in Appendix F where the concrete structure temperature is approximately 65 °C. The inside diameter of the heat pipes and the fin width can then be used to find the number of active thermosyphon heat pipes in Table 7.1. This number of thermosyphons must be multiplied by 1.5 to give the total number of thermosyphon heat pipes that will be active during normal operation. The total number of thermosyphon heat pipes and the heat pipe inside diameter can then be used to find the appropriate fin width in Table 7.1. The maximum concrete structure temperature under normal operating conditions can then be read from the tables in Appendix F using the inside diameter of the heat pipes and the new fin width. The RCCS must then be tested under normal operating conditions for an extended time period to verify the steady state operating temperature of the concrete structure. The reason for this is that the temperatures given in Appendix F is for simulations of 10^6 s and it is possible that a RCCS is not operating at a 100 % steady state after 10^6 s.

The third and final operating condition is when an emergency shut-down takes place and the RCCS must remove the decay heat from the reactor cavity. The theoretical model uses the decay heat as given in Section 2.6.3 to calculate the maximum concrete structure temperature under emergency conditions. The decay heat is then adjusted so that the theoretical model will have a RPV temperature of 527 °C as given in Section 2.6.2 to simulate a DLOFC emergency. For the purpose of this thesis, it is assumed that the water that evaporates from cooling dam can be replaced as needed. In order to comply with the requirements in Section 2.4, the mass flow rate of the feed water into the cooling dam must be set to zero for 72 hours after an emergency shut-down.

The last step in the optimisation of the RCCS is to test the performance of the chosen RCCS for different ambient conditions. The ambient conditions affect the cooling dam water temperature and the rate of evaporation from the cooling dam.

An additional step that can be implemented in the optimisation procedure is to use CLTHPs under vacuum conditions in order to decrease the total mass of the RCCS by fixing the maximum temperature of the working fluid to the saturation temperature at a low pressure. The expansion tanks can be evacuated in order to make the pressures in the top part of the thermosyphons 20 kPa. By doing this, two-phase flow will be induced in the thermosyphons and the maximum working fluid temperature will be the saturation temperature of the working fluid at 20 kPa, which is 65 °C for water. By using the saturation temperature of the water in the thermosyphons to keep the water temperature constant, it might be possible to use a RCCS with a lower total mass.

7.5 Comparison of the optimisation of a RCCS for two different sized cooling dams

The size of the cooling dam has a big effect on the maximum temperature of the concrete structure. For example, a RCCS with 18.85 mm inside diameter heat pipes and 20 mm wide fins with a 20 m diameter cooling dam has a maximum concrete structure temperature of 97 °C, while the same RCCS with a 30 m diameter cooling dam has a maximum concrete structure temperature of 83 °C. The size of the cooling dam should be carefully considered. The bigger the cooling dam, the more water will be needed to keep the cooling dam full because more water might evaporate from the cooling dam as a result of an increased surface area. However, by using a bigger cooling dam, one can reduce the total weight of the RCCS. For example, considering only normal operating conditions, the lightest RCCS with a 30 m diameter cooling dam that has a maximum concrete structure temperature of 65 °C has 90.12 mm inside diameter pipes, 25 mm wide fins and a total mass of 284 tons. If using a 40 m diameter cooling dam, 62.72 mm inside diameter pipes and 60 mm wide fins, the total mass is 149 tons. By increasing the cooling dam diameter by 10 m, the total mass of the RCCS is decreased by 135 tons. In order to find the optimal RCCS in terms of mass, the biggest possible cooling dam should be used. The biggest cooling dam will differ from plant to plant depending on the availability of water and the ambient conditions. In this comparison, it will be assumed that one PBMR can have a 40 m diameter cooling dam and another PBMR can have a 60 m diameter cooling dam. This comparison between two different RCCSs will also serve as an optimisation example and will follow the procedure as explained in Section 7.4.

Firstly, by using Tables F.5 and F.6 for the 40 m diameter cooling dam and Tables F.9 and F.10 for the 60 m diameter cooling dam, select the heat pipe inside diameter and the fin width for which the maximum concrete structure temperature is approximately 65 °C. This temperature corresponds to the maximum concrete structure temperature when there is a thermosyphon heat pipe failure. This temperature will be denoted by $T_{Con_i,f}$. Next, multiply the number of thermosyphons by 1.5 to satisfy the second condition in Section 1.2. The total mass of the RCCS can now be found in Table 7.2. These steps must be repeated until the lowest total mass of the RCCS is found.

For the 40 m diameter cooling dam, Table F.5 shows a maximum concrete structure temperature of 65 °C for heat pipes with 32.46 mm ID and 25 mm wide fins. This is the first RCCS to be tried in the optimisation. Table 7.1 shows that there is 324 active thermosyphons in this RCCS. This number must be multiplied by 1.5 to find the minimum

total number of closed loop thermosyphon heat pipes in the RCCS. The new number of heat pipes is thus 486. From Table 7.1, it can be seen that the maximum number of thermosyphon heat pipes for a 32.46 mm ID heat pipe is only 363. This RCCS can thus not be used.

A second RCCS that can be used is one with 49.25 mm ID heat pipes and 50 mm wide fins. The maximum concrete structure temperature under thermosyphon heat pipe failure conditions for this RCCS is 65.1 °C and the number of active thermosyphons is 186. The minimum total number of thermosyphons is thus 279, but Table 7.1 shows the closest to 279 is 297. The number of closed loop thermosyphon heat pipes will thus be 297. This RCCS has 20 mm wide fins and a total weight of 238 tons. From Table F.5, it can be seen that the maximum concrete structure temperature under normal operating conditions will be 58.7 °C. These same steps were repeated for larger heat pipes and the results are given in Table 7.4.

Table 7.4: RCCS optimisation with a 40 m diameter cooling dam

$T_{Con_i,f}$	ID	Wfin	Nhp_{active}	Min total Nhp	Nhp used	Wfin	RCCS mass	$T_{Con_i,n}$
65	32.46	25	324	486	na	na	na	na
64.1	38.1	30	276	414	na	na	na	na
64.1	49.25	45	199	299	na	na	na	na
65.1	49.25	50	186	279	297	20	238	58.7
63.5	62.72	60	155	233	243	25	225	57.6
64.7	73.66	80	120	180	188	35	307	58.5
64.3	90.12	100	99	149	156	45	228	58.2

As can be seen from Table 7.4, the optimal RCCS when using a 40 m diameter dam is one with 243 closed loop thermosyphon heat pipes constructed with 62.72 mm ID pipes and 60 mm wide fins. The total mass of the RCCS will be 225 tons. The same procedure was followed for optimizing the RCCS with a 60 m diameter cooling dam. The results are shown in Table 7.5. In the case where two possible RCCSs has the same total mass as in the last two cases in Table 7.5, the RCCS that has the highest normal operating temperature must be used. The highest normal operating temperature corresponds to the lowest parasitic heat removal from the reactor cavity.

As can be seen from Table 7.5, the optimal RCCS when using a 40 m diameter dam is one with 324 closed loop thermosyphon heat pipes constructed with 32.46 mm ID pipes and 25 mm wide fins. The total mass of the RCCS will be 159 tons.

Table 7.5: RCCS optimisation with a 60 m diameter cooling dam

$T_{Con_i,f}$	ID	Wfin	Nhp_{active}	Min total Nhp	Nhp used	Wfin	RCCS mass	$T_{Con_i,n}$
64.4	32.46	50	210	315	324	25	159	56.8
63.6	38.1	60	177	266	276	30	164	56
62.7	49.25	80	135	203	213	40	175	55.1

The RCCSs can now be tested under emergency shut-down conditions. Only the PLOFC emergency condition will be considered in these sample optimisations. The simulations were run until the RCCS reached equilibrium and then the decay heat was switched on. Figures 7.1 and 7.2 shows the temperatures of the heat shield and the inside surface of the concrete citadel as a function of time for the RCCSs with cooling dam diameters of 40 m and 60 m respectively.

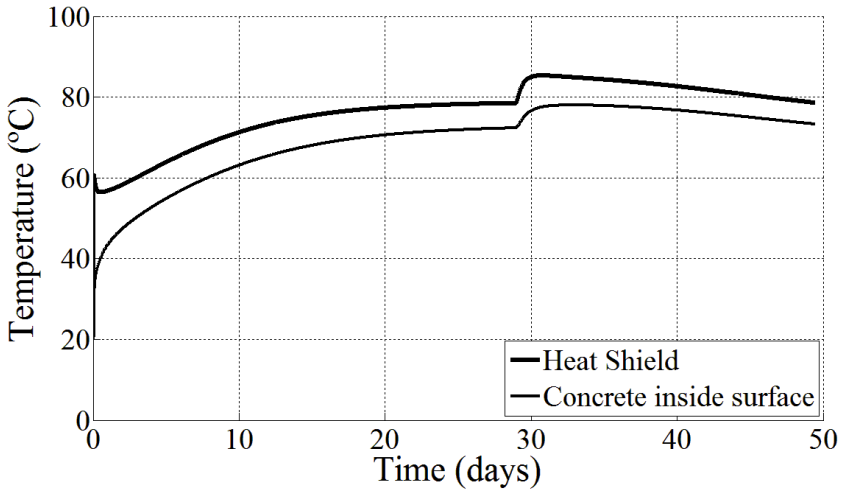

Figure 7.1: Temperature of the heat shield and the concrete citadel for a RCCS with a 40 m diameter cooling dam

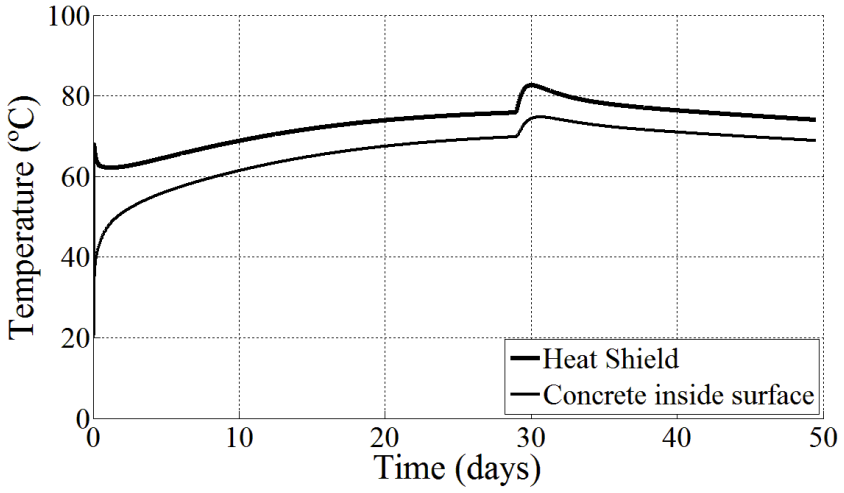

Figure 7.2: Temperature of the heat shield and the concrete citadel for a RCCS with a 60 m diameter cooling dam

As can be seen from figures 7.1 and 7.2, the RCCSs reaches equilibrium after approximately 28 days after start up. The maximum heat shield temperatures are 85 °C and 83 °C for the 40 m diameter and 60 m diameter cooling dams respectively. The maximum concrete structure temperatures are 78 °C and 75 °C for the 40 m diameter and 60 m

diameter cooling dams respectively.

Figures 7.3 and 7.4 shows the temperatures of the water in the cooling dams at the top and bottom of the dams as a function of time for the two RCCSs. The 40 m diameter cooling dam has a maximum temperature of 65 °C and the 60 m diameter cooling dam has a maximum temperature of 53 °C. Using a bigger dam results in a 3 °C colder concrete structure and a 12 °C cooler cooling dam.

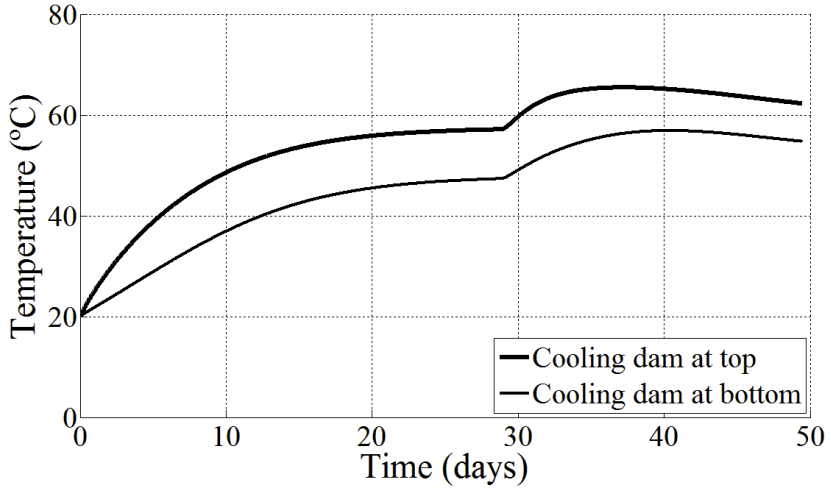

Figure 7.3: Temperatures of the cooling dam at the top and bottom for a RCCS with a 40 m diameter cooling dam

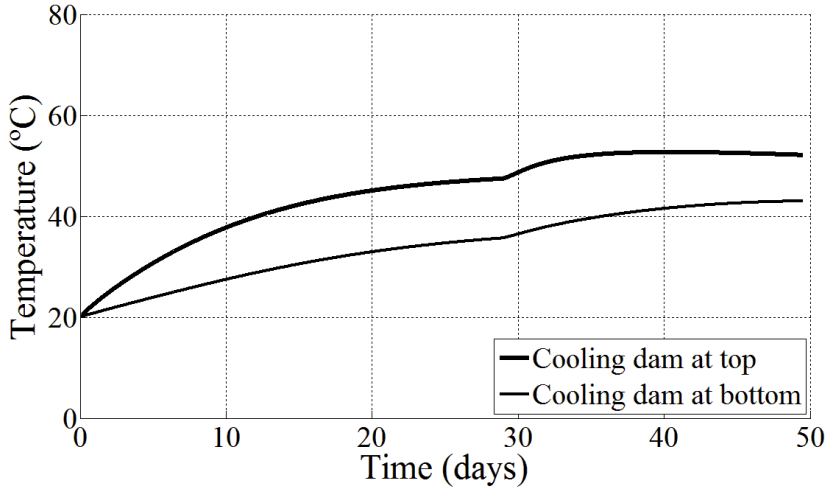

Figure 7.4: Temperatures of the cooling dam at the top and bottom for a RCCS with a 60 m diameter cooling dam

Figures 7.5 and 7.6 shows the mass flow rate in the thermosyphon heat pipes and the rate of evaporation from the cooling dams as a function of time for the two RCCSs. The RCCS with the 40 m diameter dam has a maximum mass flow rate in the heat pipes of 0.128 kg/s and the RCCS with the 60 m diameter dam has a maximum mass flow rate in

heat pipes of 0.1 kg/s. It is expected for the RCCS operating at a lower temperature of the working fluid to have a lower mass flow rate in the heat pipes. The rate of evaporation from the 60 m cooling dam is 0.043 kg/s and 0.034 kg/s from the 40 m cooling dam. This is also expected because the rate of evaporation increases with water temperature.

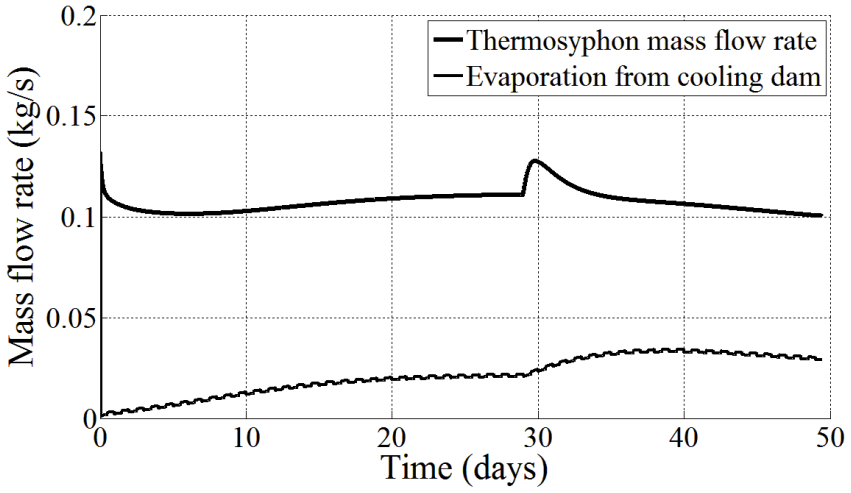

Figure 7.5: Mass flow rate in the thermosyphon heat pipes and the rate of evaporation from the 40 m diameter cooling dam

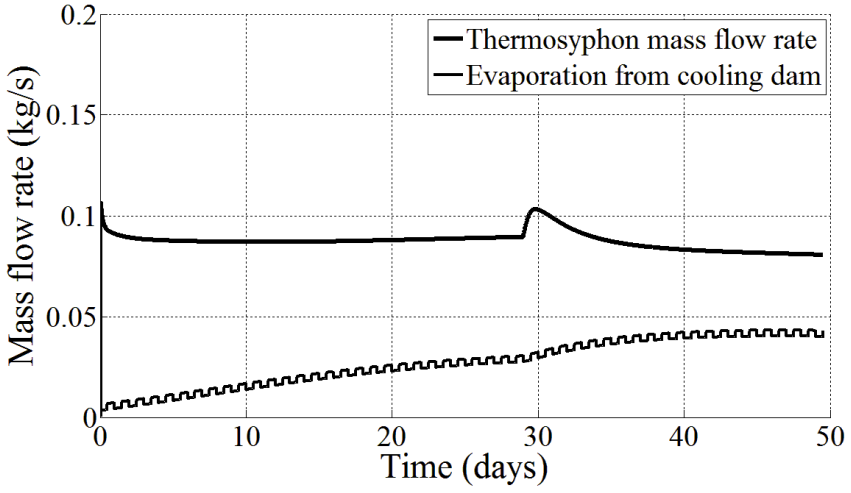

Figure 7.6: Mass flow rate in the thermosyphon heat pipes and the rate of evaporation from the 60 m diameter cooling dam

This comparison shows that if cooling water is readily available, using a large cooling dam can be very effective in reducing the total weight of the RCCS. In this example, the RCCS total weight is reduced by 66 tons by using a 60 m diameter cooling dam instead of a 40 m diameter cooling dam. A two-phase flow example is not given in this sample comparison, but a two-phase optimisation will be given in the final design in Chapter 8.

Chapter 8

Results

This chapter shows how the optimisation of the RCCS was done. The final results include the simulation of the RCCS under all the different operating conditions. The optimisation was done for the PBMR demonstration power plant.

8.1 The PBMR demonstration power plant

The PBMR demonstration power plant will be constructed next to the Koeberg power station on the west coast of South Africa. It is important to make some assumptions regarding the environmental conditions at the demonstration plant since the ambient conditions has an effect on the RCCS performance as was shown in Section 6.2. The sea water will be used as feed water to the cooling dam to make up for the water losses from the cooling dam due to evaporation. The average Koeberg sea water temperature is approximately 13 °C (Slabber, 2006). The wind speed in summer can reach 60 km/h and the ambient air temperature can reach 35 °C. These values are used to test the optimal RCCS. Building a PBMR next to the sea holds a great advantage from a RCCS design point of view in that cooling water is available in abundance. This means that a large cooling dam can be built in order to save in total RCCS material weight and cost. A 50 m diameter cooling dam was used for the PBMR demonstration plant optimisation.

8.2 Radiation Heat Shield optimisation for normal operating conditions

The radiation heat shield optimisation is done using Tables F.7 and F.8 for the concrete structure surface temperatures. The results can be seen in Table 8.1.

Table 8.1: Radiation heat shield optimisation for normal operating conditions and a thermosyphon heat pipe failure using a 50 m diameter dam

$T_{Con_i,f}$	ID	Wfin	Nhp_{active}	Min total Nhp	Nhp used	Wfin	RCCS mass	$T_{Con_i,n}$
58.6	62.72	60	155	233	243	25	225	52.6
59.8	73.66	80	120	180	188	35	307	53.6
59.6	90.12	100	99	149	156	45	228	55.1

Using the optimisation procedure outlined in Section 7.4, it was found that the optimal RCCS radiation shield has 243 closed loop thermosyphon heat pipes constructed from 62.72 mm ID pipes and 25 mm wide flarbat fins. The total mass of the RCCS is 225 tons. As stated in Section 7.4, the RCCS was tested under normal operating conditions for $5x10^6$ s to verify the steady state concrete structure temperature. The steady state temperatures of the heat shield and the concrete structure can be seen in figure 8.1. As can be seen from the figure, the steady state temperature is almost 10 °C higher than what was predicted in Appendix F.

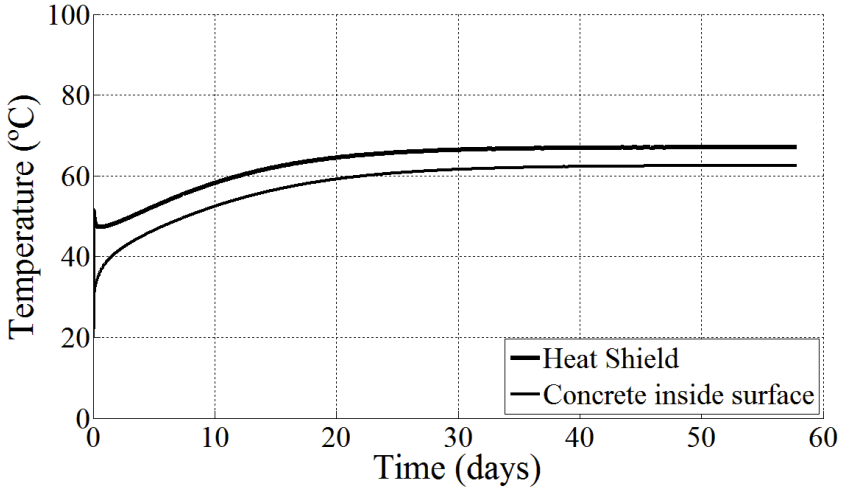

Figure 8.1: Steady state temperatures of the HS and concrete structure of the proposed RCCS

Figure 8.1 shows that the proposed RCCS will result in a concrete structure temperature of 62.5 °C. The RCCS can thus be used under normal operating conditions. This RCCS can now be tested in emergency shut-down conditions.

8.3 Testing of the RCCS during emergency shut-downs

The proposed RCCS is tested for both a PLOFC and a DLOFC emergency shut-down. The decay heat for the PLOFC is used as given in Section 2.6.3 by equation (2.6.1). For the DLOFC emergency condition, the decay heat will have the same profile as given by equation (2.6.1), but the magnitude is adjusted in such a way that the maximum RPV temperature will be approximately 527 °C as given by Slabber (2006). All simulations had a total simulation time of $5x10^6$ s and the emergency shut-down started after $3x10^6$ s into the simulations. The ambient temperatures were 35 °C during the day and 16 °C during the night. The wind speed was 1km/h.

Figures 8.2 and 8.3 show the HS and concrete structure temperatures as a function of time for the PLOFC and DLOFC emergency conditions respectively. The maximum concrete structure temperatures are 65.8 °C and 80.9 °C for the PLOFC and DLOFC

shut-down conditions respectively. The decay heat for the DLOFC condition was adjusted to twice that of the PLOFC condition in order to let the RPV get up to 530.3 °C. This is very close to the 527 °C suggested by Slabber (2006). The maximum concrete structure temperature is well below the specified maximum temperature of 125 °C for emergency shut-down conditions.

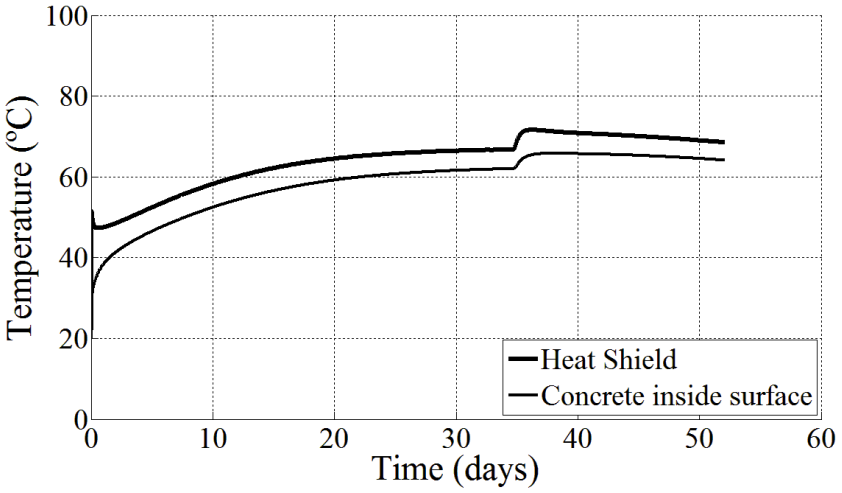

Figure 8.2: HS and concrete structure temperatures of the proposed RCCS during a PLOFC emergency shut-down

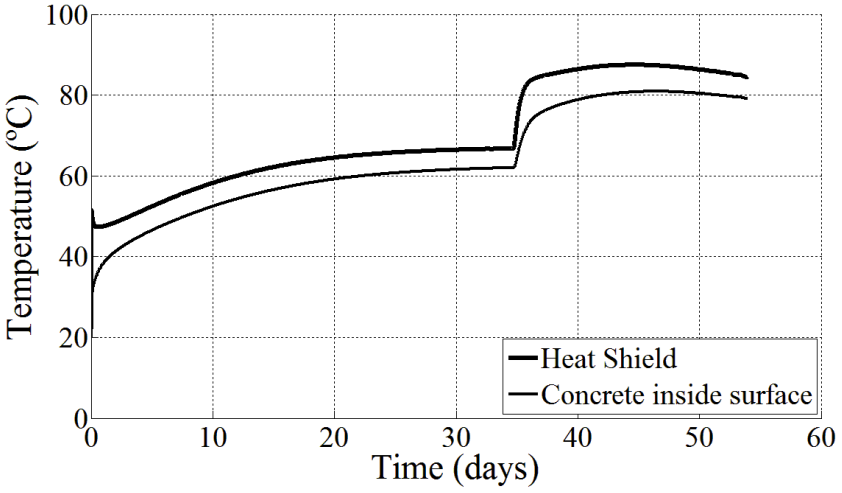

Figure 8.3: HS and concrete structure temperatures of the proposed RCCS during a DLOFC emergency shut-down

Table 8.2 summarizes the proposed RCCS performance during normal operating conditions as well as during the two different emergency shut-down conditions. As can be seen from Table 8.2, the PLOFC emergency condition does not have a great influence on the temperature of the concrete structure. The concrete structure temperature increases by only 3.3 °C. The DLOFC shut-down condition increases the concrete structure temperature by 18.4 °C.

Table 8.2: Maximum temperatures and working fluid mass flow rates during normal operating conditions as well as during the emergency shut-down conditions

	Normal	PLOFC	DLOFC
T_{RPV}	366.1	413.9	530.3
T_{HS_i}	67.0	71.6	87.5
T_{Con_i}	62.5	65.8	80.9
T_{dam}	50.2	56.0	67.3
$\dot{m}$	0.2518	0.287	0.3795

8.4 Testing of the RCCS during emergency shut-downs while there are thermosyphon heat pipe failures

As stated in Section 1.2, in the case of a thermosyphon heat pipe failure, the adjacent thermosyphon heat pipes must be able to compensate for the loss of cooling capacity. This implies that if a third of the closed loop thermosyphon heat pipes fail, the concrete structure temperature must still not exceed 65 °C. This requirement also stands during an emergency shut-down condition, where the maximum concrete structure temperature must not exceed 125 °C. Since the DLOFC emergency shut-down has a more severe effect on the concrete structure temperature than the PLOFC emergency shut-down, only the DLOFC emergency shut-down needs to be considered.

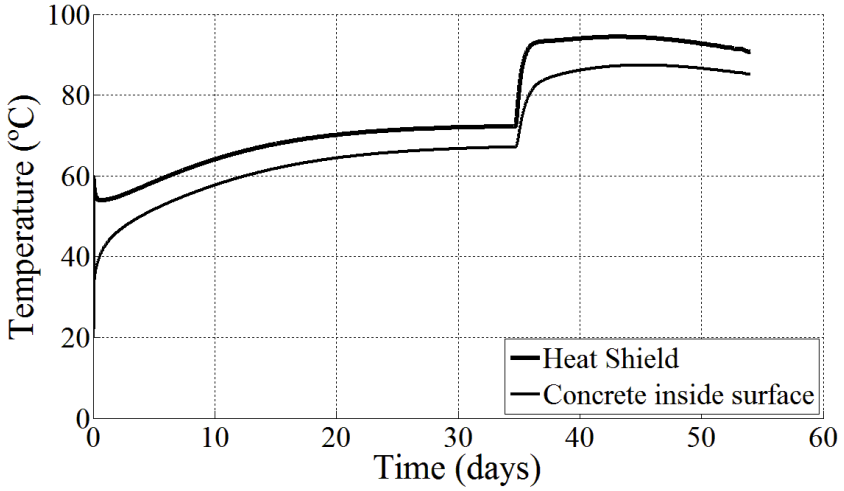

Figure 8.4: HS and concrete structure temperatures for the proposed RCCS during a DLOFC emergency shut-down with only two thirds of the thermosyphon heat pipes working

As can be seen from the figure, the maximum concrete structure temperature is 87.4 °C. The maximum RPV and HS temperatures are 531.7 °C and 94.4 °C respectively. The cooling dam temperature is 67.8 °C and the maximum working fluid mass flow rate is 0.4527 kg/s.

8.5 Testing of the RCCS during lower ambient temperatures and higher wind speeds

The RCCS has been tested for ambient conditions where the air temperature is 35 °C and the wind velocity is 1 km/h. With the demonstration plant situated near the sea on the West Coast, this does not represent the dominant ambient conditions in which the RCCS will need to operate. The ambient conditions on the West Coast are characterized by cooler ambient temperatures and higher wind speeds. This will enhance the performance of the RCCS.

Figure 8.5 shows the temperatures of the HS and the concrete structure when the ambient air temperature is 25 °C and the wind speed is 1 km/h. The maximum HS temperature is 66.4 °C and the maximum concrete structure temperature is 61.6 °C. Figure 8.6 shows the temperatures of the HS and the concrete structure when the ambient air temperature is 25 °C and the wind speed is 40 km/h. This higher wind speed results in that the maximum concrete structure temperature is 47.1 °C. This shows the significant effect the wind speed has on the performance of the RCCS.

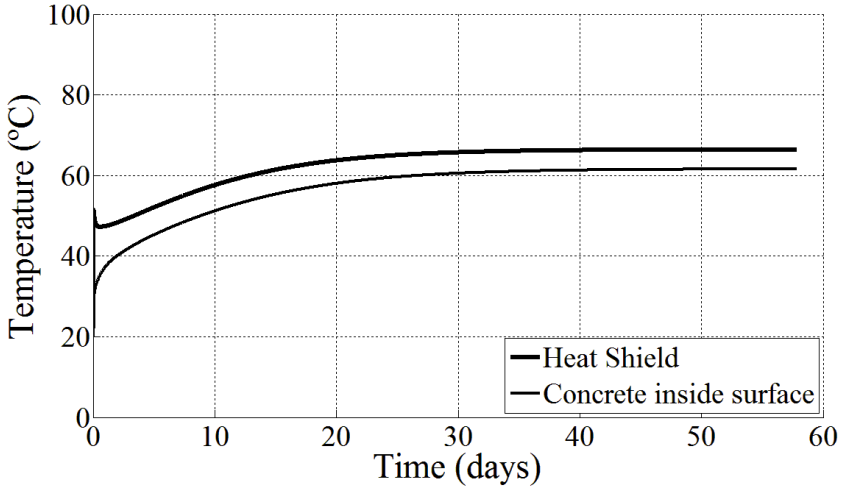

Figure 8.5: HS and concrete structure temperatures for the proposed RCCS with the ambient air at 25 °C

Table 8.3 shows the maximum temperatures of the RPV, the HS, the concrete structure and the cooling dam water as well as the maximum mass flow rate for different ambient conditions. As can be seen by the results, the cooling dam water temperature drops dramatically at higher wind speeds. This, in turn, results in a cooler concrete structure.

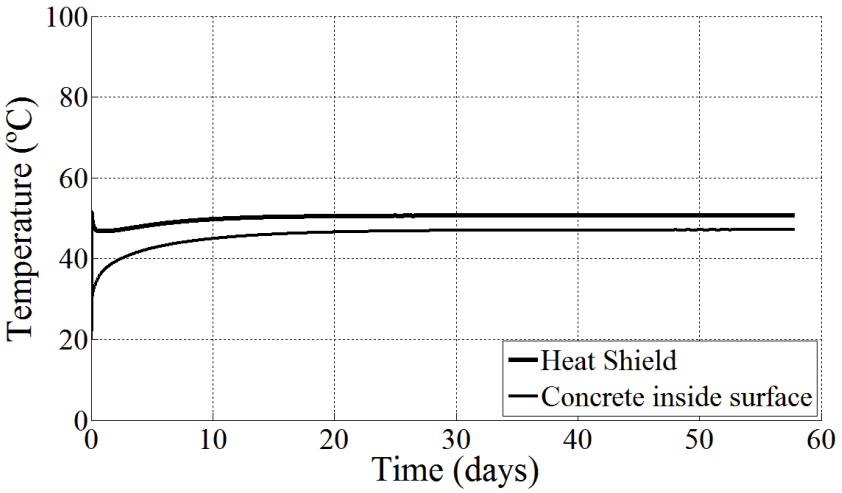

Figure 8.6: HS and concrete structure temperatures for the proposed RCCS with the ambient air at 25 °C and a wind speed of 40 km/h

Table 8.3: Maximum temperatures and working fluid mass flow rates during normal operating conditions in different ambient conditions

	25 °C air & 1 km/h wind	25 °C air & 40 km/h wind
T_{RPV}	366.0	362.2
T_{HS_i}	66.4	50.6
T_{Con_i}	61.6	47.1
T_{dam}	49.4	29.2
$\dot{m}$	0.2503	0.2235

8.6 Further improvement of the RCCS design by using two-phase flow in the closed loop thermosyphon heat pipes

By using only single phase flow in the closed loop thermosyphon heat pipes, the latent heat of evaporation of the working fluid is never utilized. This restricts the optimisation of the RCCS and the lowest total mass of a RCCS that can be used is 225 tons. The method of using two-phase flow in the closed loop thermosyphon heat pipes has been explained in Section 7.4. If studying Table G.1, it can be seen that heat pipes with diameters of 18.85 mm or 24.3 mm cannot be modelled. This is because the heat pipes do not have enough working fluid in them and as boiling starts, the quality of the liquid-vapour mixture approaches unity, thus the density is so low that there is virtually no pressure and therefore no mass in the control volume. This causes numerical instability and the homogeneous flow model cannot capture these types of flow conditions.

Since the current proposed RCCS is using 62.72 mm ID pipes, the only pipes that can be used that can possibly result in a lower total RCCS weight are 32.46 mm, 38.1 mm and 49.25 mm ID pipes. The cooling dam diameter that is used will still be 50 m. Table 8.4 shows the HS and concrete structure temperatures for RCCSs with different fin widths operating under vacuum pressure.

Table 8.4: Temperatures of the heat shield and the concrete structure surface for thermosyphon heat pipe inside diameters of 32.46 mm to 49.25 mm with a 50 m diameter cooling dam under vacuum conditions.

	ID (mm)					
Wfin	32.46		38.1		49.25	
	T_{HS_i}	T_{Con_i}	T_{HS_i}	T_{Con_i}	T_{HS_i}	T_{Con_i}
20	64.3	57.7	63.1	56.3	60.0	53.6
25	65.5	58.9	64.1	57.5	61.3	54.8
30	66.6	60.0	65.0	58.4	62.6	55.9
35	67.7	61.0	66.0	59.4	63.8	57.0
40	68.7	62.0	66.8	60.2	64.8	58.1
45	69.6	62.9	67.7	61.0	65.4	58.8
50			68.5	61.8	66.1	59.5
60			70.0	63.3	67.2	60.6
75					68.9	62.3
80					69.6	62.9
100					71.5	64.7

By using Table 8.4, the optimal RCCS was found to be one with 276 closed loop thermosyphon heat pipes consisting of 38.1 mm ID pipes with 30 mm fins. The total mass of this RCCS is 164 tons. This is 61 tons less than the optimal RCCS for single phase flow. By using this RCCS, the concrete structure temperature could be maintained at 62 °C for normal operating conditions. However, during a PLOFC emergency shut-down, the working fluid in the RCCS boils to such an extent that the density in the thermosyphon heat pipe drops to below 20 kg/m^3. In such low density areas, there is virtually no heat transfer and the theoretical model becomes instable. It was decided to rather use 20 mm wide fins with the 38.1 mm ID pipes to create a RCCS with 338 closed loop thermosyphon heat pipes with a total weight of 198 tons, 27 tons lighter than the single phase RCCS discussed in Section 8.2. The HS and concrete structure temperatures are shown in figure 8.7 for the RCCS under normal operating conditions.

As can be seen from figure 8.7, the concrete structure temperature stays constant at 60 °C under normal operating conditions. The effect of the boiling and condensation of the working fluid can be seen in the fact that after approximately 12 days after start-up, both the HS and the concrete structure temperatures increases at a lower rate. Figures 8.8 and 8.9 shows that the concrete structure temperature only increases by approximately 1 °C in an ambient temperature of 35 °C and drops by 9 °C if there is a 40 km/h wind.

In the case where a CLTHP fails and the adjacent two CLTHPs must provide adequate cooling of the HS, the RCCS under vacuum performs well. As can be seen from figure 8.10, the concrete structure temperature never exceeds the specified maximum temperature of 65 °C. With only 225 CLTHPs working, the maximum concrete structure temperature is 63.7 °C.

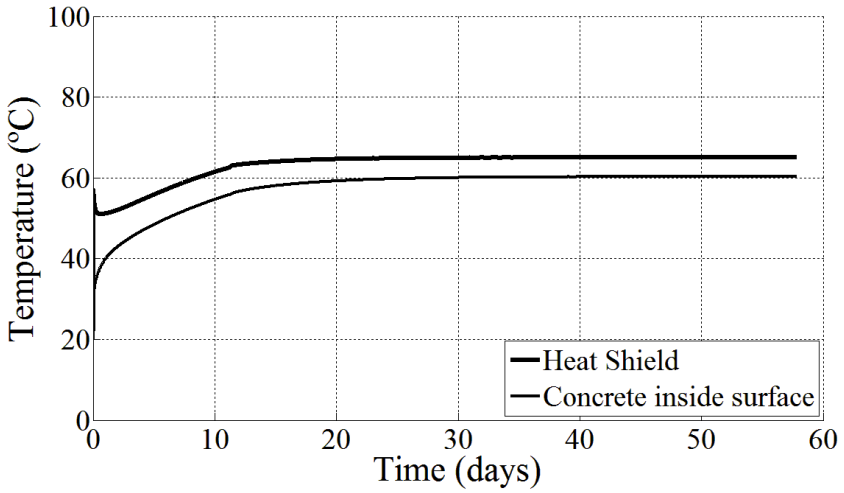

Figure 8.7: HS and concrete structure temperatures for the proposed RCCS under vacuum pressure under normal operating conditions

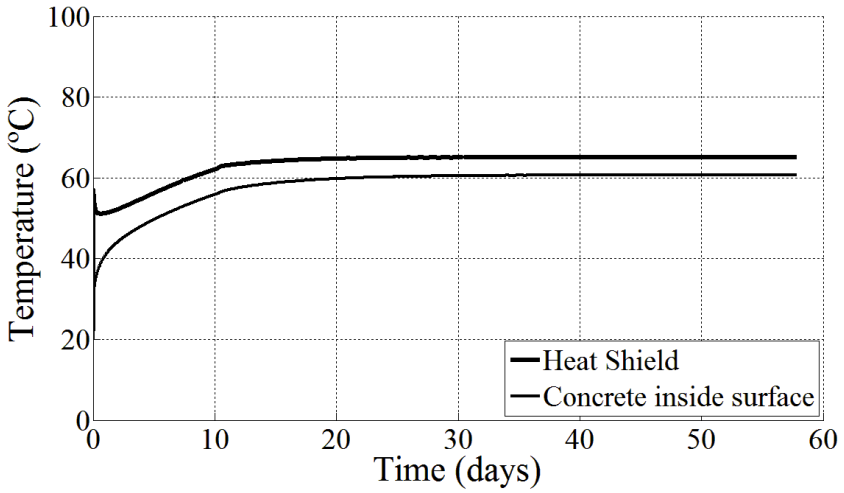

Figure 8.8: HS and concrete structure temperatures for the proposed RCCS under vacuum pressure under normal operating conditions with an ambient temperature of 35 °C

During a PLOFC shut-down emergency, the maximum concrete structure temperature is 62 °C as can be seen from figure 8.11. The corresponding maximum mass flow rate in the heat pipes is 0.14 kg/s as can be seen from figure 8.12.

Table 8.5 is a summary of the performance of the RCCS under vacuum pressure. The ambient temperature of the normal operating condition was 25 °C. The wind velocity was 1 km/h. The maximum concrete structure temperature during a PLOFC shut-down is 62.3 °C. This is 62.7 °C degrees below the specified maximum temperature of 125 °C and 3.5 °C below the maximum concrete structure temperature of the single phase RCCS of 65.8 °C.

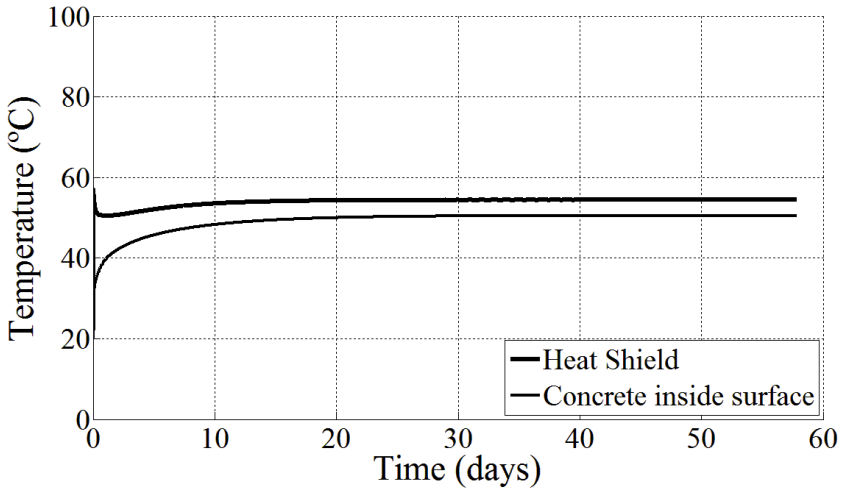

Figure 8.9: HS and concrete structure temperatures for the proposed RCCS under vacuum pressure under normal operating conditions with a wind speed of 40 km/h

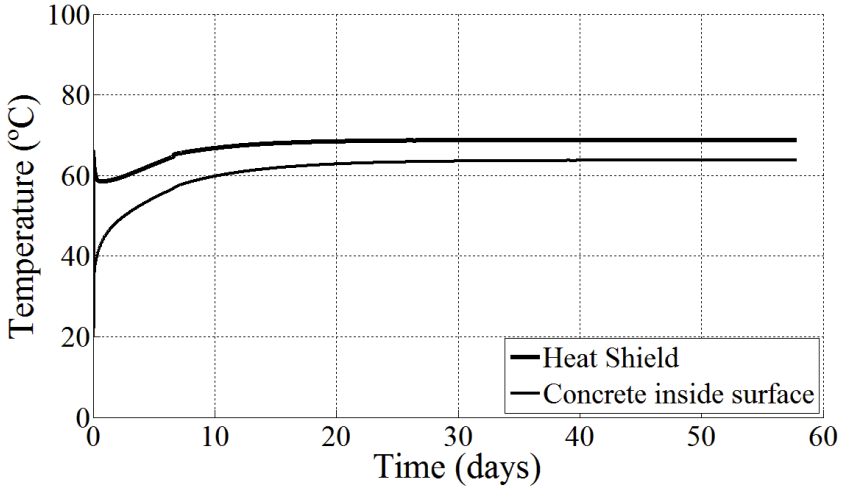

Figure 8.10: HS and concrete structure temperatures for the proposed RCCS under vacuum pressure under normal operating conditions with a CLTHP failure

Table 8.5: Maximum temperatures and working fluid mass flow rates for different operating conditions for the two phase RCCS

	Normal	CLTHP failure	40 km/h wind	35 °C air	PLOFC
T_{RPV}	365.7	366.6	363.1	365.7	413.3
T_{HS_i}	65.0	68.7	54.4	65.1	68.1
T_{CS_i}	60.3	63.7	50.5	60.7	62.3
T_{dam}	47.2	46.0	30.9	47.5	50.0
$\dot{m}$	0.114	0.1404	0.091	0.1166	0.1361

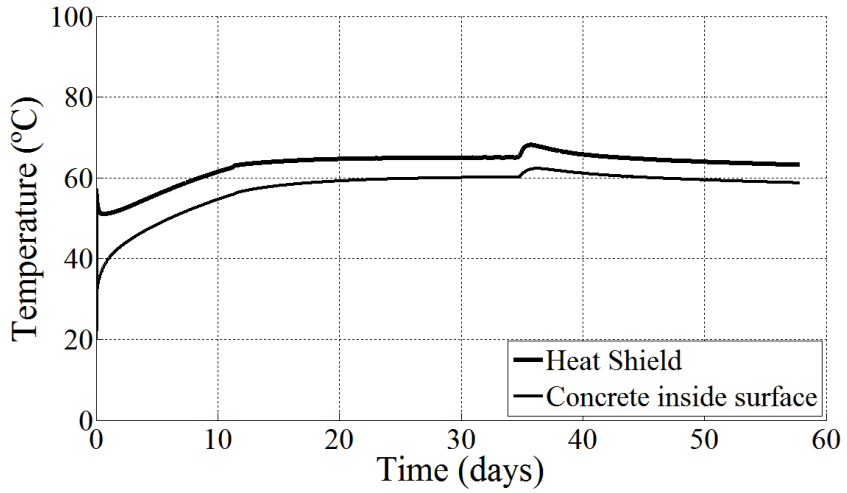

Figure 8.11: HS and concrete structure temperatures for the proposed RCCS under vacuum pressure for a PLOFC shut-down

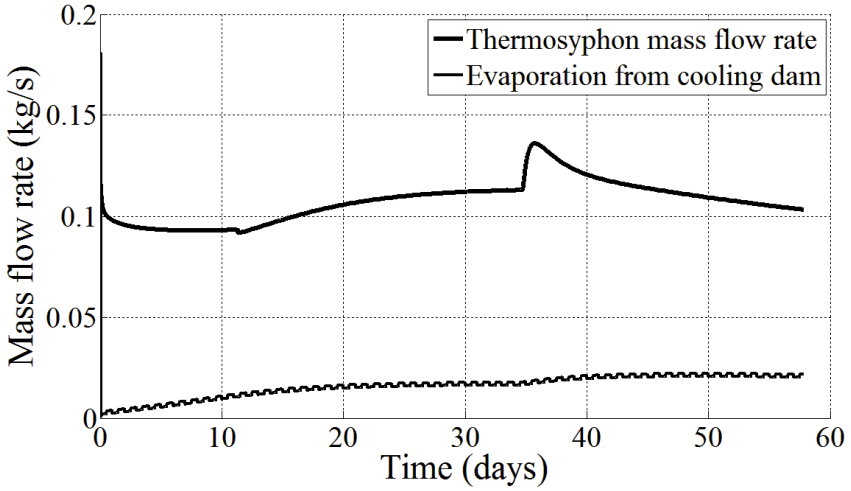

Figure 8.12: Mass flow rate in the heat pipes for the proposed RCCS under vacuum pressure for a PLOFC shut-down

Chapter 9

Discussion and Conclusion

The thesis presented the background theory needed to establish the important requirements of a passive RCCS, the applicable theory for modelling the heat transfer of a RCCS and in particular, the heat and mass transfer in closed loop thermosyphon heat pipes (CLTHPs). The thesis shows how the heat transfer capabilities of CLTHPs can be used to develop a totally passive RCCS suitable for the PBMR.

The background research in the literature study gave an insight of the philosophy of passive systems and how they are incorporated in the design of nuclear power plants where safety is the primary design variable. The literature study gave the requirements of the PBMR RCCS as well as the current design. The current design and the requirements of the PBMR RCCS formed the basis of the conceptual design of the RCCS presented in this thesis.

The different operating conditions under which the RCCS must be able to perform was investigated and the theoretical model was established to simulate these conditions. The transient response of the reactor during emergency shut-down conditions was investigated. The PLOFC emergency shut-down condition is well understood and the heat load on the RCCS during this event can be accurately described by using the decay heat of the reactor. The heat load on the RCCS during a DLOFC emergency shut-down condition could not be found in literature and the heat load needed to be approximated using the specified maximum temperature of the RPV during this event as given by Slabber (2006). It was determined that the decay heat for the PLOFC emergency shut-down condition must be doubled for the DLOFC emergency shut-down condition, because this resulted in a maximum RPV temperature corresponding closely to the value specified by Slabber (2006).

The effective thermal conductivity of the reactor has an important role in the transient analysis of the reactor. The effective thermal conductivity needed to be determined so that the heat transfer from the reactor core to the RPV would be the same as was found by Van Staden (2004) using a CFD analysis of the PBMR core. The effective thermal conductivity of the reactor was approximated conservatively as the load on the RCCS is 2.35 MW in this theoretical model whereas it is 2.21 MW in the model of Van Staden (2004).

All the radiation view factors in the reactor were determined analytically. The view factors needed to be determined for each vertical element of the theoretical model since

the temperatures of each of the vertical elements were different. Radiation view factors for each vertical element to all the vertical elements of the opposing surfaces were determined.

The theoretical modelling of the convection in the reactor cavity, especially the convection from the RPV to the radiation heat shield (HS), proved to be very difficult. The reactor cavity can be assumed to be infinitely wide since it is round. A 1D model is thus a fair representation of the enclosure. However, the enclosure of the experiment is not infinitely wide and had to be modelled as convection in an enclosed rectangle. This is essentially a 3D problem, but the 1D theoretical model was adjusted by multiplying the Nusselt number of the 1D theoretical model by 3. This new Nusselt number was then used to model the convection heat transfer. The current theoretical model thus uses a Nusselt number adapted for an enclosure of finite width. This is considered as being conservative since the reactor cavity is large enough to be considered as infinite. This assumption can be made because temperatures of the 350 mm wide enclosure in the experimental work corresponded well with the theoretical values where the Nusselt number was not multiplied by 3. In keeping with the safety philosophy of passive cooling design, the theoretical model was set up in a conservative manner. The grid size was set to 12 elements in the vertical direction to ensure that the concrete structure temperature is predicted higher than what a theoretical model will predict with a larger number of vertical elements. For example, a theoretical model with 12 vertical elements predicts that the maximum working fluid temperature will be 72.9 °C, whereas a theoretical model with 24 vertical elements predicts a maximum working fluid temperature of 68.8 °C. Furthermore, it was assumed that there is no temperature drop over the thickness of the RPV and the radiation heat shield emissivity was assumed to be 0.8. Also, the wind speed was assumed to be only 1 km/h for the optimisation of the RCCS.

The first part of the research objectives as listed in Section 1.3 was to create a theoretical model of the heat transfer of a RCCS. The simplifying assumptions for the modelling of CLTHPs were investigated with the literature study and implemented in the computer program. The explicit method is used by the computer program as is used by Dobson and Ruppersberg (2006). The model was investigated for grid independence and the response of the model to various changes in material properties was investigated.

The second part of the research objectives was met by the construction of a 2 m high experimental apparatus that can test three different heat shields in order to validate the theoretical model. The model is a scale model of the PBMR in the horizontal, or main heat transfer, direction. A problem with the experimental apparatus was the inability to completely insulate the enclosed cavity. The result of this was that the temperatures measured at the bottom of the heat shield and concrete structure were low compared to the temperatures in the middle and top of the heat shield and concrete structure.

A RCCS optimisation procedure was developed. Unlike derivative based numerical optimisation, the optimisation procedure presented in this thesis uses data tables. The optimisation procedure is used to select the RCCS that has the lowest total mass for a given cooling dam size that can be used to keep the concrete citadel below 65 °C during normal operating conditions and below 125 °C during an emergency shut-down. The advantage of the optimisation method is that the theoretical model used as the optimisation tool can do a month simulation in 10 minutes on a 3 GHz computer. This is very quick in comparison with CFD simulations. The model can be easily adjusted for differently sized

heat shields. The optimisation can give good RCCS design options that can be verified using a CFD analysis. The optimisation was done for both single phase flow and two phase flow of the working fluid in the CLTHPs. The two phase flow RCCS has a lower total mass than the RCCS that only works with single phase flow. Although the two phase flow RCCS performs better during normal operating conditions as well as during a PLOFC emergency shut-down than the single phase flow RCCS, it could not be simulated for the DLOFC emergency shut-down condition due to numerical instabilities. Using the optimisation procedure presented in this thesis, the optimum RCCS that operates only with single phase flow has a total mass of 225 tons and the optimum RCCS that uses both single and two phase flow has a total mass of 198 tons.

Numerical instabilities in the theoretical model during two phase flow in the CLTHPs had a limiting effect of the optimisation of the two phase flow RCCS. The chosen RCCS for the optimisation of the two phase RCCS might not be the optimum, or lightest, RCCS. This is because the smaller the heat pipes in the RCCS is, the lower the density will be because there is less water to absorb and transfer the heat from the heat shield. Low densities causes numerical instabilities in the homogenous flow model because control volumes are essentially vacuums in the CLTHP and then the saturation temperature drops and a low temperature control volume results from equation (9.1) as first given in Section 3.2.

$$T_i^{t+\Delta t} = T_{Sat@P_i} \tag{9.1}$$

This low temperature control volume gets colder with each time step. This problem might be breached by using a six equation slip-flow model, where the three conservation equations are solved separately for the vapour and liquid in the CLTHP. The six equation slip-flow model is used by Reyes (2005). In order to optimise a two phase flow RCCS, a deeper understanding of boiling, condensation and void fractions is needed. This is an extremely complex field of study and was done only in its simplest form for the purpose of the thesis, since it is unlikely that a two phase flow RCCS could be used with the same confidence as a single phase flow RCCS and it was shown that a single phase RCCS could be used in the PBMR. A single phase flow RCCS should be used in the PBMR because a CLTHP at vacuum pressure is a safety risk, because if a CLTHP with a small inside diameter (as a two phase RCCS would have) suddenly operates at atmospheric pressure, the temperature of the working fluid will increase above the specified limit of the CLTHP as specified for vacuum operating conditions.

In closure, it can be said that the modelling and design of a RCCS, especially a two phase flow RCCS, requires a detailed knowledge of heat and mass transfer as well as nuclear reactor transients. The 1D theoretical model presented in this thesis can be used to find the optimal single phase flow RCCS for a PBMR once the maximum size of the cooling dam is known. The RCCS is entirely passive during emergency shut-down conditions. This is an improvement of the current PBMR RCCS.

Chapter 10

Recommendation

The modelling of the RCCS was done using basic heat transfer principles and the laws of mechanics. This is adequate for a first-run design and optimisation procedure as was necessary in this project. The single phase flow CLTHP is well understood and its behaviour has been shown to be well simulated and hence the experimental values can be predicted accurately. However, the two phase flow CLTHP is modelled in a limited way. This is because the homogeneous flow model is used. By using a more complex model like the six equation slip-flow model as used by Reyes (2005), the two phase flow behaviour could be more accurately described. Modelling of two phase flow CLTHPs are further complicated by the need to verify and validate the theoretical results, because a fully operational CLTHP must be used in the experiment, unlike the experimental apparatus used in this thesis where only a section of the riser pipe of the CLTHP was used. For a single phase flow experiment, the working fluid can be pumped through the riser at a constant mass flow rate whereas for a two phase flow experiment, a fully operational CLTHP must be used so that natural circulation can take place in the CLTHP. A two phase flow experiment must be a full scale model of the PBMR RCCS. The reason for this is that an experiment representing only a section of the RCCS as is used in this thesis will not induce boiling in the working fluid because the heat load on the radiation heat shield is too low. This means that for the mass flow rate that will exist in the CLTHP, the working fluid will not have enough time to start boiling before being cooled in the condenser section of the CLTHP. Building a full scale experimental apparatus will be expensive, but this is recommended as a further study in proving the suitability of the current RCCS design for the actual PBMR as well as investigating a two phase flow RCCS. If a six equation slip-flow model, or a similar model, could be verified with experimental results, the optimisation of two phase flow RCCS could be done more accurate than what is presented in this thesis.

There are mainly two ways to further improve the design of the RCCS. Firstly, a more complex fin-heat pipe configuration can be developed as is shown in figure 10.1. The aim of this would be to improve the fin efficiency. This will obviously be more expensive than the use of standard parts as was an optimisation objective for this thesis. The current fin-heat pipe configuration is constructed from standard sized flatbar and pipe as shown in figure 10.2.

The second way to improve the RCCS is by improving the design of the cooling dam. By looking at the convection heat transfer equation describing the heat transfer from the downcomer of the CLTHP to the water in the cooling dam, $\dot{Q}_{water-dam} = hA(T_{water} - T_{dam})$, one can see that the heat transfer will increase for either an enlarged

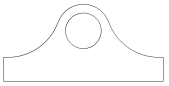

Figure 10.1: A recommended, more complex fin-heat pipe configuration

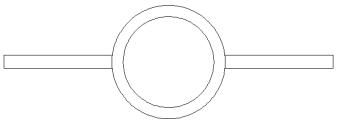

Figure 10.2: The current fin-heat pipe configuration constructed from standard parts

surface area or a greater temperature difference. Instead of making the dam larger to increase the temperature difference between the cooling water and the CLTHP surface, one can increase the convection surface area by immersing a part of the top horizontal pipe of the CLTHP into the cooling dam. This will condense the vapour in the top horizontal pipe during two phase flow and induce a greater density difference in the CLTHP. This, in turn, will increase the mass flow rate of the working fluid in the CLTHP and increase the heat transfer rate.

A further investigation of the convection heat transfer form the RPV to the HS must be done. A CFD model should be used to investigate whether or not a 1D model can capture the convection heat transfer with enough accuracy for design purposes. By using a 1D model, a reactor cavity which is open at the top and at the bottom is implied. In the theoretical model used in this thesis, the convection heat transfer is multiplied by 3 to predict the experimental result more accurately. This however can be a very conservative approach and limits the optimisation of the RCCS.

Appendices

Appendix A

Radiation view factor between two finite surfaces

As stated in Section 2.10.1, the calculation of the radiation view factor between any two surfaces requires the solution of the double area integral. With reference to figure A.1, Modest (2003) gives this double area integral as shown in equation (A.1).

$$F_{A_i - A_j} = \frac{1}{A_i} \int_{A_i} \int_{A_j} \frac{cos\theta_i cos\theta_j}{\pi s^2} dA_j dA_i \tag{A.1}$$

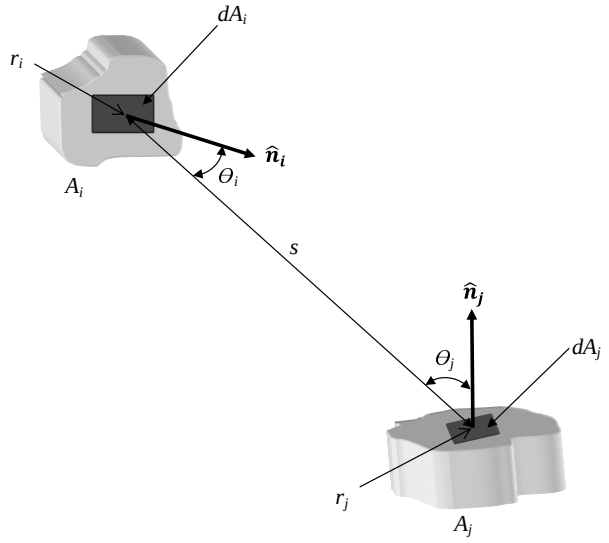

Figure A.1: Radiative exchange between two finite surfaces

To carry out the integrations in equation A.1, $cos\theta_i$, $cos\theta_j$ and s must be known in terms of a local coordinate system that describes the geometry of the two surfaces. A vector pointing from the origin of the global coordinate system to the origin of the local coordinate system on the surface is shown in figure A.2 and can be written as follows:

$$\mathbf{r} = x\hat{\mathbf{i}} + y\hat{\mathbf{j}} + z\hat{\mathbf{k}} \tag{A.2}$$

where $\hat{\mathbf{i}}$, $\hat{\mathbf{j}}$ and $\hat{\mathbf{k}}$ are unit vectors in the x-, y- and z-directions respectively.
The vector from dA_i to dA_j can be given by

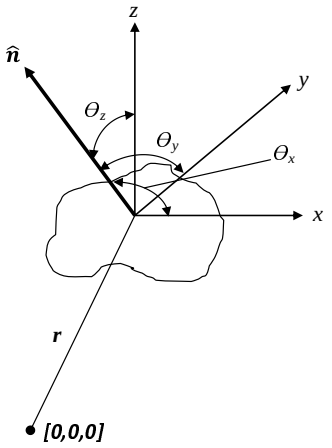

Figure A.2: Normal unit vector and directional cosines for a surface element

$$\mathbf{s}_{ij} = -\mathbf{s}_{ji} = (x_j - x_i)\,\hat{\mathbf{i}} + (y_j - y_i)\,\hat{\mathbf{j}} + (z_j - z_i)\,\hat{\mathbf{k}} \tag{A.3}$$

The length of the vector s can be calculated using

$$s^2 = (x_j - x_i)^2 + (y_j - y_i)^2 + (z_j - z_i)^2 \tag{A.4}$$

Assume that the surface normal vectors are also known in terms of the unit vectors $\hat{\mathbf{i}}$, $\hat{\mathbf{j}}$ and $\hat{\mathbf{k}}$, then, as in figure A.2, it follows that

$$\hat{\mathbf{n}} = l\hat{\mathbf{i}} + m\hat{\mathbf{j}} + n\hat{\mathbf{k}} \tag{A.5}$$

where l, m and n are the directional cosines for the unit vector $\hat{\mathbf{n}}$. Thus $l = \hat{\mathbf{n}}\cdot\hat{\mathbf{i}} = cos\theta_x$ is the cosine of the angle θ_x between $\hat{\mathbf{n}}$ and the x-axis. The cosines of θ_i and θ_j may be calculated as follows:

$$cos\theta_i = \frac{1}{s}\left[(x_j - x_i)\,l_i + (y_j - y_i)\,m_i + (z_j - z_i)\,n_i\right] \tag{A.6}$$

$$cos\theta_j = \frac{1}{s}\left[(x_i - x_j)\,l_j + (y_i - y_j)\,m_j + (z_i - z_j)\,n_j\right] \tag{A.7}$$

Equation A.1 can now be solved.

Appendix B

Background theory to the simplifying assumptions in the modelling of the closed loop thermosyphon heat pipe

B.1 The Boussinesq Approximation

In fluid dynamics, the Boussinesq approximation, named after French physicist Joseph Valentin Boussinesq, is used in the field of *buoyancy-driven flow*. It states that density differences are sufficiently small to be neglected, except where they appear in terms multiplied by g, the acceleration due to gravity. The essence of the Boussinesq approximation is that the difference in inertia is negligible but gravity is sufficiently strong to make the specific weight appreciably different between the two fluids. Sound waves are theoretically impossible and therefore neglected when the Boussinesq approximation is used since sound waves move via density variations that travel at the speed of sound throughout the medium.

The Boussinesq approximation's advantage arises when considering the flow analysis of two streams of water at different temperatures with densities ρ_1 and ρ_2. The Boussinesq approximation requires that only a single density ρ needs to be considered, because the difference in densities, $\triangle\rho = \rho_1$ - ρ_2, is negligible. Dimensional analysis shows that, under these circumstances, the only sensible way that acceleration due to gravity, g, should enter into the governing equations of motion is with a reduced gravity, g', term where

$$g' = g\frac{\rho_1 - \rho_2}{\rho} \tag{B.1.1}$$

where the density in the denominator may be either ρ_1 or ρ_2 without significantly affecting the result.

The mathematics of the flow analysis is therefore simpler because the density ratio, ρ_1/ρ_2, does not affect the flow velocity, because the Boussinesq approximation states that it may be assumed to be exactly one.

The Boussinesq approximation is used in the theoretical model of the thermosyphon to assume that density and viscosity variations are small and have an affect only in the body force term in the momentum balance equation (Agrawal *et al.*, 2007). The reason

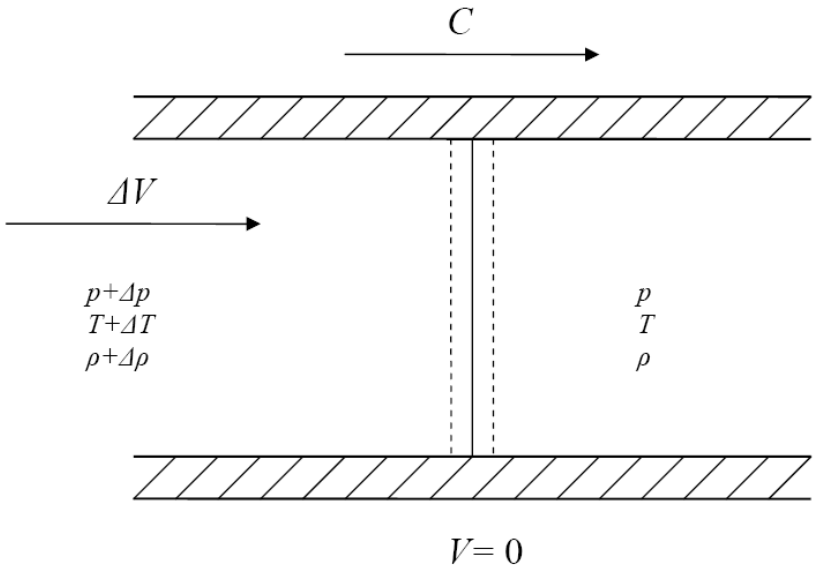

Figure B.1: Cross section of a fluid in a pipe

why density cannot be assumed to be a constant in the body force, or buoyancy, term of the momentum balance equation is because the buoyancy force that drives the flow in the thermosyphon varies with density and temperature. To determine the value of the density the Boussinesq approximation allows us to relate density with temperature with reasonable accuracy at a constant pressure with the following relation:

$$\rho = \rho_{\text{ref}} \left(1 + \beta \left(T - T_{\text{ref}}\right)\right) \tag{B.1.2}$$

B.2 The Speed of Sound

The speed of sound, denoted by a, of a fluid is the rate of propagation of pressure pulses, or sound waves, through the fluid (White, 2003).

The speed of sound is a thermodynamic property of the fluid. Consider a pulse, or pressure wave, that moves at velocity, C, towards a still standing cross section of a fluid as illustrated in figure B.1.

The pulse is leaving cross sections of the fluid behind in a new thermodynamic state and creates a velocity in the fluid. This velocity is much slower than the pulse. White (2003) determined the velocity to be given by

$$\triangle V = C \frac{\triangle \rho}{\rho + \Delta \rho} \tag{B.2.1}$$

This is the result of the continuity equation applied to a control volume as in figure B.1. From this equation it can be seen that the previous statement of how the created fluid velocity is much less than the pulse velocity is correct.

White (2003) also determines the change in density to be

$$\triangle \rho = \rho C \Delta V \tag{B.2.2}$$

If equation (B.2.1) and (B.2.2) are combined an expression for the wave velocity is formulated.

$$C^2 = \frac{\Delta p}{\Delta \rho}\left(1 + \frac{\Delta \rho}{\rho}\right) \tag{B.2.3}$$

If the Boussinesq approximation is used, $\Delta\rho \to 0$, this equation reduces to the speed of sound of a fluid given by

$$a^2 = \frac{\delta p}{\delta \rho} \tag{B.2.4}$$

Appendix C

Safety considerations for experiments

The experimental set-up requires high temperatures and 220 V electric power. It is therefore necessary to assess the safety hazards that the equipment can create and to set up a standardised procedure for working with the equipment in order to ensure safe operation. There are two safety hazards that the user of the experiment must be protected from. The first is the heat generated in the heating elements and the second is the electric current in the heating elements as well as in the water pump.

The heating elements use 6 kW electrical power in order to heat up to 300°C. The following start-up procedure lists all the switches that must be turned on in order for the heating elements to be on. This procedure must be reversed for shut-down.

- Switch on the 350 A mains.
- Switch on the secondary switch for the 350 A mains.
- Switch on the mains in the control box and close the door of the control box.
- Switch on the control box as shown in figure C.1.
- Switch on a set of heating elements.

Note that only one set of heating elements can be switched on at a time. If more than one set are switched on, the power would be cut. Only one of the five switches needs to be off for the heating elements to be off, but all five need to be switched off at every shut-down. This is to ensure that the heating elements can not be switched on by accident.

Table C.1 lists the main safety hazards and the protection against them that have been put in place in order to ensure safe operation of the experimental apparatus.

Figure C.1: Control box

Table C.1: Safety hazards and the protection against them

Safety Hazard	**Protection**
Electrical shock	All wires are insulated All equipment is earthed
Water on electrical equipment	All electrical equipment is inside closed boxes 1.8 m above the ground
Burning against elements	Workstation is 4 m from elements and behind concrete
Switching on 2 elements	Protected with circuit breaker
Water on electric pump	Connections are insulated and above floor

Appendix D

Standard sizes for Stainless Steel flatbar and pipes used in the optimisation of the RCCS radiation heat shield

The standard sizes for the flatbar used as fins in the heat shield and the sizes for the pipes for the closed loop thermosyphon heat pipes are given in this appendix. The catalogues are from the websites of the following two manufacturers:

Stalcor, a division of Kulungile Metals (Pty) Limited.
www.stalcor.co.za

NDE
www.nde.co.za

Flat bar

Grades: 304/304L/316/316L/3CR12

mm flat	kg/m
20 x 3	0,47
x 4	0,63
x 5	0,79
x 6	0,94
x 8	1,26
x 10	1,57
x 12	1,88
x 16	2,51
25 x 3	0,59
x 4	0,79
x 5	0,98
x 6	1,3
x 8	1,57
x 10	1,96
x 12	2,50
30 x 3	0,71
x 4	0,94
x 5	1,18
x 6	1,5
x 8	1,88
x 10	2,36
x 12	2,83
x 16	3,78
x 20	4,71
35 x 3	0,82
x 4	1,10
x 5	1,37
x 6	1,65
x 8	2,20
x 10	2,75
40 x 3	0,95
x 4	1,26
x 5	1,57
x 6	1,9
x 8	2,51
x 10	3,2
x 12	3,77
x 16	5,02
x 20	6,28
x 25	7,85
x 30	9,42

mm flat	kg/m
45 x 5	1,77
x 6	2,12
x 8	2,83
50 x 3	1,18
x 4	1,57
x 5	1,96
x 6	2,5
x 8	3,14
x 10	3,98
x 12	4,90
x 16	6,28
x 20	7,85
x 30	11,78
60 x 3	1,41
x 5	2,36
x 6	2,83
x 8	3,77
x 10	4,71
x 12	5,65
x 16	7,54
x 20	9,42
x 25	11,78
x 30	14,13
75 x 6	3,54
x 8	4,71
x 10	5,89
x 20	11,78
80 x 5	3,14
x 6	3,77
x 8	5,02
x 10	6,28
x 12	7,54
x 16	10,05
x 20	12,56
100 x 6	4,71
x 8	6,28
x 10	7,60
x 12	9,42
x 16	12,56
x 20	15,70
x 25	19,63

Hexagon bar

Grades: 303/316

mm hexagon	kg/m
6	0,38
8	0,44
10	0,68
11	0,82
12	0,98
13	1,15
14	1,33
17	1,96
19	2,45
22	3,29
24	3,92
27	4,96
30	6,12
32	6,96
36	8,81
38	9,82
41	11,43
46	14,39
50	17,00
55	20,57
60	24,48
65	28,72

Square bar

Grades: 316

mm square	kg/m
6	0,29
8	0,56
10	0,79
12	1,13
16	2,10
20	3,16
22	4,00
25	4,91
30	7,11
35	9,62
40	12,60
50	19,63
60	28,28
80	50,24
90	63,58
100	78,50

Angle

Grades: 304/316/3CR12

Dimension mm	kg/m
25 x 25 x 3	1,20
30 x 30 x 3	1,34
40 x 40 x 3	1,9
50 x 50 x 3	2,50
40 x 40 x 4	2,67
50 x 50 x 4	3,50
25 x 25 x 6	2,22
30 x 30 x 6	2,67
40 x 40 x 6	3,61
50 x 50 x 6	4,90
65 x 65 x 6	6,10
75 x 75 x 6	7,3.
80 x 80 x 8	10,46
50 x 50 x 10	7,09
75 x 75 x 10	11,10
100 x 100 x 10	15,00

Note: Flat bar and angle are generally hot rolled.

STALCOR

STAINLESS STEEL ALUMINIUM CORPORATION

STAINLESS STEEL NOMINAL BORE PIPES

Type: (AISI) 304/304L seamless/welded to ASTM A312 / ASME SA 312 hot rolled/cold drawn

Nominal Bore	Sch	Outside Diameter	Inside Diameter	Wall Thickness	kg/m	Product Code
8 mm	10S	13.72	10.42	1.65	.49	PIN1/0137/016/04
	40S	13.72	9.25	2.24	.64	PIN4/0137/022/04
	80S	13.72	7.67	3.02	.80	
10 mm	10S	17.15	13.84	1.65	.64	PIN1/0171/016/04
	40S	17.15	12.52	2.31	.85	PIN4/0171/023/04
	80S	17.15	10.74	3.20	1.10	
15 mm	10S	21.34	17.12	2.11	1.01	PWN1/0213/021/04
	40S	21.34	15.80	2.77	1.27	PWN4/0213/027/04
	80S	21.34				
20 mm	10S	26.67	22.45	2.11	1.29	PWN1/0266/021/04
	40S	26.67	20.93	2.87	1.71	PWN4/0266/028/04
	80S	26.67	18.85	3.91	2.19	
25 mm	10S	33.40	27.86	2.77	2.12	PWN1/0334/027/04
	40S	33.40	26.64	3.38	2.54	PWN4/0334/033/04
	80S	33.40	24.30	4.55	3.23	
32 mm	10S	42.16	36.62	2.77	2.76	PWN1/0421/027/04
	40S	42.16	35.04	3.56	3.45	PWN4/0421/035/04
	80S	42.16	32.46	4.85	4.47	
40 mm	10S	48.24	42.72	2.77	3.15	PWN1/0482/027/04
	40S	48.24	40.90	3.68	4.11	PWN4/0482/036/04
	80S	48.24	38.10	5.08	5.40	
50 mm	10S	60.33	54.79	2.77	3.99	PWN1/0603/027/04
	40S	60.33	52.51	3.91	5.29	PWN4/0603/039/04
	80S	60.33	49.25	5.54	7.47	
65 mm	10S	73.03	66.93	3.05	5.35	PWN1/0730/030/04
	40S	73.03	62.71	5.16	8.80	PWN4/0730/051/04
	80S	73.03	59.01	7.01	11.40	
80 mm	10S	88.90	82.80	3.05	6.56	PWN1/0889/030/04
	40S	88.90	77.92	5.49	11.48	PWN4/0889/054/04
	80S	88.90	73.66	7.62	15.25	
100 mm	10S	114.30	108.20	3.05	8.50	PWN1/1143/030/04
	40S	114.30	102.26	6.02	16.34	PWN4/1143/060/04
	80S	114.30	97.18	8.56	22.29	

STAINLESS STEEL NOMINAL BORE PIPES

Type: (AISI) 304/304L seamless/welded to ASTM A312 / ASME SA 312 hot rolled/cold drawn *cont'd...*

Nominal Bore	Sch	Outside Diameter	Inside Diameter	Wall Thickness	Mass/m	Product Code
125 mm	10S	141.30	134.50	3.40	11.75	PIN1/1413/034/04
	40S	141.30	128.20	6.55	22.12	PIN4/1413/065/04
	80S	141.30	122.26	9.52	30.92	
150 mm	10S	168.28	161.48	3.40	14.05	PIN1/1682/034/04
	40S	168.28	154.06	7.11	28.72	PIN4/1682/071/04
	80S	168.28	146.34	10.97	42.52	
200 mm	10S	219.08	211.56	3.76	20.30	PIN1/2190/037/04
	40S	219.08	202.72	8.18	43.27	PIN4/2190/081/04
	80S	219.08	193.68	12.70	64.57	
250 mm	10S	273.05	264.67	4.19	28.24	PIN1/2730/041/04
	40S	273.05	254.51	9.27	61.30	PIN4/2730/092/04
	80S	273.05	247.65	12.70	81.46	
300 mm	10S	323.85	314.71	4.57	36.58	PIN1/3238/045/04
	40S	323.85	304.81	9.52	75.09	PIN4/3238/095/04
	80S	323.85	298.45	12.70	97.36	
350 mm	10S	355.60	346.04	4.78	41.99	
	40S	355.60	336.54	9.53	82.58	
	80S	355.60	330.20	12.70	109.04	
400 mm	10S	406.40	396.84	4.78	48.07	
	40S	406.40	387.34	9.53	94.70	
	80S	406.40	381.00	12.70	125.20	
450 mm	10S	457.20	447.64	4.78	54.15	
	40S	457.20	438.14	9.53	106.83	
	80S	457.20	431.80	12.70	141.35	
500 mm	10S	508.00	496.92	5.54	69.70	
	40S	508.00	488.94	9.53	118.93	
	80S	508.00	482.60	12.70	157.51	
550 mm	10S	558.80	547.72	5.54	76.75	
	40S	558.80	539.74	9.53	131.07	
	80S	558.80	533.40	12.70	173.66	
600 mm	10S	609.60	596.90	6.35	95.92	
	40S	609.60	590.54	9.53	143.20	
	80S	609.60	584.20	12.70	189.82	

Appendix E

Sample Input File for the Theoretical Model

```
1         '    DTIME         ' time step
1000000   '    TSCRAM        ' time when shutdown starts
1000000   '    TSTOP         ' total simulation time
1000      '    PSSTEP        ' print screen step
10        '    PDSTEP        ' print data step
1         '    SLIP          ' SLIP=ug/ul for the homogeneous flow model
2         '    N1            ' Bottom pipe number of elements
12        '    N2            ' Hot pipe number of elements
2         '    N3            ' Top pipe number of elements
12        '    N4            ' Cold pipe number of elements
40        '    L1            ' Length of bottom pipe
12        '    L2            ' Length of hot pipe
40        '    L3            ' Length of top pipe
12        '    L4            ' Length of cold pipe
0.02667   '    Di1           ' Inside diameter of bottom pipe
0.02667   '    Di2           ' Inside diameter of hot pipe
0.02667   '    Di3           ' Inside diameter of top pipe
0.02667   '    Di4           ' Inside diameter of cold pipe
0.4       '    PLk           ' Liuid only pressure loss coefficient
7800      '    Rsteel        ' Density of RPV steel
13        '    zextank       ' Height of expansion tank water level
101000    '    Patm_tank     ' Atmospheric pressure above tank
0.1       '    dextankpipe   ' Pipe diameter of Expansion tank
9         '    Lextankpipe   ' Length of tank pipe Expansion tank
2         '    Lextank       ' Expansion Tank lenght
2         '    Wextank       ' Expansion Tank width
2         '    Dextank       ' Expansion Tank depth
.8        '    ETAfin        ' fin efficiency
9.5       '    Dfin          ' fin diameter
0.01      '    tfin          ' fin thickness
16        '    kfin          ' fin conductivity
477       '    Cfin          ' fin specific heat
7900      '    Rfin          ' fin density
0.8       '    EMISf         ' Emissivity of fin
```

```
30       '    Dtank        ' diameter of dam
0.9      '    ecw          ' Emissivity of dam water
1000     '    ROUcw        ' Density of dam water
4266     '    Cvtank       ' specific heat of dam water
2300000  '    hfgtank      ' latent heat of evaporation J/kg of dam water
14       '    Tfeed        ' feed water temperature of dam water
0.85     '    EMISr        ' Emissivity of reactor vessel
6.56     '    Dr           ' outside diameter of reactor vessel
0.18     '    rwt          ' thickness of reactor vessel
477      '    Cvr          ' specific heat of reactor vessel
12       '    NJcs         ' Number of horizontal elements in the concrete
9.86     '    Dcs          ' Inside Diameter of concrete structure
0.9      '    CSthickness  ' Thickness of concrete structure in meters
2400     '    ROUcs        ' Density of concrete structure
.8       '    kcs          ' Thermal conductivity of concrete structure
1100     '    ccs          ' Thermal capasity of concrete structure
0.77     '    ecs          ' Emissivity of concrete
25       '    Tday         ' Ambient temperature during day
16       '    Tnight       ' Ambient temperature during night
101325   '    Patm         ' Atmospheric pressure
10       '    Vwind        ' Wind velocity km/h
0.5      '    RH           ' Relative humidity
20       '    Ttbegin      ' Initial dam temperature
20       '    Tbegin       ' Initial thermosyphon temperature
470      '    Trbegin      ' Initial reactor vessel temperature
1100     '    Tcorebegin   ' Initial reactor core temperature
20       '    Tabegin      ' Initial temp of air between the RPV and the HS
20       '    Tfbegin      ' Initial fin temperature
20       '    Tcsbegin     ' Initial concrete temperature
20       '    Tafcsbegin   ' Initial temp of air between the HS and the concrete
1000     '    Rcore        ' Density of reactor core
1000     '    Cvcore       ' Thermal capasity of reactor core
1        '    Ffcs         ' Radiation view factor from HS to concrete
1        '    Frf          ' Radiation view factor from RPV to HS
448      '    Nhp          ' Number of heat pipe loops in the reactor cavity
1900000  '    PowerHP      ' Steady state heat into thermosyphons
```

Appendix F

Temperatures of the Heat Shield and Concrete inside surface for different sized fins and heat pipes

The maximum temperatures of the radiation heat shield and the inside surface of the concrete citadel are given in the following tables for heat pipes with inside diameters varying from 18.85 mm to 146.33 mm and fins with widths varying from 20 mm to 100 mm. These values are given for five different sized cooling dams. The diameter of the cooling dams is varied from 20 m to 60 m. The height of the cooling dam is fixed at 12 m. This is the same height as the closed loop thermosyphon heat pipes. The wind speed is 1 m/s, the day time ambient temperature is 25 °C and the night time temperature 16 °C. The relative humidity is 0.5. The feed water for the cooling dam to replace the evaporated water is assumed to be at 14 °C.

Table F.1: Temperatures of the Heat Shield and the Concrete surface for thermosyphon heat pipe inside diameters of 18.85 mm to 62.72 mm with a 20 m diameter cooling dam.

	ID (mm)											
Wfin	18.85		24.3		32.46		38.1		49.25		62.72	
	T_{HS_i}	T_{Con_i}	T_{HS_i}	T_{Con_i}	T_{HS_i}	T_{Con_i}	T_{HS_i}	T_{Con_i}	T_{HS_i}	T_{Con_i}	T_{HS_i}	T_{Con_i}
20	106.6	97.0	100.6	91.3	95.6	86.5	93.6	84.6	91.0	82.2	89.1	80.3
25	109.5	99.9	102.8	93.4	97.3	88.1	95.0	85.9	92.1	83.2	90.0	81.1
30	111.2	101.7	104.9	95.4	98.8	89.6	96.3	87.2	93.2	84.2	90.9	82.0
35	111.3	101.9	106.9	97.3	100.3	91.0	97.6	88.4	94.2	85.2	91.6	82.7
40	111.4	102.1	108.8	99.2	101.8	92.4	98.8	89.6	95.2	86.1	92.5	83.5
45	111.5	102.3	110.6	101.0	103.2	93.7	100.0	90.8	96.1	87.0	93.3	84.3
50	111.5	102.4	112.4	102.7	104.5	95.1	101.2	91.9	97.1	87.9	94.1	85.0
60	111.8	102.7	112.8	103.4	107.1	97.6	103.5	94.1	98.8	89.6	95.5	86.4
75	112.1	103.2	113.0	103.7	110.8	101.1	106.6	97.1	101.4	92.1	97.6	88.4
80	112.3	103.4	113.0	103.8	111.9	102.2	107.7	98.1	102.3	93.0	98.3	89.1
100	113.4	104.5	113.2	104.1	114.8	105.2	111.6	101.9	105.4	95.9	100.9	91.6

Table F.2: Temperatures of the Heat Shield and the Concrete surface for thermosyphon heat pipe inside diameters of 73.66 mm to 146.33 mm with a 20 m diameter cooling dam.

	ID (mm)									
Wfin	73.66		90.12		102.26		128.2		146.33	
	T_{HS_i}	T_{Con_i}	T_{HS_i}	T_{Con_i}	T_{HS_i}	T_{Con_i}	T_{HS_i}	T_{Con_i}	T_{HS_i}	T_{Con_i}
20	88.5	79.7	87.3	78.5	86.8	78.1	86.1	77.4	86.2	77.5
25	89.3	80.5	87.9	79.1	87.4	78.6	86.6	77.9	86.6	77.8
30	90.0	81.2	88.5	79.7	87.9	79.2	87.1	78.3	87.0	78.2
35	90.7	81.8	89.1	80.3	88.5	79.7	87.5	78.8	87.4	78.7
40	91.4	82.5	89.7	80.9	89.0	80.2	88.0	79.2	87.8	79.0
45	92.1	83.1	90.3	81.4	89.5	80.7	88.4	79.6	88.2	79.3
50	92.8	83.8	90.9	82.0	90.1	81.2	88.8	80.0	88.6	79.8
60	94.0	85.0	91.9	83.0	91.1	82.2	89.7	80.8	89.3	80.4
75	95.9	86.8	93.5	84.5	92.5	83.5	90.9	82.0	90.4	81.5
80	96.5	87.3	94.1	85.0	92.9	83.9	91.3	82.3	90.7	81.8
100	98.8	89.6	96.0	86.9	94.7	85.7	92.9	83.8	92.1	83.1

Table F.3: Temperatures of the Heat Shield and the Concrete surface for thermosyphon heat pipe inside diameters of 18.85 mm to 62.72 mm with a 30 m diameter cooling dam.

	ID (mm)											
Wfin	18.85		24.3		32.46		38.1		49.25		62.72	
	T_{HS_i}	T_{Con_i}	T_{HS_i}	T_{Con_i}	T_{HS_i}	T_{Con_i}	T_{HS_i}	T_{Con_i}	T_{HS_i}	T_{Con_i}	T_{HS_i}	T_{Con_i}
20	92.2	83.0	85.9	77.1	80.7	72.2	78.5	70.1	75.8	67.6	73.8	65.6
25	95.3	86.0	88.3	79.3	82.4	73.8	80.0	71.5	77.0	68.7	74.7	66.5
30	98.1	88.7	90.4	81.4	84.1	75.4	81.5	72.9	78.2	69.8	75.7	67.4
35	100.8	91.3	92.6	83.4	85.7	76.9	82.9	74.2	79.3	70.8	76.5	68.2
40	103.4	93.8	94.6	85.3	87.3	78.4	84.2	75.4	80.3	71.8	77.4	69.1
45	106.0	96.2	96.5	87.2	88.7	79.7	85.5	76.7	81.3	72.8	78.3	69.9
50	108.3	98.5	98.4	88.9	90.2	81.1	86.8	77.9	82.4	73.8	79.2	70.7
60	113.9	103.6	101.9	92.3	92.9	83.7	89.2	80.2	84.3	75.5	80.7	72.2
75	114.6	105.3	106.9	97.1	96.8	87.4	92.4	83.3	87.1	78.2	83.0	74.3
80	114.7	105.5	108.6	98.7	97.9	88.5	93.6	84.4	88.0	79.1	83.8	75.1
100	115.2	106.1	114.5	104.4	102.7	93.0	97.7	88.3	91.2	82.1	86.6	77.7

Table F.4: Temperatures of the Heat Shield and the Concrete surface for thermosyphon heat pipe inside diameters of 73.66 mm to 146.33 mm with a 30 m diameter cooling dam.

	ID (mm)									
Wfin	73.66		90.12		102.26		128.2		146.33	
	T_{HS_i}	T_{Con_i}	T_{HS_i}	T_{Con_i}	T_{HS_i}	T_{Con_i}	T_{HS_i}	T_{Con_i}	T_{HS_i}	T_{Con_i}
20	73.1	65.0	71.8	63.8	71.3	63.3	70.5	62.6	70.6	62.7
25	74.0	65.8	72.5	64.4	71.9	63.9	71.1	63.1	71.0	63.1
30	74.8	66.6	73.1	65.1	72.5	64.5	71.6	63.6	71.5	63.5
35	75.6	67.3	73.8	65.7	73.1	65.0	72.1	64.1	72.0	64.0
40	76.3	68.0	74.5	66.3	73.7	65.6	72.6	64.5	72.4	64.4
45	77.1	68.7	75.1	66.9	74.3	66.1	73.1	65.0	72.8	64.7
50	77.8	69.4	75.8	67.5	74.9	66.7	73.5	65.4	73.3	65.2
60	79.2	70.7	76.9	68.6	76.0	67.7	74.5	66.3	74.0	65.9
75	81.2	72.6	78.7	70.2	77.5	69.2	75.9	67.6	75.3	67.0
80	81.8	73.2	79.3	70.8	78.0	69.7	76.3	68.0	75.7	67.4
100	84.4	75.6	81.4	72.8	80.0	71.5	78.0	69.6	77.2	68.9

Table F.5: Temperatures of the Heat Shield and the Concrete surface for thermosyphon heat pipe inside diameters of 18.85 mm to 62.72 mm with a 40 m diameter cooling dam.

	ID (mm)											
Wfin	18.85		24.3		32.46		38.1		49.25		62.72	
	T_{HS_i}	T_{Con_i}	T_{HS_i}	T_{Con_i}	T_{HS_i}	T_{Con_i}	T_{HS_i}	T_{Con_i}	T_{HS_i}	T_{Con_i}	T_{HS_i}	T_{Con_i}
20	82.8	74.4	76.4	68.3	71.0	63.3	68.7	61.2	65.9	58.7	63.8	56.7
25	86.0	77.4	78.8	70.6	72.8	65.0	70.3	62.7	67.1	59.8	64.8	57.6
30	89.0	80.2	81.0	72.7	74.5	66.6	71.8	64.1	68.4	61.0	65.8	58.6
35	91.7	82.8	83.2	74.7	76.2	68.2	73.3	65.5	69.6	62.0	66.7	59.5
40	94.4	85.4	85.3	76.7	77.8	69.7	74.6	66.7	70.7	63.1	67.7	60.3
45	97.0	87.8	87.3	78.6	79.3	71.1	76.0	68.0	71.7	64.1	68.6	61.2
50	99.5	90.1	89.2	80.4	80.8	72.5	77.3	69.2	72.8	65.1	69.5	62.0
60	104.3	94.8	92.8	83.8	83.6	75.1	79.8	71.6	74.8	66.9	71.1	63.5
75	110.8	101.0	97.9	88.7	87.6	78.9	83.2	74.7	77.7	69.6	73.5	65.8
80	112.8	103.0	99.6	90.3	88.8	80.0	84.4	75.8	78.7	70.5	74.3	66.5
100	116.4	107.1	105.7	96.1	93.6	84.6	88.5	79.8	82.0	73.6	77.3	69.3

Table F.6: Temperatures of the Heat Shield and the Concrete surface for thermosyphon heat pipe inside diameters of 73.66 mm to 146.33 mm with a 40 m diameter cooling dam.

	ID (mm)									
Wfin	73.66		90.12		102.26		128.2		146.33	
	T_{HS_i}	T_{Con_i}	T_{HS_i}	T_{Con_i}	T_{HS_i}	T_{Con_i}	T_{HS_i}	T_{Con_i}	T_{HS_i}	T_{Con_i}
20	63.1	56.1	61.7	54.8	61.2	54.4	60.4	53.7	60.6	53.8
25	64.0	57.0	62.5	55.5	61.9	55.0	61.0	54.2	61.0	54.2
30	64.9	57.8	63.2	56.2	62.6	55.6	61.6	54.8	61.5	54.7
35	65.7	58.5	63.9	56.9	63.2	56.2	62.2	55.3	62.1	55.2
40	66.5	59.3	64.7	57.6	63.8	56.8	62.7	55.7	62.5	55.6
45	67.3	60.0	65.3	58.2	64.5	57.4	63.2	56.2	62.9	56.0
50	68.1	60.7	66.0	58.8	65.1	58.0	63.7	56.7	63.5	56.5
60	69.6	62.1	67.3	59.9	66.3	59.1	64.7	57.6	64.3	57.2
75	71.7	64.1	69.1	61.6	67.9	60.6	66.2	59.0	65.6	58.4
80	72.4	64.7	69.7	62.2	68.5	61.1	66.6	59.4	66.0	58.8
100	75.0	67.1	72.0	64.3	70.6	63.0	68.5	61.1	67.7	60.3

Table F.7: Temperatures of the Heat Shield and the Concrete surface for thermosyphon heat pipe inside diameters of 18.85 mm to 62.72 mm with a 50 m diameter cooling dam.

	ID (mm)											
Wfin	18.85		24.3		32.46		38.1		49.25		62.72	
	T_{HS_i}	T_{Con_i}	T_{HS_i}	T_{Con_i}	T_{HS_i}	T_{Con_i}	T_{HS_i}	T_{Con_i}	T_{HS_i}	T_{Con_i}	T_{HS_i}	T_{Con_i}
20	77.1	69.3	70.5	63.2	65.1	58.2	62.8	56.1	60.0	53.6	57.9	51.7
25	80.4	72.3	73.0	65.5	66.9	59.9	64.4	57.6	61.3	54.8	58.9	52.6
30	83.4	75.2	75.3	67.6	68.7	61.5	66.0	59.0	62.6	55.9	60.0	53.6
35	86.2	77.8	77.5	69.7	70.4	63.1	67.5	60.4	63.8	57.0	61.0	54.5
40	89.0	80.4	79.7	71.7	72.1	64.6	68.9	61.7	64.9	58.1	61.9	55.4
45	91.6	82.9	81.7	73.6	73.6	66.0	70.2	62.9	66.0	59.1	62.9	56.2
50	94.1	85.2	83.6	75.4	75.1	67.4	71.6	64.2	67.1	60.1	63.8	57.1
60	99.0	89.9	87.3	78.8	78.0	70.1	74.1	66.6	69.1	61.9	65.5	58.6
75	105.5	96.2	92.5	83.7	82.1	73.9	77.6	69.7	72.1	64.7	67.9	60.9
80	107.6	98.2	94.2	85.4	83.2	75.0	78.8	70.9	73.1	65.6	68.8	61.6
100	115.5	105.8	100.3	91.2	88.2	79.7	83.1	74.9	76.5	68.7	71.8	64.4

Table F.8: Temperatures of the Heat Shield and the Concrete surface for thermosyphon heat pipe inside diameters of 73.66 mm to 146.33 mm with a 50 m diameter cooling dam.

	ID (mm)									
Wfin	73.66		90.12		102.26		128.2		146.33	
	T_{HS_i}	T_{Con_i}	T_{HS_i}	T_{Con_i}	T_{HS_i}	T_{Con_i}	T_{HS_i}	T_{Con_i}	T_{HS_i}	T_{Con_i}
20	57.3	51.1	55.9	49.9	55.4	49.5	54.6	48.8	54.8	49.0
25	58.2	52.0	56.7	50.6	56.1	50.1	55.3	49.3	55.3	49.4
30	59.1	52.8	57.4	51.3	56.8	50.7	55.9	49.9	55.8	49.8
35	60.0	53.6	58.2	52.0	57.4	51.3	56.4	50.4	56.4	50.3
40	60.8	54.3	58.9	52.7	58.1	51.9	56.9	50.9	56.8	50.8
45	61.6	55.1	59.6	53.3	58.8	52.5	57.5	51.4	57.3	51.2
50	62.4	55.8	60.3	53.9	59.4	53.1	58.0	51.8	57.8	51.7
60	63.9	57.2	61.6	55.1	60.6	54.2	59.1	52.8	58.7	52.4
75	66.1	59.2	63.5	56.8	62.3	55.8	60.6	54.2	60.0	53.7
80	66.8	59.8	64.2	57.4	62.9	56.3	61.0	54.6	60.5	54.1
100	69.5	62.3	66.5	59.6	65.1	58.3	63.0	56.4	62.2	55.6

Table F.9: Temperatures of the Heat Shield and the Concrete surface for thermosyphon heat pipe inside diameters of 18.85 mm to 62.72 mm with a 60 m diameter cooling dam.

	ID (mm)											
Wfin	18.85		24.3		32.46		38.1		49.25		62.72	
	T_{HS_i}	T_{Con_i}	T_{HS_i}	T_{Con_i}	T_{HS_i}	T_{Con_i}	T_{HS_i}	T_{Con_i}	T_{HS_i}	T_{Con_i}	T_{HS_i}	T_{Con_i}
20	73.6	66.2	66.9	60.1	61.4	55.1	59.2	53.1	56.4	50.6	54.3	48.7
25	76.9	69.3	69.4	62.4	63.3	56.8	60.8	54.5	57.7	51.8	55.4	49.7
30	80.0	72.2	71.8	64.6	65.1	58.5	62.4	56.0	59.0	52.9	56.5	50.7
35	82.8	74.8	74.0	66.6	66.9	60.1	63.9	57.4	60.2	54.0	57.4	51.5
40	85.6	77.4	76.2	68.7	68.5	61.6	65.3	58.7	61.4	55.1	58.5	52.4
45	88.3	79.9	78.2	70.5	70.1	63.0	66.7	59.9	62.5	56.1	59.4	53.3
50	90.8	82.3	80.2	72.4	71.6	64.4	68.1	61.2	63.7	57.1	60.4	54.2
60	95.8	87.0	83.9	75.9	74.6	67.2	70.7	63.6	65.7	59.0	62.1	55.7
75	102.4	93.3	89.2	80.8	78.7	71.0	74.2	66.8	68.7	61.8	64.6	58.0
80	104.5	95.3	90.9	82.5	79.9	72.1	75.4	68.0	69.7	62.7	65.4	58.8
100	112.4	102.9	97.1	88.3	84.9	76.7	79.7	72.0	73.1	65.9	68.5	61.6

Table F.10: Temperatures of the Heat Shield and the Concrete surface for thermosyphon heat pipe inside diameters of 73.66 mm to 146.33 mm with a 60 m diameter cooling dam.

	ID (mm)									
Wfin	73.66		90.12		102.26		128.2		146.33	
	T_{HS_i}	T_{Con_i}	T_{HS_i}	T_{Con_i}	T_{HS_i}	T_{Con_i}	T_{HS_i}	T_{Con_i}	T_{HS_i}	T_{Con_i}
20	53.7	48.2	52.3	47.0	51.9	46.6	51.2	45.9	51.4	46.1
25	54.7	49.1	53.2	47.7	52.6	47.2	51.8	46.5	51.9	46.6
30	55.6	49.9	53.9	48.4	53.3	47.8	52.4	47.0	52.4	47.0
35	56.5	50.7	54.7	49.1	54.0	48.5	53.0	47.6	53.0	47.5
40	57.3	51.4	55.5	49.8	54.7	49.0	53.5	48.0	53.5	48.0
45	58.2	52.2	56.2	50.4	55.4	49.7	54.1	48.6	53.9	48.4
50	59.0	52.9	56.9	51.0	56.0	50.3	54.6	49.0	54.5	48.9
60	60.5	54.3	58.2	52.2	57.3	51.4	55.7	50.0	55.3	49.7
75	62.8	56.4	60.2	54.0	59.0	53.0	57.3	51.4	56.7	50.9
80	63.5	57.0	60.8	54.6	59.6	53.5	57.7	51.8	57.2	51.3
100	66.2	59.5	63.2	56.8	61.8	55.5	59.7	53.6	58.9	52.9

Appendix G

Temperatures of the Heat Shield and Concrete inside surface for different sized fins and heat pipes under vacuum conditions

The maximum temperatures of the heat shield and the inside surface of the concrete citadel are given in the following tables for heat pipes with inside diameters varying from 18.85 mm to 146.33 mm and fins with widths varying from 20 mm to 100 mm for when the closed loop thermosyphon heat pipes are under vacuum pressure. The vacuum pressure is 5 kPa. The temperature values are given for three different sized cooling dams. The diameters of the cooling dams are 60 m, 80 m and 100 m. The wind speed is 1 m/s, the day time ambient temperature is 25 °C and the night time temperature 16 °C. The relative humidity is 0.5. The feed water for the cooling dam to replace the evaporated water is assumed to be at 14 °C.

Table G.1: Temperatures of the Heat Shield and the Concrete surface for thermosyphon heat pipe inside diameters of 18.85 mm to 62.72 mm with a 60 m diameter cooling dam under vacuum conditions.

	ID (mm)											
Wfin	18.85		24.3		32.46		38.1		49.25		62.72	
	T_{HS_i}	T_{Con_i}	T_{HS_i}	T_{Con_i}	T_{HS_i}	T_{Con_i}	T_{HS_i}	T_{Con_i}	T_{HS_i}	T_{Con_i}	T_{HS_i}	T_{Con_i}
20			66.0	59.4	61.4	55.1	59.2	53.1	56.4	50.6	54.3	48.7
25			67.7	61.1	63.7	57.0	60.8	54.5	57.7	51.8	55.4	49.7
30					65.0	58.4	62.4	56.0	59.0	52.9	56.5	50.7
35					66.2	59.6	63.9	57.4	60.2	54.0	57.4	51.5
40					67.3	60.7	65.4	58.7	61.4	55.1	58.5	52.4
45					68.3	61.7	66.3	59.7	62.5	56.1	59.4	53.3
50							67.2	60.6	63.7	57.1	60.4	54.2
60							68.8	62.2	66.0	59.1	62.1	55.7
75									67.9	61.3	64.6	58.0
80									68.5	61.9	65.4	58.8
100									70.6	63.9	68.3	61.6

Table G.2: Temperatures of the Heat Shield and the Concrete surface for thermosyphon heat pipe inside diameters of 73.66 mm to 146.33 mm with a 60 m diameter cooling dam under vacuum conditions.

	ID (mm)									
Wfin	73.66		90.12		102.26		128.2		146.33	
	T_{HS_i}	T_{Con_i}	T_{HS_i}	T_{Con_i}	T_{HS_i}	T_{Con_i}	T_{HS_i}	T_{Con_i}	T_{HS_i}	T_{Con_i}
20	53.7	48.2	52.3	47.0	51.9	46.6	51.2	45.9	51.4	46.1
25	54.7	49.1	53.2	47.7	52.6	47.2	51.8	46.5	51.9	46.6
30	55.6	49.9	53.9	48.4	53.3	47.8	52.4	47.0	52.4	47.0
35	56.5	50.7	54.7	49.1	54.0	48.5	53.0	47.6	53.0	47.5
40	57.3	51.4	55.5	49.8	54.7	49.0	53.5	48.0	53.5	48.0
45	58.2	52.2	56.2	50.4	55.4	49.7	54.1	48.6	53.9	48.4
50	59.0	52.9	56.9	51.0	56.0	50.3	54.6	49.0	54.5	48.9
60	60.5	54.3	58.2	52.2	57.3	51.4	55.7	50.0	55.3	49.7
75	62.8	56.4	60.2	54.0	59.0	53.0	57.3	51.4	56.7	50.9
80	63.5	57.0	60.8	54.6	59.6	53.5	57.7	51.8	57.2	51.3
100	66.2	59.5	63.2	56.8	61.8	55.5	59.7	53.6	58.9	52.9

Table G.3: Temperatures of the Heat Shield and the Concrete surface for thermosyphon heat pipe inside diameters of 18.85 mm to 62.72 mm with a 80 m diameter cooling dam under vacuum conditions.

	ID (mm)											
Wfin	18.85		24.3		32.46		38.1		49.25		62.72	
	T_{HS_i}	T_{Con_i}	T_{HS_i}	T_{Con_i}	T_{HS_i}	T_{Con_i}	T_{HS_i}	T_{Con_i}	T_{HS_i}	T_{Con_i}	T_{HS_i}	T_{Con_i}
20			63.6	57.2	57.5	51.8	55.3	49.8	52.6	47.4	50.5	45.6
25			65.6	59.2	59.5	53.6	57.0	51.3	53.9	48.6	51.6	46.5
30					61.3	55.3	58.6	52.8	55.2	49.8	52.7	47.5
35					63.1	56.9	60.1	54.2	56.4	50.9	53.7	48.4
40					65.3	58.7	61.6	55.5	57.6	51.9	54.7	49.3
45					66.4	60.0	63.0	56.8	58.8	53.0	55.7	50.2
50							64.4	58.1	60.0	54.0	56.7	51.1
60							67.2	60.6	62.0	55.9	58.4	52.7
75									65.1	58.7	61.0	55.0
80									66.1	59.7	61.8	55.8
100									69.4	62.8	65.0	58.6

Table G.4: Temperatures of the Heat Shield and the Concrete surface for thermosyphon heat pipe inside diameters of 73.66 mm to 146.33 mm with a 80 m diameter cooling dam under vacuum conditions.

	ID (mm)									
Wfin	73.66		90.12		102.26		128.2		146.33	
	T_{HS_i}	T_{Con_i}	T_{HS_i}	T_{Con_i}	T_{HS_i}	T_{Con_i}	T_{HS_i}	T_{Con_i}	T_{HS_i}	T_{Con_i}
20	50.0	45.1	48.6	43.9	48.2	43.6	47.5	43.0	47.8	43.2
25	50.9	46.0	49.4	44.7	48.9	44.2	48.2	43.5	48.3	43.7
30	51.9	46.8	50.2	45.4	49.7	44.9	48.8	44.1	48.8	44.1
35	52.8	47.6	51.0	46.1	50.4	45.5	49.4	44.6	49.4	44.7
40	53.6	48.4	51.8	46.8	51.0	46.1	50.0	45.1	49.9	45.1
45	54.5	49.2	52.5	47.4	51.7	46.7	50.6	45.7	50.4	45.5
50	55.4	49.9	53.3	48.1	52.4	47.3	51.1	46.1	51.0	46.0
60	56.9	51.3	54.6	49.3	53.7	48.5	52.2	47.1	51.9	46.8
75	59.2	53.4	56.6	51.1	55.5	50.1	53.8	48.6	53.3	48.1
80	59.9	54.0	57.3	51.7	56.1	50.6	54.3	49.0	53.8	48.5
100	62.8	56.6	59.8	53.9	58.3	52.6	56.3	50.8	55.6	50.1

Table G.5: Temperatures of the Heat Shield and the Concrete surface for thermosyphon heat pipe inside diameters of 18.85 mm to 62.72 mm with a 100 m diameter cooling dam under vacuum conditions.

	ID (mm)											
Wfin	18.85		24.3		32.46		38.1		49.25		62.72	
	T_{HS_i}	T_{Con_i}	T_{HS_i}	T_{Con_i}	T_{HS_i}	T_{Con_i}	T_{HS_i}	T_{Con_i}	T_{HS_i}	T_{Con_i}	T_{HS_i}	T_{Con_i}
20			67.7	61.0	64.3	57.7	53.4	48.3	50.7	45.9	48.6	44.1
25			67.5	59.4	65.5	58.9	55.1	49.8	52.0	47.1	49.7	45.0
30					66.6	60.0	56.7	51.2	53.4	48.2	50.9	46.1
35					61.3	55.3	58.3	52.7	54.6	49.4	51.9	46.9
40					63.0	56.9	59.7	54.0	55.8	50.4	52.9	47.9
45					64.6	58.4	61.2	55.3	57.0	51.5	53.9	48.8
50							62.6	56.6	58.2	52.6	54.9	49.7
60							65.3	59.0	60.3	54.5	56.7	51.2
75									63.4	57.3	59.3	53.6
80									64.4	58.2	60.1	54.3
100									68.0	61.5	63.3	57.2

Table G.6: Temperatures of the Heat Shield and the Concrete surface for thermosyphon heat pipe inside diameters of 73.66 mm to 146.33 mm with a 100 m diameter cooling dam under vacuum conditions.

	ID (mm)									
Wfin	73.66		90.12		102.26		128.2		146.33	
	T_{HS_i}	T_{Con_i}	T_{HS_i}	T_{Con_i}	T_{HS_i}	T_{Con_i}	T_{HS_i}	T_{Con_i}	T_{HS_i}	T_{Con_i}
20	48.1	43.6	46.8	42.5	46.4	42.1	45.8	41.6	46.1	41.8
25	49.1	44.5	47.6	43.2	47.1	42.7	46.4	42.1	46.6	42.3
30	50.1	45.4	48.5	43.9	47.9	43.4	47.1	42.7	47.1	42.8
35	51.0	46.2	49.3	44.6	48.6	44.1	47.7	43.3	47.7	43.3
40	51.9	46.9	50.1	45.4	49.3	44.6	48.2	43.7	48.2	43.7
45	52.7	47.7	50.8	46.0	50.0	45.3	48.8	44.3	48.7	44.1
50	53.6	48.5	51.5	46.7	50.7	45.9	49.4	44.7	49.3	44.7
60	55.2	49.9	52.9	47.9	52.0	47.1	50.6	45.8	50.2	45.5
75	57.5	52.0	54.9	49.7	53.8	48.7	52.2	47.2	51.7	46.8
80	58.2	52.6	55.6	50.3	54.4	49.2	52.6	47.6	52.1	47.2
100	61.1	55.2	58.1	52.5	56.7	51.3	54.7	49.5	53.9	48.8

List of References

Agrawal, R., West, D. and Balakotaiah, V. (2007). Modeling and analysis of local hot spot formation in down-flow adiabatic packed-bed reactors. *Chemical Engineering Science*, vol. 62, no. 18-20, pp. 4926–4943.

Ambrosini, W. (2008). Lesson learned from the adoption of numerical techniques in the analysis of nuclear reactor thermal-hydraulic phenomena. *Progress in Nuclear Energy*, vol. 50, pp. 866–876.

Ambrosini, W. and Ferreri, J. (2000). Stability analysis of single-phase thermosyphon loops by finite-difference numerical methods. *Nuclear Engineering and Design*, vol. 201, no. 1, pp. 11–24.

Ball, S. (2004 22-24 September). Sensitivity Studies of Modular High-Temperature Gas-Cooled Reactor (MHTGR) Postulated Accidents. 2nd International Topical Meeting on HIGH TEMPERATURE REACTOR TECHNOLOGY, Beijing, China.

Barnert, H. and Singh, J. (1996 13-15 November). Studies on self-acting heat removal systems on the basis of partial boiling of water for steel pressure vessel cooling of modular HTRs. In: *Technical committee meeting on high temperature gas cooled reactor technology development*, IAEA-TECDOC-988, pp. 293–304. International Atomic Energy Agency, Johannesburg, South Africa.

Bhat, N.R., Kansal, A.K., Kamble, M.T. and Andhansare, M.G. (not dated). Cooling of concrete structure in advanced heavy water reactor. *Reactor Engineering Division, Bhabha Atomic Research Centre, Trombay, Mumbai, INDIA.*

Çengel, Y. and Boles, M. (2002). *Thermodynamics: An Engineering Approach.* Boston; Burr Ridge, IL: McGraw-Hill.

Çengel, Y. (2003). *Heat Transfer: A Practical Approach.* McGraw-Hill.

Chinnery, D.N.W. (1973). Heating requirements of swimming pools and the feasibility of heating domestic pools with solar energy. *Council for Scientific and Industrial Research (CSIR), Report number R/BOU 472.*

Costa, V.A.F. (2002). Laminar natural convection in differentially heated rectangular enclosures with vertical diffusive walls. *Int. J. Heat Mass Transfer*, vol. 45, pp. 4217–4225.

Dams, M. (1996). Simulation of the pebble bed modular reactor natural air convection passive heat removal system. *Integrators of System Technology Ltd, Waterkloof, South Africa.*

de Groot, S., Bakker, K., van Heek, A.I. and Fütterer, M.A. (2008). Modelling of the HFR-EU1BIS experiment and thermomechanical evaluation. *Nuclear Engineering and Design*, vol. 238, pp. 3114–3120.

Dobson, R.T. and Ruppersberg, J.C. (2006). *A Novel Closed Loop Thermosyphon Heat Pipe Reactor Cavity Cooling System (RCCS) for a Pebble Bed Modular Reactor (PBMR).* Kumamato, Japan. 8th International Heat Pipe Symposium.

Eckert, E.R.G. and Carlson, W.O. (1961). Natural convection in an air layer enclosed between two vertical plates with different temperatures. *Int. J. Heat Mass Transfer*, vol. 2, pp. 106–120.

Eckert, E.R.G. and Drake, R.M. (1972). *Analysis of Heat and Mass Transfer.* McGraw-Hill.

Hoffmann, J. and van Rensburg, J. (2006 1-4 October). VERIFICATION AND VALIDATION OF THE CFD MODEL OF THE PBMR REACTOR. 3rd International Topical Meeting on High Temperature Reactor Technology, Johannesburg, South Africa.

Hossain, K., Buck, M., Ben Said, N., Bernnat, W. and Lohnert, G. (2008). Development of a fast 3D thermal–hydraulic tool for design and safety studies for HTRS. *Nuclear Engineering and Design*, vol. 238, pp. 2976–2984.

Incropera, F.P. and DeWitt, D.P. (2002). *Fundamentals of Heat and Mass Transfer.* 5th edn. John Wiley & Sons.

Khodabandeh, R. (2005). Pressure drop in riser and evaporator in an advanced two-phase thermosyphon loop. *International Journal of Refrigeration*, vol. 28, no. 5, pp. 725–734.

Koster, A., Matzner, H. and Nicholsi, D. (2003). PBMR design for the future. *Nuclear Engineering and Design*, vol. 222, pp. 231–245.

Mayson, R. (2005). The latest nuclear reactor technologies. In: *BEAwec Workshop.*

McKee, H. (1970). Thermosiphon Reboilers - A Review. *Industrial & Engineering Chemistry*, vol. 62, no. 12, pp. 76–82.

Mills, A.F. (1999). *Heat Transfer.* 2nd edn. Prentice Hall.

Modest, M. (2003). *Radiative heat transfer.* Academic Press.

Molz, M., Mantelli, M.B.H. and Milanez, F. (2004 September 21-25). Transient modeling of a closed two-phase thermosyphon for heat exchanger applications. 13th International Heat Pipe Conference, Shangai, China.

Narayana, K. (1998). View Factors for Parallel Rectangular Plates. *Heat Transfer Engineering*, vol. 19, no. 1, pp. 59–63.

Oh, C. and Davis, C. (2007 September 30-October 4). Rccs experiments and validation for high temperature gas-cooled reactor. The 12th International Topical Meeting on Nuclear Reactor Thermal Hydraulics (NURETH-12), Sheraton Station Square, Pittsburgh, Pennsylvania, U.S.A.

PowerBASIC Inc., Console Compiler 5. (2008).

Reimann, J., Piazza, G. and Harsch, H. (2006). Thermal conductivity of compressed beryllium pebble beds. *Fusion Engineering and Design*, vol. 81, pp. 449–454.

Reitsma, F., Strydom, G., de Haas, J., Ivanov, K., Tyobeka, B., Mphahlele, R., Downar, T., Seker, V., Gougar, H., Da Cruz, D. *et al.* (2006). The PBMR steady-state and coupled kinetics core thermal-hydraulics benchmark test problems. *Nuclear Engineering and Design*, vol. 236, no. 5-6, pp. 657–668.

Reyes, J.N. (2005). GOVERNING EQUATIONS IN TWO-PHASE FLUID NATURAL CIRCULATION FLOWS. *Natural circulation in water cooled nuclear power plants: phenomena models and methodology for system reliability assessments*, p. 155.

Robold, K. (1982). Wärmetransport im inneren und in der randzone von kugelschüttungen. *Kernforschungsanlage Jülich GmbH*, vol. JÜL, p. 1796.

Slabber, J. (2006). Technical description of the PBMR demonstration power plant. Tech. Rep. 016956, PBMR (Pty) Ltd. Revision 4.

Slabber, J.F.M. (2007). *Private Communication.* PBMR (Pty) Ltd., Centurion, South Africa.

Van Staden, M.P. (2004). Analysis of Effectiveness of the PBMR Cavity Cooling System. Beijing, China. Conf. High Temperature Reactor Technology.

Viljoen, C., Building, L., van Rooyen, W. and Mtyobile, V. (2006 1-4 October). THE USE OF CFD IN THE DESIGN OF PBMR TEST FACILITIES. 3rd International Topical Meeting on High Temperature Reactor Technology, Johannesburg, South Africa.

Welander, P. (1967). On the oscillatory instability of a differentially heated loop. *Fluid Mechanics*, vol. 29, pp. 17–30.

White, F.M. (2003). *Fluid Mechanics.* 5th edn. McGraw-Hill, New York.

Zehner, P. and Schlünder, E. (1972). Einfluß der wärmestrahlung und des druckes auf den wärmetransport in nicht durchströmten schüttungen. *Chem. Eng. Technol.*, vol. 44.